Title	X-ray Study of Luminous Supermassive Black Holes in the Brightest Cluster Galaxies
Author(s)	上田，周太朗
Citation	大阪大学，2014，博士論文
Version Type	VoR
URL	https://doi.org/10.18910/34047
rights	
Note	

X-ray Study of Luminous Supermassive Black Holes in the Brightest Cluster Galaxies

Shutaro Ueda
shutaro@ess.sci.osaka-u.ac.jp

Department of Earth and Space Science, Graduate School of Science,
Osaka University,
1-1, Machikaneyama, Toyonaka, Osaka, 560-0043,
Japan

February 4, 2014

Abstract

We present the X-ray study of luminous supermassive black holes (SMBHs) in the brightest cluster galaxies (BCGs). Our aim is to investigate whether or not there are significant differences in the properties of the luminous SMBHs in the BCGs from those in field galaxies. By referring both the *Planck* SZ cluster catalogue and the *Swift*/BAT 70-Month catalogue, we search for luminous SMBHs hosted by BCGs with X-ray luminosity of $L_{\rm X} > 1 \times 10^{45}\,{\rm erg\,s^{-1}}$ in the $14 - 195\,{\rm keV}$ band. We find two clusters out of 861 clusters sample. One is the Phoenix cluster ($z = 0.596$), and the other is H 1821+643 ($z = 0.297$).

Using the X-ray spectra obtained with the *Suzaku*/XIS & HXD, we detect a neutral iron K-line (Fe I) from both AGNs. The equivalent width (EW) of Fe I is $150^{+140}_{-60}\,{\rm eV}$ and $82 \pm 7\,{\rm eV}$, respectively. The Fe I line indicates that a large amount of cold gas, i.e., the torus, surrounds the luminous SMBHs. In particular, we measure that the column density ($N_{\rm H}$) of the torus is $3.2^{+0.9}_{-0.8} \times 10^{23}\,{\rm cm^{-2}}$ for the SMBH in the BCG of the Phoenix cluster. This values of $N_{\rm H}$ indicates that it is heavily obscured, i.e., it is classified as the type 2 quasi-stellar object (QSO). In the case of H 1821+643, we obtain the upper limit of the $N_{\rm H}$, i.e., luminous SMBH in its BCG is classified as the type 1 QSO.

We also analyze other three samples. One is in the BCG of IRAS 09104+4109, which is not included in both catalogues but the mass of the cluster and the X-ray luminosity of the type 2 QSO are below with the sensitivity limit of the surveys of *Planck* and *Swift*. The others are located in the field galaxies of ESP 39607 ($z = 0.201$) and 3C 433 ($z = 0.102$). By analyzing the X-ray spectra obtained with the *Suzaku*/XIS & HXD, we identify that they are heavily obscured and luminous AGNs. i.e., type 2 QSO. The EW of Fe I of each type 2 QSO is $539 \pm 150\,{\rm eV}$, $124^{+52}_{-31}\,{\rm eV}$, and $57^{+30}_{-27}\,{\rm eV}$, respectively.

We first focus on the environment of four type 2 QSOs with the $N_{\rm H}$ and the EW of Fe I. The relation of the $N_{\rm H}$ and the EW for four type 2 QSOs shows a similar trend to that expected from local AGNs in field. This result indicates that four type 2 QSOs have similar torus geometry of field AGNs even if the type 2 QSOs exist in the BCGs.

On the other hand, we also focus on the EW $-L_{\rm X}$ relation, i.e., the X-ray Baldwin effect. Our data of the QSOs in the BCGs are a little far away from the trend obtained from local type 2 AGNs. Since there are some causes to deviate the data points from the trend, we evaluate the standard deviation of the fluctuation by using a total of 59 type 2 AGNs in field. Thus, we obtain the standard deviation of $1\sigma_{\rm dex.} = 0.47\,{\rm dex}$. Although the type 2 QSO in the Phoenix cluster and that in IRAS 09104+4109 have the difference that are larger than $1\sigma_{\rm dex.}$ significance ($1.9\sigma_{\rm dex.}$ and $2.9\sigma_{\rm dex.}$ significance, respectively), the others are below $1\sigma_{\rm dex.}$ significance. The probability to obtain two sources out of three those that have deviations larger than $+1.9\sigma_{\rm dex.}$ and $+2.9\sigma_{\rm dex.}$ is 2×10^{-4}; we can reject

the hypothesis that the the three QSOs in BCGs follow the same with a significance level of $\sim 0.02\,\%$. If we focus on the two QSOs in the Phoenix cluster and H 1821+643, we should refer the probability to obtain one source out of two those that has deviations larger than $+1.9\sigma_{\rm dex.}$, which is 6%.

We also investigate the difference between the type 2 fraction for the QSOs in the BCGs and for those in field galaxies. By referring both catalogues, we find two samples, i.e., one is the type 1 QSO and the other is the type 2 QSO, meaning that the type 2 fraction is $50\,\%$. On the contrary, we measure the reflection fraction ($R; R = \Omega/2\pi$) of the torus of both QSOs. The mean values of the reflection fraction is $0.79^{+0.48}_{-0.39}$, which indicates that the type 2 fraction for QSOs in BCGs is $80\,\%$ (at least over $40\,\%$).

Overall, the EW$-L_{\rm X}$ relation, type 2 fraction, and reflection fraction of our sample of luminous AGNs in the BCGs suggest that covering factor is larger for those objects than than expected. If we assume a tours, its opening angle can be smaller than that expected in luminous AGNs in field galaxies.

We estimate the time scale of the AGN feedback of radiative mode. Since we find two clusters including luminous SMBHs ($L_{\rm X} > 1 \times 10^{45}\,{\rm erg\,s^{-1}}$ in the $14 - 195\,{\rm keV}$ band) in their BCGs, we estimate the time scale to be 23 Myr assuming that the age of cluster is 10 Gyr. We quantitatively obtain the time scale, for the first time.

To evaluate the effect of radiation heating, we evaluate the heating and cooling energy of three clusters. The total radiative energies in the Phoenix cluster, H 1821+643, and IRAS 09104+4109 are many orders of magnitude smaller than the total cooling energy of each cluster estimated by the bolometric luminosity of the ICM. The total mechanical energy in IRAS 09104+4109 overcomes the total cooling energy of the ICM, while the total mechanical energy in H 1821+643 is about a factor of 2 smaller than the total cooling energy of the its ICM. Since we have no data of the total mechanical energy in the Phoenix cluster, we can not discuss the case of the Phoenix cluster.

We estimate the mass of the torus in the Phoenix cluster and IRAS 09104+4109 to be $1.1 \times 10^{8}\,M_{\odot}$ and $9.8 \times 10^{7}\,M_{\odot}$ for the outer radius of 100 pc, respectively. If both SMBHs keep constant accretion rate during 23 Myr, the total accretion masses are estimated to be $2.5 \times 10^{9}\,M_{\odot}$ and $1.2 \times 10^{8}\,M_{\odot}$, respectively, which are larger than those of the tori. To maintain the mass of the torus, some mechanisms need to supply the cold gas. The cooling flow may supply the cooled gas and then the torus may play a role in a reservoir of cooled gas.

Contents

List of Tables

List of Figures

Chapter 1

Introduction

Clusters of galaxies are structures that consist of tens or hundreds of galaxies distributed in a few Mpc region. They are known to be the largest gravitationally bound objects in the Universe. The mass is evaluated from the velocity dispersion of the member galaxies in a cluster. It is typically $10^{14}-10^{15}\,M_{\odot}$, which is larger than the sum of those of member galaxies by one order of magnitude. This fact is recognized as the missing mass problem, in which the concept of a dark matter is introduced.

One of the greatest works in the history of X-ray astronomy is the discovery of the diffuse thermal X-ray emission from an intracluster medium (ICM); inter-galactic space is filled with a hot plasma of which temperature is $10^7 - 10^8\,\mathrm{K}$ and the gas number density is $10^{-2} - 10^{-5}\,\mathrm{cm}^{-3}$. The X-ray spectra of clusters show fluorescent lines of various elements, indicating that the ICM partly consists of the gas originated from member galaxies, though there may be some contributions of the primordial gas left over directly from the Big Bang. Although the ICM is basically in hydrostatic equilibrium with the gravitational potential primarily formed with dark matters, the cooling time of the ICM at the core of a cluster is much shorter than the age of the Universe. This result leads to the idea of the cooling flow, that is, the cooled gas should flow toward the center of the cluster. However, detailed X-ray spectroscopy and multi-wavelength study of the cores of clusters indicate that the cooling flow is significantly suppressed in most of the clusters.

One of the most promising models accounting for the suppression of the cooling flow is the heating of the ICM by radiations and jets from active galactic nuclei (AGNs), so-called the AGN feedback. The most luminous galaxy in a cluster is called a brightest cluster galaxy (BCG). The BCG is normally located at the center of the cluster. The BCG is usually a giant elliptical galaxy, often classified as a cD galaxy, where the suffix c indicates the fact that the galaxy is very large and the D denotes that the galaxy is diffuse. The BCGs often host AGNs with various levels of activity, and must play an important role of the AGN feedback.

Some of the supermassive black holes (SMBHs) in the BCGs have the mass of the order of $10^{10}\,M_\odot$, which is at the highest end of that of SMBHs in galaxies. This is a natural consequence of the well-known relation between the velocity dispersion of stars or gas in the bulge of a galaxy and the mass of SMBH at its center, so-called the $M_{\rm BH}-\sigma$ relation. The co-evolution of galaxies and SMBHs in them is one of the most extensively studied topics in the astronomy at present. The evolution of the BCGs and SMBHs in them may be just an extreme case of those for galaxies in general or significantly different from those for field galaxies. If there is a difference between the BCGs and the field galaxies, the evolution must be heavily affected by their environment. Therefore, the studies of the BCGs and the SMBHs in them are important to understand the co-evolution among three classes of objects, i.e., clusters, BCGs, and SMBHs. Note that the mechanism of the co-evolution is not only one-direction from a large scale to a small scale but also the inverse direction that must be important for the AGN feedback.

The origin of the SMBHs in the central galaxies has been a long standing issue before the recognition of the $M_{\rm BH}-\sigma$ relation. However, it is clear that the SMBHs are growing when gas accretions occur, although galaxy mergers might be another mechanism to increase the mass. We can see the scene of the growth of the SMBHs in AGNs. We thus study the luminous AGNs in the BCGs. We focus on the X-ray spectra of those sources, as they provide us the most accurate estimate of the intrinsic radiation power from the SMBHs, and their surrounding structure, such as an accretion torus, from the spectral shape including iron lines. With X-ray observations, we also measure various properties of the ICM (temperature, density, and abundance) surrounding the BCGs. While the extensive studies have been made for AGNs and for clusters of galaxies, they have been done rather separately by the experts of each field. We try to explore new fields combined AGNs with clusters in X-ray astronomy.

Our aim is to investigate whether there are significant differences in the properties of the luminous SMBHs in the BCGs from those in field galaxies. For this purpose, we have to be careful about the sample selection. We hence employ the *Planck* Sunyaev-Zel'dovich (SZ) cluster catalogue for a complete sample of clusters of galaxies. This catalogue is published in 2013. For a complete sample of the AGNs, we employ the *Swift*/BAT 70-Month catalogue. The cross correlation of these two catalogues, as the first attempt, provides us the fraction of luminous AGNs in the BCGs. Detailed X-ray properties of those AGNs are studied with the X-ray astronomy satellites, *Chandra*, *XMM-Newton*, and *Suzaku*.

Outline of this work is as follows. We first introduce brief reviews of clusters of galaxies, AGNs, and its feedback in Chapter 2. As our theme includes a wide range of objects, we have to focus on the topic directly relevant to our study. In Chapter 3, we introduce the X-ray observatories using in this work. We then pick up the sample of the luminous AGNs in BCGs by referring both the *Planck* Sunyaev-Zel'dovich cluster catalogue and the *Swift*/BAT 70-Month catalogue in Chapter 4. As a result, we find only two cases that the BCG is a luminous AGN. One is the Phoenix cluster having a very luminous type 2 quasar in its central galaxy and the other is H 1821+643 including a very luminous type 1 quasar. In Chapter 5, we analyze the X-ray spectra of both quasars obtained with the X-ray observations. Note that our results on the Phoenix cluster with *Suzaku* and *Chandra* have already been published (Ueda et al. 2013a). We extend our analysis to three type 2 quasars observed with *Suzaku* in Chapter 6. One is in a BCG but has been omitted in Chapter 4 because its X-ray luminosity and the SZ effect are just below the thresholds of both catalogues. The other two are in the field galaxies. We propose a hypothesis that the AGNs in the BCG tend to have larger equivalent widths of neutral iron lines than those expected from their X-ray luminosity. Discussions are described in Chapter 7, and summary is in Chapter 8.

Chapter 2

Review

2.1 Overview of Clusters of Galaxies

Clusters of galaxies, in which dark matters were first noticed by Zwicky (1933), are the largest gravitational bound objects in the Universe. Clusters are thus important targets for cosmology as for the cosmic microwave background (CMB; Penzias & Wilson 1965). For example, cosmological models employing cold dark matter and dark energy, such as the ΛCDM model (e.g., Riess et al. 1998; Perlmutter et al. 1999; Komatsu et al. 2011), can be examined with statistical studies of clusters of galaxies (e.g., Vikhlinin et al. 2009; Rozo et al. 2010; Vanderlinde et al. 2010). In this review, we briefly overview the history and current status of cluster studies.

Systematic observational studies of clusters were initiated by Abell, who picked up rich clusters of galaxies by examining the photographic plates obtained in the Palomar Observatory Sky Survey (POSS). This work was later extended to the southern sky and was summarized in the Abell catalogue of rich clusters of galaxies (Abell 1958; Abell et al. 1989), in which a total of 4073 clusters in the sky are listed.

Extensive studies of clusters were triggered by a discovery of X-ray emission from these objects. The first indication of the X-ray emission from clusters of galaxies was reported by Boldt et al. (1966) and Felten et al. (1966), who detected X-rays from the direction of the Coma cluster. *Uhuru* (Giacconi et al. 1971), the first X-ray astronomy satellite launched in 1970, revealed that the X-rays from clusters are diffuse emission (Forman et al. 1972). Mitchell et al. (1976) discovered a strongly ionized iron K-line (i.e., Fe XXV) in the X-ray spectrum of the Perseus cluster with *Ariel 5*. They revealed that the emission comes from optically thin thermal plasmas. These results indicate that the inter-galactic space is, surprisingly, filled with the intracluster medium (ICM) consisting of hot plasma with $T \sim 10^7 - 10^8$ K in which heavy elements are included. X-ray luminosities of clusters range typically in $10^{44} - 10^{45}\,\mathrm{ergs\,s^{-1}}$ with $H_0 = 50\,\mathrm{km\,s^{-1}\,Mpc^{-1}}$ (e.g., Jones & Forman 1984), and thus clusters are significant populations of extragalactic X-ray sources as for active galactic nuclei (AGNs).

X-ray surface brightness profiles of clusters were systematically studied with imaging instruments in sounding rockets, the *Einstein* X-ray Observatory (Giacconi et al. 1979), and *ROSAT*. These X-ray surface brightness profiles are usually fitted with so-called β model (e.g., King 1962; Ettori 2000). It is one of the methods to estimate the total gravitational mass within each radius under the assumption that the X-ray emitting thermal plasma is in hydrostatic equilibrium. A total mass of a cluster derived in this way is typically $10^{14} - 10^{15}\,M_\odot$ (e.g., Jones & Forman 1984), indicating there needs dark matters in a cluster. It is also found that the X-ray surface brightness profiles are different for clusters with or without cD galaxies at their centers; the clusters with cD galaxies show strong, sharp, and centered peaks (e.g., Gorenstein et al. 1977, 1978, 1979; Jones & Forman 1984; White et al. 1994), while those without do not. These peaks were interpreted as evidence of the cooling flow, which is described separately in Section 2.1.2.

Clusters of galaxies are important targets for currently working X-ray astronomy satellites, and a huge amount of studies has been accumulated. Common properties of clusters established in these X-ray studies can be summarized as follows.

- Clusters consist of galaxies, ICM (i.e., X-ray emitting plasma), and dark matters. The mass fraction of dark matter in a cluster is $\sim 80\,\%$ (e.g., David et al. 1995; Sato et al. 2012; Ichikawa et al. 2013). Stars and interstellar medium (ISM) in member galaxies account for only a few percent of the total mass, while the ICM contributes more than ($\sim 20\,\%$ of total mass; Sato et al. 2012).

- The ICM contains heavy elements such as oxygen, silicon, and iron (e.g. Fujita et al. 2008; Hoshino et al. 2010; Matsushita 2011; Simionescu et al. 2012; Sakuma et al. 2011; Ueda et al. 2013b). The heavy elements are distributed not only in the central regions but also in the outskirts of clusters. The iron abundance is uniform distribution with ~ 0.3 solar in the outskirts of clusters (e.g., Fujita et al. 2008; Simionescu et al. 2012; Ueda et al. 2013b; Matsushita et al. 2013).

New observational techniques using other wavelength bands other than X-rays have been established these days. One is the gravitational lensing (e.g., Einstein 1936; Zwicky 1937), in which target clusters function as gravitational lenses of background galaxies, and those lensed images usually in optical band can be used to estimates the mass distribution in the clusters (e.g., Turner et al. 1984; Narayan et al. 1984; Grossman & Narayan 1988, 1989; Miralda-Escude & Babul 1995; Mahdavi et al. 2008). The gravitational lens not only provides measurements of cluster mass independent to those with X-ray observations but also enable us to map the three-dimensional distribution of dark matter with some assumptions. The other one is the cluster searches through the Sunyaev-Zel'dovich effect observed in the CMB (Sunyaev & Zeldovich 1972, 1980). The Sunyaev-Zel'dovich effect is modification of the the CMB spectrum due to inverse-Compton scattering by electrons in the ICM. The effect is proportional simply to the optical depth and ICM temperature (e.g., Barbosa et al. 1996; Nagai et al. 2007), and thus more efficient to search for distant clusters than usual survey in optical or in X-rays band (e.g., Williamson et al. 2011; Planck Collaboration et al. 2014). In fact, we will employ some of the products of those surveys in Chapter 5.

2.1.1 Radiative Processes in X-ray Band

In this section, we briefly summarize radiative processes involved in X-ray emission from clusters of galaxies. More comprehensive descriptions are presented in e.g., Rybicki & Lightman (1985); Sarazin (1988), and also in the Atomic data for astrophysicists (ATOMDB[1]; Smith et al. 2001; Foster et al. 2012).

As mentioned above, the density and temperature of the ICM are typically $\sim 10^{-3} - 10^{-5}\,\mathrm{cm}^{-3}$ and $10^7 - 10^8\,\mathrm{K}$, respectively. Therefore, the ICM is a hot, collisionally-dominated optically-thin plasma. Involved radiative processes include thermal bremsstrahlung (i.e., free-free transitions), radiative recombination, dielectric recombination, one-electron radiative transitions, and so on. The emissivity (ϵ_ν^{ff}) of thermal bremsstrahlung in the CGS unit ($\mathrm{erg\,s^{-1}\,cm^{-3}\,Hz^{-1}}$) is

$$\epsilon_\nu^{ff} = 6.8 \times 10^{-38} Z^2 n_e n_i T_g^{-\frac{1}{2}} e^{-\frac{h\nu}{kT_g}} \bar{g}_{ff}, \tag{2.1}$$

where Z is the atomic number, n_e is electron number density, n_i is the number density of ions, T_g is temperature of the plasma, k is the Boltzmann constant ($k = 1.38 \times 10^{-16}\,\mathrm{erg\,K^{-1}}$), h is the Planck constant ($h = 6.63 \times 10^{-27}\,\mathrm{erg\,s}$), ν is frequency, and $\bar{g}_{ff}$ is a velocity averaged Gaunt factor, respectively. Assuming that n_e equals to n_i, the emissivity (ϵ_ν^{ff}) depends on square of the electron number density, i.e., $\epsilon_\nu^{ff} \propto n_e^2 T^{-\frac{1}{2}}$. The value of $\bar{g}_{ff}$ is of order unity for $h\nu/kT \sim 1$, and is 1 to 5 for $10^{-4} < h\nu/kT < 1$ (Figure 5.3 of Rybicki & Lightman 1985). Evaluating Equation 2.1 with $Z = 1$ yields,

$$\epsilon_\nu^{ff} = 6.3 \times 10^{-48} \Big(\frac{n_e}{10^{-3}\,\mathrm{cm}^{-3}}\Big)^2 \Big(\frac{kT_g}{10\,\mathrm{keV}}\Big)^{-\frac{1}{2}} e^{-\frac{h\nu}{kT_g}} \bar{g}_{ff} \quad \mathrm{erg\,s^{-1}\,cm^{-3}\,Hz^{-1}}. \tag{2.2}$$

The X-ray luminosity of thermal bremsstrahlung in the frequency range $\nu_1 < \nu < \nu_2$ is

---

[1] http://www.atomdb.org/

given by integrating Equation 2.1 in all volume, which is

$$L_{\mathrm{X}} = \int dV \int_{\nu_1}^{\nu_2} \epsilon_{\nu}^{ff} d\nu. \tag{2.3}$$

Assuming spherical symmetry, the bolometric luminosity of thermal bremsstrahlung is expressed as

$$L_{\mathrm{bol,bremss}} = 1.7 \times 10^{45} \Big(\frac{n_e}{10^{-3}\,\mathrm{cm}^{-3}}\Big)^2 \Big(\frac{kT_g}{10\,\mathrm{keV}}\Big)^{\frac{1}{2}} \Big(\frac{V}{\frac{4\pi}{3}(1\,\mathrm{Mpc})^3}\Big), \tag{2.4}$$

where pc is 3.09×10^{18} cm and V is a volume of emission region, respectively.

Processes other than thermal bremsstrahlung depend on the ionization states of atoms. A temperature T of 10^7 K or 10^8 K corresponds to energy $kT \sim 1$ keV or $kT \sim 10$ keV, respectively, which are comparable to the K-shell binding energies of heavy elements such as oxygen, neon, magnesium, silicon, sulfur, and iron. Therefore, most of the atoms are highly ionized, i.e., He-like, H-like and fully-ionized ions, in the ICM. Fractions of each ionization state for each element in the plasma with a given temperature can be calculated with the Saha equation (Rybicki & Lightman 1985). Transition probabilities of various processes in such a plasma can be calculated with some database for atomic level, and thus emission spectrum can be predicted. As an example, we show the equivalent width (EW) of an He-like iron K-shell line (Fe XXV, 6.7 keV) as a function of plasma temperature in Figure 2.1. The EW of Fe XXV is maximum at the temperature of $\gtrsim 2 \times 10^7$ K. We show the flux ratio of Fe XXV to Fe XXVI with temperatures in Figure 5.8. For optically-thin plasma in collisional ionization equilibrium (CIE), the Raymond-Smith model (Raymond & Smith 1977), the MEKAL model (Kaastra & Mewe 1993; Liedahl et al. 1995), and the APEC model (Smith et al. 2001) are available in the X-ray spectral analysis software, XSPEC (Arnaud 1996). We employ the APEC model, in which the ATOMDB (Smith et al. 2001; Foster et al. 2012) are used, in our X-ray spectral analysis.

2.1.2 Cooling Flow

In this subsection, we add some explanations on cooling flows in clusters of galaxies, which are mentioned above and may play important roles in co-evolution of BCGs and clusters. More detailed descriptions are given in Sarazin (1988); Fabian (1994); McNamara & Nulsen (2007); Fabian (2012).

The cooling efficiency of a plasma is dominated by thermal bremsstrahlung at high temperatures ($T_g > 2 \times 10^7$ K, left panel of Figure 2.2; Gehrels & Williams 1993) and by line emissions at low temperatures (right panel of Figure 2.2; Foster et al. 2012).

When thermal bremsstrahlung is the dominant process, the X-ray luminosity of ICM is proportional to square of the number density of electrons ($L_{\mathrm{X}} \propto n_e^2 T_g^{\frac{1}{2}}$) as mentioned

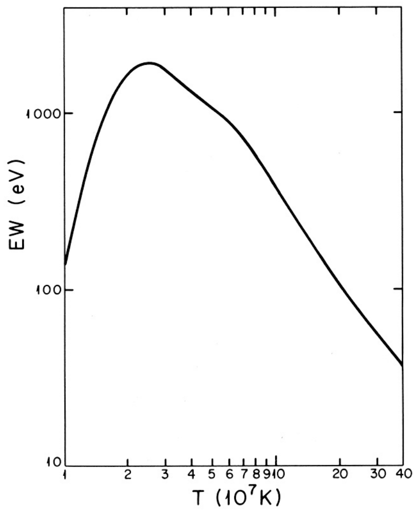

Figure 2.1: Equivalent width (EW) of He-like iron K-shell line (Fe XXV) as a function of plasma temperature (Figure 1 of Bahcall & Sarazin 1978). The EW is maximum at the plasma temperature $\gtrsim 2 \times 10^7$ K. ©AAS. Reproduced with permission.

in Section 2.1.1. We define the radiative cooling time ($t_{\rm cool}$) as $t_{\rm cool} = (d \ln T_g/dt)^{-1}$. If the ICM cools isobarically, this cooling time is expressed in

$$t_{\rm cool} \approx 8.5 \times 10^{10} \Big(\frac{n_e}{10^{-3}\,{\rm cm}^{-3}}\Big)^{-1} \Big(\frac{T_g}{10^8\,{\rm K}}\Big)^{\frac{1}{2}} \ \ {\rm yr}. \tag{2.5}$$

For the ICM with $n_e \sim 10^{-4}\,{\rm cm}^{-3}$ and $T_g \sim 10^8$ K, the cooling time is longer than the age of Universe. However, at the central regions of clusters of galaxies (typically $r < 100$ kpc), the electron number density is sometimes larger than $10^{-2}\,{\rm cm}^{-3}$. Then, the cooling time gets shorter than the age of Universe or the age of clusters of galaxies, for which we assume 10^{10} yr.

Adiabatic sound speed (c_s) in a gas is defined as

$$c_s^2 \equiv \frac{\partial P}{\partial \rho} = \gamma \frac{P}{\rho_g}, \tag{2.6}$$

where P is a pressure, ρ_g is a gas density, and γ is an adiabatic index (γ for the monoatomic gas is 5/3), respectively. For an ideal gas, P is given by $P = \rho_g k T_g/\mu m_{\rm p}$, where μ is a mean molecular mass ($\mu = 0.60$ in this work; Rosati et al. 2002) and $m_{\rm p}$ is a mass of proton, respectively. In this case, c_s is given by

$$c_s = \Big(\frac{5}{3}\frac{kT_g}{\mu m_{\rm p}}\Big)^{\frac{1}{2}} \approx 1500 \Big(\frac{T_g}{10^8\,{\rm K}}\Big)^{\frac{1}{2}} \ \ {\rm km\,s^{-1}}. \tag{2.7}$$

Using the virial radius ($r_{\rm vir}$) of clusters, the sound crossing time t_s is estimated to be

$$t_s = 2\frac{r_{\rm vir}}{c_s} \approx 1.3 \times 10^9 \Big(\frac{r_{\rm vir}}{1\,{\rm Mpc}}\Big) \Big(\frac{c_s}{1500\,{\rm km\,s^{-1}}}\Big)^{-1} \ \ {\rm yr}. \tag{2.8}$$

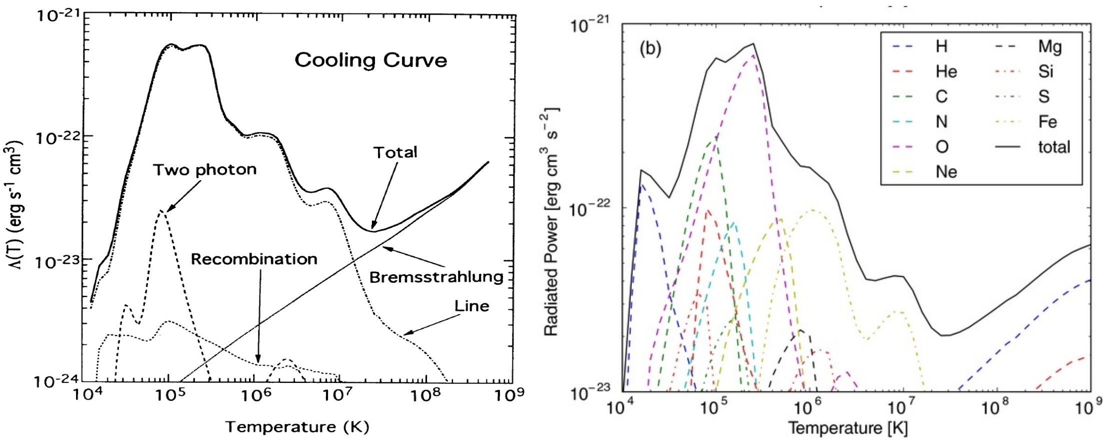

Figure 2.2: Cooling Curve as a function of the ICM temperature. Left: Temperature dependence of the cooling efficiency for each process in an optically-thin plasma of the cosmic abundance of Allen (1973) reported by Gehrels & Williams (1993). Right: Cooling function as a function of temperature for each element with the solar abundance of Anders & Grevesse (1989) reported by Foster et al. (2012). ©AAS. Reproduced with permission.

This is shorter than the age of clusters, and thus we can assume that the ICM is in hydrostatic equilibrium. The pressure is therefore balanced with the gravitational force. Thus, with a spherical symmetry,

$$\frac{dP}{dr} + \rho_g \frac{GM(r)}{r^2} = 0, \tag{2.9}$$

where G is the Gravitational constant and $M(r)$ is a total mass within r.

At the central regions of clusters, ICM is cooled by X-ray radiation with a shorter time scale than the age of clusters. The decrease in the temperature of the ICM causes the depletion in the pressure, which leads to a mass flow from the outer region to the central region so that the hydrostatic equilibrium (2.9) is satisfied. This flow is called "cooling flow" (Cowie & Binney 1977; Fabian & Nulsen 1977; Mathews & Bregman 1978; Fabian 1994). We define the radius $r_{\rm cool}$ as the size of a cool core. The mass deposition rate (or sometimes called cooling flow rate, $\dot{M}$) across $r_{\rm cool}$ is determined with the bolometric luminosity ($L_{\rm bol}$) within $r_{\rm cool}$ and the temperature of the ICM (dT_g) at $r_{\rm cool}$. If we assume the system is spherically symmetric and the cooling is only due to radiation from the ICM plus the PdV work done on the ICM, the following equation is obtained.

$$L(T_g) = \frac{5}{2}\frac{\dot{M}}{\mu m_{\rm p}} kT_g. \tag{2.10}$$

This leads

$$\dot{M} = \frac{2}{5}\frac{\mu m_{\rm p} L_{\rm bol}}{kT_g} \approx 460 \Big(\frac{T_g}{10^8\,{\rm K}}\Big)^{-1} \Big(\frac{L_{\rm bol}}{10^{45}\,{\rm erg\,s^{-1}}}\Big) \;\; M_\odot\,{\rm yr}^{-1}. \tag{2.11}$$

In a typical cluster, this mass deposition rate can be $\sim 100\,M_{\odot}\,\mathrm{yr}^{-1}$. If such a cooling flow is maintained for 10 Gyr, the total accreted mass amount to $\sim 10^{12}\,M_{\odot}$, which is comparable to that of a galaxy. The temperature of the accreted gas must be much lower than T_g in the core of a cluster. Therefore, it is expected that the cooling flow induces a massive starburst in the center of a cluster (i.e., in its central galaxy).

Nevertheless, we have little observational evidence of the expected levels of cooling flows in clusters. The total mass of cooled dust in and around the central galaxy is many orders of magnitude smaller than expected value from the cooling flow (Edge 2001). The star formation rate in central galaxies in clusters is 10 % or smaller of the cooling flow rate (e.g., O'Dea et al. 2008). Signatures of cooling flows can also be examined by observing X-ray emission lines below 1 keV including various Fe L-shell lines from which the amount of low-temperature plasma is measured (Böhringer et al. 2002). However, observations with the *XMM-Newton*/Reflection Grating Spectrometer (RGS) revealed that no significant Fe XVII line at $\sim$ 1 keV is found in X-ray spectra of A 1835 (Peterson et al. 2001) and A 1795 (Tamura et al. 2001). The prominent Fe XVII line at 12 Å in low-temperature plasma is either weak or absent in cooling flow clusters (Peterson et al. 2003), although there is a hint of the Fe XVII line emission in the A 2597, whose flux is consistent with a cooling rate of $\sim 100\,M_{\odot}\,\mathrm{yr}^{-1}$ (Morris & Fabian 2005). Extensive discussions have been made to account for this contradiction on cooling flows, so called the "cooling flow problem" (Fabian 1994). At present, it is believed that cooling flows are not as strong as that expected from the simplified estimate, as mentioned above. This indicates that some heating mechanism function at the center of the cluster to suppress the cooling flow. One of the most promising heating mechanisms is the AGN feedback (Peterson & Fabian 2006; McNamara & Nulsen 2007). Note that even if there is no cooling *flow*, energy loss by radiation must take place. We thus use the mass deposition rate ($\dot{M}$) defined above but with a different name, i.e., cooling rate.

2.2 Overview of Active Galactic Nuclei (AGNs)

Active galactic nuclei (AGNs) are core regions of the galaxies that have significantly higher luminosities than those in normal galaxies. Their luminosities are in some cases comparable to those of the whole galaxies, and their spectra of the radiation range over various wavelength (e.g., Peterson 1997; Beckmann & Shrader 2012b). A pioneering work on this subject was performed by Seyfert (1943), who obtained optical spectra of six spiral galaxies of which cores are very bright and found emission lines from them. This emission component, however, remained a mystery. Later in 1960's, Schmidt (1963) identified the radio source 3C 273 with an optical counter part of which spectrum shows a huge redshift of $z = 0.158$. Since this source and its similar sources were not resolved at that time, they were called quasi-stellar objects (QSOs) or quasars (Burbidge & Burbidge 1966; Burbidge 1967). With extensive discussions on the nature of these objects, huge amount of radiation generated by accretion onto supermassive black holes (SMBHs) in distant galaxies was recognized s the most promising explanation for these objects (Hoyle & Fowler 1963; Salpeter 1964; Zel'dovich 1964; Lynden-Bell 1969; Lynden-Bell & Rees 1971). The cores of the galaxies observed by Seyfert are believed to have the same origin.

AGNs have been extensively observed in all wavelength bands, from radio to γ-ray, sometimes simultaneously. There are various schemes of classifications of AGNs, each focusing on their properties in some wavelength band. Although it is beyond the scope of this review to cover all those classifications, we know that many properties of AGNs are different in those with strong radio emission and those without; the former are called radio-loud AGNs and the latter radio-quiet AGNs (Peterson 1997; Beckmann & Shrader 2012b, and references therein). Radio-loud AGNs are characterized with prominent jets and the radiation associated with them, while those features are not significant in radio-quiet AGNs. Radio-quiet AGNs are major population in the AGNs. Those in the local Universe are called Seyfert galaxies (to be precise the nuclei of Seyfert galaxies), and those in the distant Universe are (radio-quiet) QSOs. Nomenclature of AGNs is not well-defined, but we call luminous AGNs QSOs in this work.

Among various wavelength bands, the X-ray band has of special importance for AGN studies. Elvis et al. (1978) discovered that Seyfert galaxies are as X-ray sources for the first time. For most of the (radio-quiet) AGNs, the X-ray band is the highest energy end of their spectrum detected so far (Peterson 1997; Beckmann & Shrader 2012b). It means that matters in the vicinity of the SMBHs can be extracted with X-ray observations for those AGNs. The strong penetration power of X-rays enforce this point. Spectra of emissions from AGNs are relatively flat; there are almost equal power for each wavelength band, very much different from stars, of which spectra peak at the optical band (Peterson 1997; Beckmann & Shrader 2012b). As a result, when we observe a galaxy hosting an AGN with X-rays, contamination from stars in the host galaxies are negligibly small. In fact, the AGNs are most abundant X-ray sources in the sky. A significant fraction of the cosmic X-ray background (CXB; e.g., Giacconi et al. 1962; Boldt 1987; Gruber et al. 1999) is also composed of unresolved distant AGNs (e.g., Mushotzky et al. 2000; Brandt & Hasinger 2005).

There are various aspects in AGN studies. Some researchers are interested in physics of accretion onto the SMBHs, of which mass ranges from $10^5\,M_\odot$ to $10^{10}\,M_\odot$. Although there found or assumed many structures around SMBHs, such as accretion disks, broad line regions, torus, narrow line regions, and relativistic jets (e.g., Urry & Padovani 1995; Beckmann & Shrader 2012b), whole picture has not yet been established. Another aspect of the AGN studies is to focus rather on the origin and evolution of the SMBHs, which is one of the biggest issues in astronomy today. It is widely believed that almost all the galaxies have an (or a few) SMBH at its center. Small fraction of them are active, i.e., AGNs, but others are dormant. In addition, the $M_{\rm BH}-\sigma$ relation discovered by Magorrian et al. (1998) and followed by extensive studies (e.g., Ferrarese & Merritt 2000; Gebhardt et al. 2000; Tremaine et al. 2002; Gültekin et al. 2009; Sadoun & Colin 2012; Salviander & Shields 2013; McConnell & Ma 2013) is important. This is a strong correlation between a mass of the SMBH at the center of a galaxy ($M_{\rm BH}$) and the velocity dispersion of gas or stars in the bulge of the galaxy (σ). Since the velocity dispersion, σ, is also positively correlated with the mass of the bulge of the galaxy or whole the galaxy, this relation can be expressed as the mass of an SMBH and that of the host galaxy is strongly correlated; the mass of an SMBH is $\sim 0.2\,\%$ of the bulge of host galaxy (e.g., Marconi & Hunt 2003; Häring & Rix 2004; Kormendy & Ho 2013). Although mechanism to make this correlation has not yet been fully understood, it is clear that those two kinds of structures, of which sizes are different by roughly ten orders of magnitude, have close interaction each other in their evolution, i.e., co-evolution (e.g. Kormendy & Ho 2013).

The $M_{\rm BH}-\sigma$ relation and related studies on the co-evolution of SMBHs and galaxies motivated us to examine the possible co-evolution with a large scale, i.e., clusters. We focus on luminous AGNs in BCGs. We would attempt a statistical study to evaluate how much fraction of the SMBHs is active in the BCGs at first. We then search for any unique properties of the luminous AGNs in BCGs that are different from AGNs in field galaxies. In the second step, we employ X-ray observations of those sources, with which intrinsic activity of the SMBHs are best evaluated and geometry of surrounding structures, in particular, accretion torus can be examined. The accretion torus is a key structure in the

AGN unification model. We introduce the model in the next subsection.

2.2.1 The AGN Unification Model

Seyfert (1943) showed that some galaxies indicate broad emission lines in the optical spectra, while other exhibited only narrow ones. The former are classified as type 1 and the latter as type 2. The optical spectra of type 2 AGNs show strong permitted and forbidden lines that line widths are $\lesssim 1000\,\mathrm{km\,s^{-1}}$ and the flux ratio of [O III]λ5007 to Hβ is ~ 10 (e.g., Antonucci 1993). The spectra of type 1 AGNs exhibit permitted lines with broad line widths of $1000 \sim 10,000\,\mathrm{km\,s^{-1}}$ in addition to the narrow lines that are seen in those of type 2 AGNs (e.g., Peterson 1997; Beckmann & Shrader 2012b). Extensive studies of these emission lines revealed that there are two kinds of line emitting clouds of which distances from the central SMBHs are different and thus their velocities are different (Peterson 1997; Beckmann & Shrader 2012b). The region from which narrow lines are emitted is called a narrow-line region (NLR), while broad lines are emitted from a broad-line region (BLR). Clouds in both regions are photoionized by strong ultraviolet (UV) and X-ray continuum radiation from the vicinity of the SMBH, though the BLR clouds have much higher density than those in the NLR regions (Netzer 1990, and references therein). Note that the locations of the BLR clouds in some AGNs are accurately measured with so-called reverberation mapping (e.g., Blandford & McKee 1982; Peterson 1993; Peterson et al. 2004) and those results yield one of the most reliable estimates on the masses of SMBHs (e.g., Hayashida et al. 1998; Czerny et al. 2001).

Antonucci & Miller (1985) discovered broad permitted lines, as seen in type 1 AGNs, in the optical spectrum of polarized photons from the nuclear region of a type 2 AGN, NGC 1068. The broad lines in the polarized light spectra are considered to be originated from a hidden BLR and scattered at the surface of an absorber that hides the BLR from our line of sight (Antonucci & Miller 1985; Miller & Goodrich 1990; Miller et al. 1991; Antonucci 1993). The absorber must have a hole for the scattered light to pass through. An obscuring dust structure with a toroidal geometry, i.e., torus, was introduced to account for the observational results of NGC 1068. Based on this model, the BLR could be observed, and thus the AGN could be classified as type 1, if our line of sight is along the direction of a hole in the absorber. In this case, there should be no essential difference between type 1 AGNs and type 2 AGNs. This is sometimes called the AGN unification model.

Strong support for this unification model came from X-ray observations; a heavily absorbed component (column density is higher than $10^{23}\,\mathrm{cm^{-2}}$) is found in the X-ray spectra of many type 2 AGNs (e.g., Awaki et al. 1990, 1991b; Koyama et al. 1992; Iwasawa et al.

1993). These results are not only the evidence of the absorbers assumed in the unification model but also can be the measure for physical parameters of absorbers. Furthermore, not only type 2 AGNs but also type 1 AGNs exhibit a reflection component in their X-ray spectra, which is characterized with a flat continuum with a hard X-ray bump and strong fluorescence K-shell lines of neutral atoms, in particular iron (e.g., Mushotzky et al. 1993; Miller 2007). The continuum is well reproduced with a model in which a power-law continuum injected to a matter with an infinite optical depth are Compton scatted and emerged from the surface (e.g., Beckmann & Shrader 2012b).

In the simplest case in which energy shift in the scattering is ignored and only single scattering is considered, the spectral shape of the reflection component can be described as

$$F_{\mathrm{ref}}(E_x) = \frac{\mu_{\mathrm{scat}}}{\mu_{\mathrm{abs}(Ex)} + \mu_{\mathrm{scat}(E_x)}} \times f \times N \times E_x^{-\Gamma}, \tag{2.12}$$

where $F_{\mathrm{ref}}(E_x)$ is the spectra emerging from the surface of the matter, E_x is an X-ray energy, μ_{scat} is the absorption coefficient for scattering, μ_{abs} is that for pure absorption, f is a factor determined from the geometry of the matter and the irradiation source, N is the normalization of the incident spectrum, and Γ is a power-law (photon) index of the incident spectrum, respectively. The spectrum of the reflection continuum should be different from that suffered by absorption. That is, if we neglect the contribution from scatted X-rays,

$$F_{\mathrm{abs}}(E_x) = \exp\Big(-(\mu_{\mathrm{abs}(Ex)} + \mu_{\mathrm{scat}(Ex)}) \times N_{\mathrm{H}}\Big) \times N \times E_x^{-\Gamma}, \tag{2.13}$$

where $F_{\mathrm{abs}}(E_x)$ is the spectra passing through an absorber of the hydrogen column density of N_{H}. Although both reflection continuum and absorption continuum have absorption edge features, especially that associated with the iron K edge at 7.1 keV, the shapes of the continuum are different. On the other hand, the intensities of the fluorescence K-shell lines are proportional to the abundance of elements and to integrated flux of the incident photons of which energies are above the absorption edge of the corresponding element.

$$F_{\mathrm{Fe-K}} \propto f_{\mathrm{fy}} \times f \times \int_{E_{\mathrm{K-edge}}}^{\infty} \Big(1 - \exp(Z_{\mathrm{Fe}} \times N_{\mathrm{H}} \times \mu_{\mathrm{abs}(E_x)})\Big)(N \times E_x^{-\Gamma})dE_x, \tag{2.14}$$

where $F_{\mathrm{Fe-K}}$ is the intensity of the iron K fluorescence line (Fe I), $E_{\mathrm{K-edge}}$ is the K-edge energy (7.1 keV; Henke et al. 1993), f_{fy} is the fluorescence yield of iron (0.3; Bambynek et al. 1972), and Z_{Fe} is the metallicity of iron of matters, respectively. The K-shell photo-ionization cross section per iron atom against an X-ray with energy above 7.1 keV is $6.0 \times 10^{-18}(E/1\,\mathrm{keV})^{-2.58}\,\mathrm{cm}^2$ (Henke et al. 1982).

Considering these processes and assuming geometry and abundance of a torus, location of the primary source with a power-law X-ray spectrum, and the direction of our

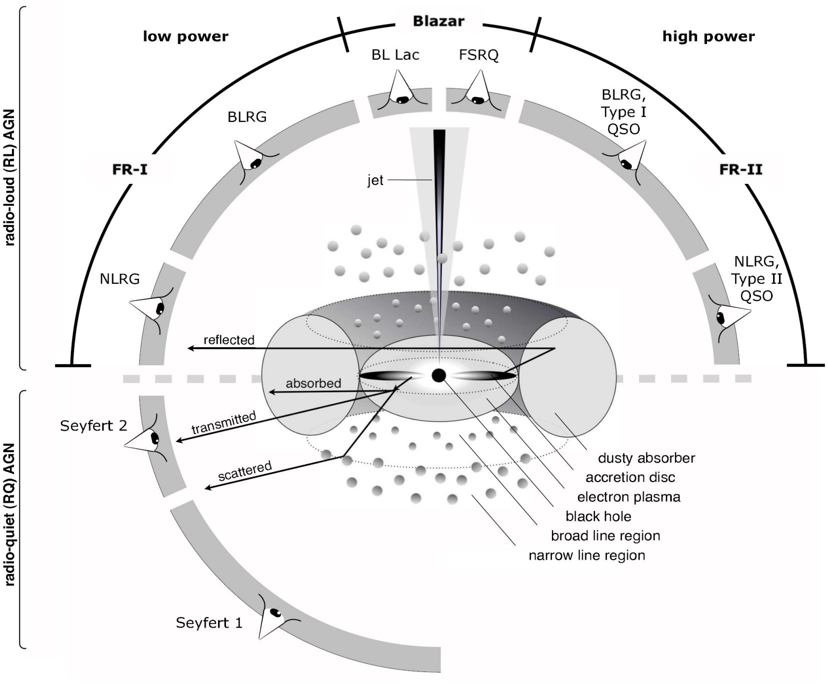

Figure 2.3: Sketch of the AGN unification model (Figure 1 of Beckmann & Shrader 2012a). "Graphic: Beckmann & Shrader (2012)" `http://adsabs.harvard.edu/abs/2012agn..book.....B`, reproduced with permission, © Dr. Volker Beckmann, private communication.

line of sight. One can calculate the X-ray spectra that are composed of several components (direct, reflected, absorbed, and fluorescent lines) and compare with observed ones. In most cases, the direct component is dominant in the X-ray spectra of type 1 AGNs, while it is seldom observed in those of type 2 AGNs This was a strong support for the AGN unification model (e.g., Awaki et al. 1991a; Antonucci 1993; Urry & Padovani 1995). As mentioned above, type 1 and type 2 classifications were originally introduced from optical spectroscopy. However, X-ray spectra have also been used for the type 1 and 2 classifications. The X-ray spectral models have sophisticated by employing Monte Carlo simulations. For example, Ikeda et al. (2009) examined X-ray spectra expected by alternating the opening angle of the torus and the inclination angle of the line of sight. In the case of Fe I, an equivalent width of Fe I with N_{H} of $10^{23}\,\mathrm{cm}^{-2}$ is decreases from $\sim 80\,\mathrm{eV}$ to $\sim 20\,\mathrm{eV}$ when the opening angle changes 20° to 80° even the same inclination angle (Ikeda et al. 2009).

The AGN unification model is illustrated in Figure 2.3 , with various structures other than the accretion torus (Beckmann & Shrader 2012a). The illustration is an interpretation based on various observations of AGNs, but not from the direct imaging.

X-ray Baldwin Effect

Baldwin (1977) reported that the luminosity of C IVλ1550 is inversely correlated with the luminosity of continuum of 1450 Å for 20 QSOs. Iwasawa & Taniguchi (1993) discovered similar anti-correlation between the equivalent widths of neutral iron K-line (Fe I) and the intrinsic (absorption corrected) X-ray luminosity of AGNs. This trend is called "the X-ray Baldwin effect" or "the Iwasawa-Taniguchi effect" (e.g., Bianchi et al. 2007). The X-ray Baldwin effect has been recently confirmed with not only type 1 AGNs but also with type 2 AGNs (Fukazawa et al. 2011). If we assume that a torus covers some fraction of the solid angle from the primary continuum source, the ratio of height to inner radius or the opening angle of the torus is the parameter to control the covering factor. When X-ray luminosity of the central engine gets high, the inner torus is photoionized by X-rays and evaporated, leading to a reduction in the covering factor (e.g., Page et al. 2004; Zhou & Wang 2005). Higher luminosity AGNs should have larger opening angle of tori. Observations and simulations supporting this idea have been presented (e.g., Page et al. 2004; Bianchi et al. 2007; Ricci et al. 2013). Figure 2.4 shows the relation between EW of Fe I and X-ray luminosity in $2-10\,\mathrm{keV}$ obtained from the *Chandra*/HETG observations (Shu et al. 2010) and simulations reported by Ricci et al. (2013). As will be mentioned in the next Subsubsection, type 2 fraction as a function of X-ray luminosity is also consistent with this point of view.

Using the ionization parameter (ξ; Tarter et al. 1969), we describe the relation of the AGN luminosity and the region that enable to emit the Fe I line.

$$n_{\mathrm{gas}} = \frac{L_{\mathrm{i}}}{\xi \times r_{\mathrm{in}}^{2}}, \tag{2.15}$$

where n_{gas} is a number density of the gas, L_{i} is an ionizing luminosity, and r_{in} is the inner radius to emit the Fe I. Thus, we estimate the inner radius to be

$$r_{\mathrm{in}} = 1 \times 10^{20} \Big(\frac{L_{\mathrm{i}}}{10^{45}\,\mathrm{erg\,s^{-1}}}\Big)^{\frac{1}{2}} \times \Big(\frac{\xi}{1}\Big)^{-2} \times \Big(\frac{n_{\mathrm{gas}}}{10^{5}\,\mathrm{cm^{-3}}}\Big)^{-2} \quad \mathrm{cm}. \tag{2.16}$$

Equation 2.16 shows $r_{\mathrm{in}} \propto L_{\mathrm{i}}^{1/2}$, which indicates that the EW of Fe I decreases when the AGN becomes bright with a similar torus geometry. Because the size of the region to emit the Fe I is reduced by the radiation from the SMBH.

Type 2 Fraction in the Universe

The AGN unification model introduced in Section 2.2.1 is basically approved by researchers. However, some results have been presented that type 1 and type 2 AGNs may have intrinsic difference in their statistical properties (e.g., Wu et al. 2009). In other words, not all the AGNs have the same geometry of the torus, as is suggested in the X-ray Baldwin effect. The type 2 AGN fraction is defined as $n_2/(n_1+n_2)$, where n_1 and n_2 are number densities of type 1 AGNs and type 2 AGNs. This fraction tells us the (averaged) opening angle (Ω) of tori of all the AGNs in the AGN unification model with the relation of $\Omega = 4\pi n_2/(n_1+n_2)\,\mathrm{str}$. Ueda et al. (2003) revealed that the type 2 fraction in the Universe depends on an intrinsic X-ray luminosity of AGN. The type 2 fraction is smaller for more luminous AGNs. This is consistent with a trend, in different notations, that lower luminosity AGNs have systematically have higher column density or higher fraction to be obscured AGNs (e.g., Lawrence & Elvis 1982; Lawrence 1991; Steffen et al. 2003; Simpson 2005; Hasinger 2008; Lusso et al. 2013).

Figure 2.5 shows the type 2 fraction obtained with X-ray and also infrared observations (Hasinger 2008). The type 2 fraction is smaller for higher luminosities as was presented by Ueda et al. (2003). The fraction is 20 % or less for AGNs with the $2-10\,\mathrm{keV}$ X-ray luminosity of $10^{45}\,\mathrm{ers\,s^{-1}}$. Extensive studies supporting similar trend have been obtained by other researchers employing various wavelength data with various data reduction methods (Steffen et al. 2003; Barger et al. 2005; Akylas et al. 2006; Treister & Urry 2006; Gilli et al. 2007; Treister & Urry 2012). However, as pointed out by Urry & Treister (2007) and Treister & Urry (2012), this trend is very sensitive to selection bias. In particular, highly obscured (sometimes called Compton thick $N_{\mathrm{H}} > 10^{24}\,\mathrm{cm^{-2}}$) type 2 AGN might have been missed in infrared, optical, UV, and soft X-ray surveys. Hard X-ray surveys with higher sensitivity may be required for this issue.

The redshift dependence of the type 2 fraction is less clear. Note that mean AGN luminosity is higher for larger redshift and the type 2 fraction can be smaller even if the type 2 fraction of a given luminosity is independent on the redshift.

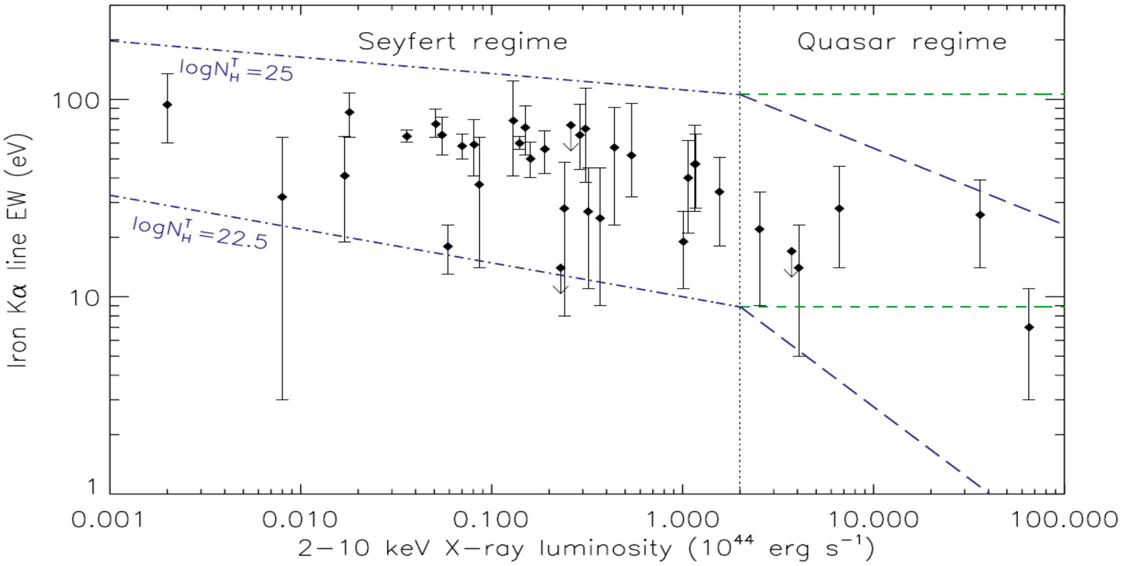

Figure 2.4: The dependence of EW of Fe I on X-ray luminosity in $2-10\,\mathrm{keV}$ with the data obtained from the observations and simulations (Figure 7 of Ricci et al. 2013). The EW of Fe I versus X-ray luminosities and predicted trends obtained for different values of the equatorial column density of the torus (Ricci et al. 2013). The data points are reported by Shu et al. (2010) and obtained by averaging multiple *Chandra*/HETG observations of AGNs. The two blue dash-dotted lines are the fits to the simulations of the X-ray Baldwin effect using the $\theta_{\mathrm{OA}} - L_{\mathrm{X}}$ relationship of Hasinger (2008) for the Seyfert regime ($\log \mathrm{EW} = 1.01 - 0.17 \log L_{\mathrm{X},44}$ for $\log N_{\mathrm{H}}^{\mathrm{T}} = 22.5$, and $\log \mathrm{EW} = 2.05 - 0.08 \log L_{\mathrm{X},44}$ for $\log N_{\mathrm{H}}^{\mathrm{T}} = 25$), where θ_{OA} is a half-opening angle and $N_{\mathrm{H}}^{\mathrm{T}}$ is an equational column density (Ricci et al. 2013). The blue long-dashed lines represent the $\mathrm{EW} - L_{rmX}$ relations obtained in the quasar regime ($\log \mathrm{EW} = 1.11 - 0.73 \log L_{\mathrm{X},44}$ for $\log N_{\mathrm{H}}^{\mathrm{T}} = 22.5$, and $\log \mathrm{EW} = 2.14 - 0.39 \log L_{\mathrm{X},44}$ for $\log N_{\mathrm{H}}^{\mathrm{T}} = 25$) using the relationship of Hasinger (2008), while the green dashed lines represent those attained using the relationship of Burlon et al. (2011). The intercepts obtained in the quasar regime have been modified to match those obtained at lower luminosities (Ricci et al. 2013). (Ricci et al., A&A, vol. 553, A29, 2013, reproduced with permission © ESO.)

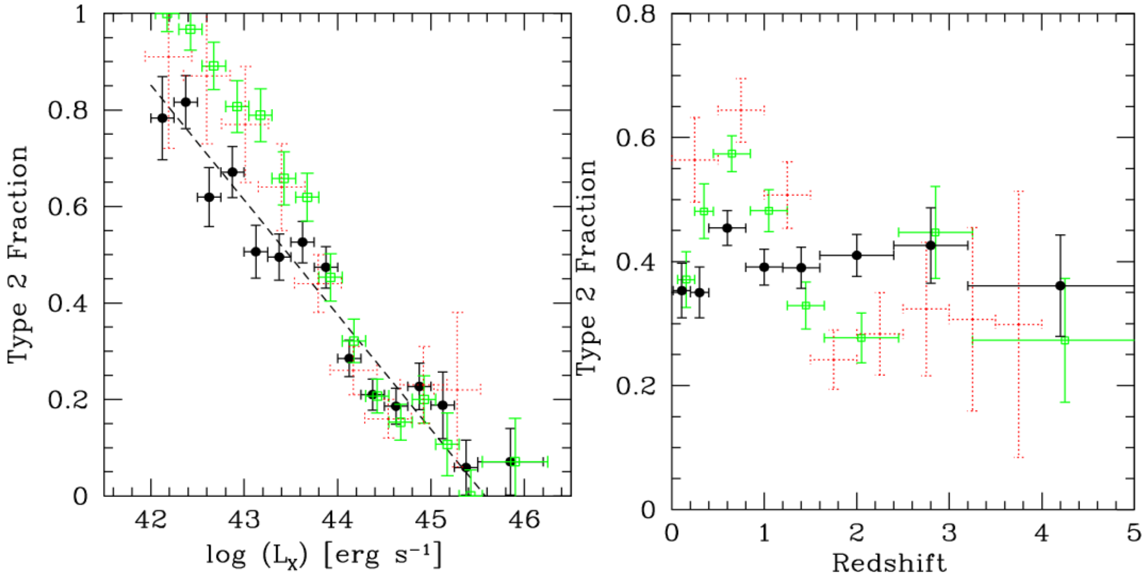

Figure 2.5: Type 2 fraction in the Universe (Figure 10 of Hasinger 2008). Left: Type 2 fraction as a function of X-ray luminosity. Right: Type 2 fraction as a function of the redshift. The filled black data points with thick error bars correspond to the combined optical/X-ray classification. The green data points with open squares and thin error bars have been derived using a purely optical spectroscopic classification, where only broad-line AGN are classified as type 1 objects. Red data points with dotted error bars are from Treister et al. (2008) for the left panel and from Treister & Urry (2006) for the right panel, respectively. (Hasinger, A&A, 490, 905, 2008, reproduces with permission © ESO.)

2.3 Brightest Cluster Galaxies and Quasars

Brightest cluster galaxies (BCGs) host SMBHs at their nuclei as for other galaxies. BCGs and their SMBHs are located at the highest end of the $M_{\rm BH} - \sigma$ mentioned in McConnell et al. (2011). However, a large scatter and/or deviation of the $M_{\rm BH} - \sigma$ relation extrapolated from the non-BCG sample were found for a few SMBHs in BCGs (e.g., Hopkins et al. 2007; Gültekin et al. 2009; McConnell et al. 2011, 2012; McConnell & Ma 2013; Graham & Scott 2013). This may indicate SMBHs of the highest mass ($\sim 10^{10}\,M_\odot$) and their host BCGs undergo some unique history of merging and/or accretion processes, as is also predicted by numerical simulations by e.g., Zubovas & King (2012) and Volonteri & Ciotti (2013).

McConnell et al. (2011) estimated the number density of SMBHs in the highest mass limit ($10^9 - 10^{10}\,M_\odot$) by employing the $M_{\rm BH} - L$ relation (e.g. Ferrarese & Merritt 2000; McLure & Dunlop 2002; Marconi & Hunt 2003) and the luminosity function of nearby galaxies. They found the number density is consistent with that of nearby BCGs. McConnell et al. (2011) suggest that local BCGs host the remnants of highly luminous QSOs. This idea is supported by some numerical simulations indicating that luminous high-redshift QSOs end up as SMBHs in the BCGs of rich clusters at the local Universe, as is shown in Figure 2.6 (e.g., Springel et al. 2005, 2006; Li et al. 2007; Angulo et al. 2012). Observationally, De Lucia & Blaizot (2007) shows that high-redshift BCGs belong to the same populations of local BCGs in their massive end, and Husband et al. (2013) indicate that the luminous QSOs at $z \sim 5$ likely represent an early stage in building up massive low-redshift clusters.

The number density of distant QSOs is larger than that of nearby QSOs (Richards et al. 2006). QSOs would be very active in the early Universe, possibly at $z = 2 - 4.5$, but are dormant at present (e.g., Richards et al. 2006; Vestergaard et al. 2008). For example, the prominent radio-jet galaxy M87 that is the BCG of the Virgo cluster hosts an SMBH with $6.3 \times 10^9\,M_\odot$ (McConnell et al. 2011), but the present luminosity is many orders of magnitude lower than the Eddington limit (Rafferty et al. 2006), which is much lower than those of typical AGNs.

Detailed study of the active phase of the SMBHs in BCGs is difficult for the sources at $z > 1$, but there are exceptional cases in which QSOs are found in the BCGs of clusters at lower redshift. In such sources, SMBHs are surely growing by gas accretion (e.g., Salpeter 1964; Hopkins et al. 2005), while strong radiation and/or jets from the SMBHs might affect the ICM in clusters (e.g., Fabian 2012). Therefore, those sources are of extreme importance for the study of the feeding and feedback processes in SMBHs, BCGs, and

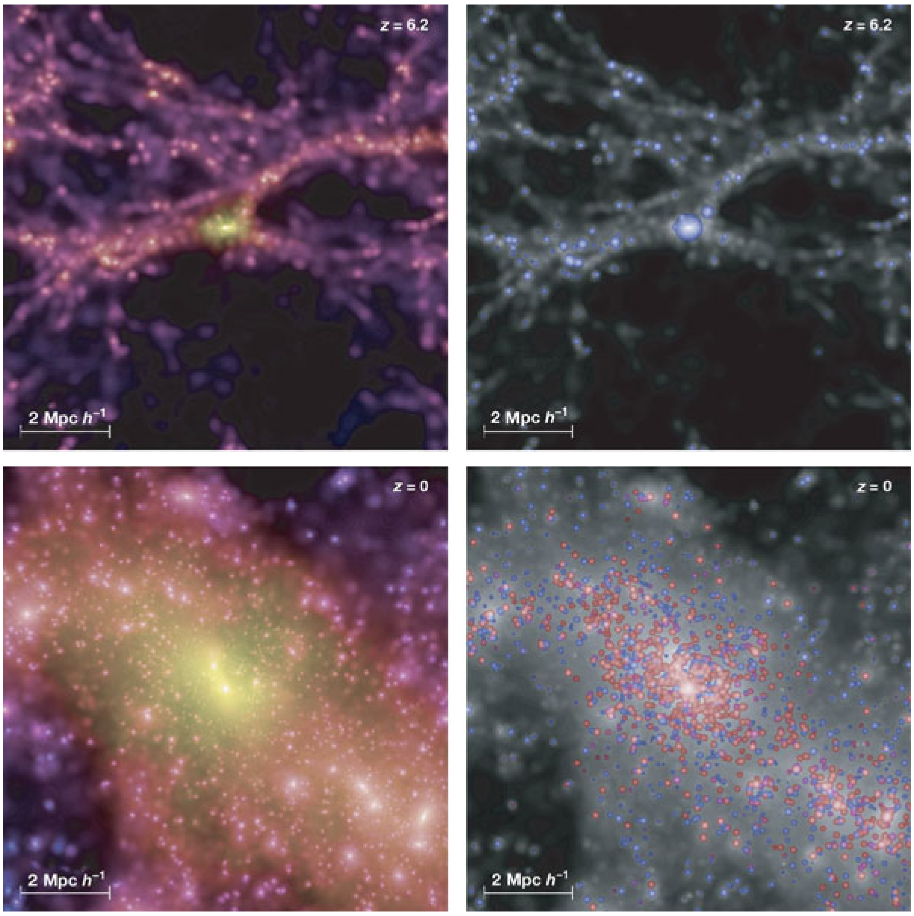

Figure 2.6: Snapshots of environment of first quasar candidate at high and low redshifts (Figure 3 of Springel et al. 2005). The two panels on the left side show the projected dark matter distribution in a cube of co-moving sidelength $10h^{-1}$ Mpc, color-coded according to density and local dark matter velocity dispersion. The panels on the right side show the galaxies of the semi-analytic model overlaid on a greyscale image of the dark matter density. The volume of the sphere representing each galaxy is proportional to its stellar mass, and the chosen color encode the rest frame stellar B-V color index. While at $z = 6.2$ (two top panels) all galaxies appear blue owing to ongoing star formation, many of the galaxies that have fallen into the rich cluster at $z = 0$ (two bottom panels) have turned red. Reprinted by permission from Macmillan Publishers Ltd: Nature (Springel et al., 2005, Nature, Volume 435, Issue 7042, pp. 629-636), copyright 2005.

clusters.

Several such candidates, i.e., QSOs in BCGs, include H 1821+643 (or E1821+643) (Kii et al. 1991; Yamashita et al. 1997; Jiménez-Bailón et al. 2007; Russell et al. 2010), 3C 186 (Siemiginowska et al. 2010), PKS 1229-021 (Russell et al. 2012), IRAS 09104+4109 (Iwasawa et al. 2001; Vignali et al. 2011; O'Sullivan et al. 2012), IRAS F15307+3252 (Iwasawa et al. 2005), and the Phoenix cluster (McDonald et al. 2012, 2013a; Ueda et al. 2013a). Note, however, that the number of the sources is very limited, and thus systematic studies have little been done. We attempt to do such a study in our work, with a particular interest on the AGN fraction and type 2 fraction of the SMBHs in BCGs.

2.4 AGN Feedback to the Intracluster Medium

As mentioned in Section 2.1.2, cooling flows in most of clusters of galaxies are suppressed by some mechanisms. Heating of the ICM by radiation or jets from AGNs is considered to be one of the most promising explanation for it. This mechanism, the AGN feedback, is classified into two modes; one is radiative mode, the other is kinetic mode (Fabian 2012).

The kinetic mode operates for AGNs with powerful jets. We know many radio-lound AGNs with jets in the BCGs of clusters in the local Universe, e.g., NGC 1275, PKS 0745-191, Hydra A, M 87, and so on (e.g., Valentijn & Bijleveld 1983; Jones & Forman 1984; Pedlar et al. 1990; Ball et al. 1993; Fabian 1994; Rafferty et al. 2006). Therefore, the kinetic mode is considered to be the primary AGN feedback at least in the local Universe. A relic of heating of the ICM by jets can be observed as an X-ray cavity in the ICM at the center, which is lower luminosity than surrounding region, i.e., the electron density is relatively small. The X-ray cavity was first discovered around NGC 1275, a cD galaxy and also the BCG of the Perseus cluster, with *Einstein* (Branduardi-Raymont et al. 1981; Fabian et al. 1981). Similar structures were found with the *ROSAT*/HRI in other bright clusters with cD galaxies (e.g., Carilli et al. 1994; Rizza et al. 2000). *Chandra* high angular resolution images have enabled us to observe more details of such structures, resulting in discovery of the X-ray bubbles in the ICM (e.g., Fabian et al. 2000; McNamara et al. 2000). The detection frequency of an X-ray cavity around a cD galaxy at the center is $\sim 20 - 30\,\%$ (Bîrzan et al. 2004; Rafferty et al. 2006). The detection rate is as high as $\sim 70\,\%$ (12/17) if we limit the sample to the clusters with a strong cooling rate (Dunn et al. 2005). Note that a significant fraction of clusters have a low temperature component in their cores, called a cool-core. The cool-core has a short cooling time, i.e., strong cooling rate. In some cases, the term of cooling flow rate has been used instead of the cooling rate, though it does not mean there is a cooling flow.

The energy required to create an X-ray cavity in ICM is the sum of the pV work required to displace the ICM at the region and the internal energy E of the hot gas remained in the cavity. This could be called enthalpy H denoted as

$$H = E + pV = \frac{\gamma}{\gamma - 1} pV, \tag{2.17}$$

where p is the pressure of the surrounding ICM, V is the volume of the cavity, and γ is the adiabatic index of the hot gas inside the cavity, respectively. If relativistic particles are filled in the cavity $\gamma = 4/3$ and thus $H = 4pV$ is expected, whereas if it is dominated by non-relativistic gas $\gamma = 5/3$ and $H = 2.5pV$ are predicted. The cavity may also be dominated by magnetic field, in which case $H = 2pV$ should be valid (e.g., Dunn & Fabian 2004; Bîrzan et al. 2004). The mechanical power of a cavity is defined as $H/t_{\rm age}$, where t_{age} is the time scale of the formation of the cavity. Rafferty et al. (2006) reported that the mean cooling rate is $6.45 \times 10^{44}\,\text{erg}\,\text{s}^{-1}$ for a sample of clusters, while the mean mechanical power of their cavities is estimated to be $1.01 \times 10^{45}\,\text{erg}\,\text{s}^{-1}$ by assuming $4pV$. It indicates that heating of the particles from AGNs can balance or overcome the ICM cooling. Extensive works (e.g., Nulsen et al. 2007; McNamara & Nulsen 2007; Hlavacek-Larrondo et al. 2012; Fabian 2012) have suggested this point of view is basically correct. Furthermore, McNamara & Nulsen (2007) examined the relation between the mechanical power of cavities and the luminosity of the ICM within r_{cool} at which the cooling time is $7.7 \times 10^{9}\,\text{yr}$. The relation is consistent with the assumption of $H = 4pV$ in most of the cases, supporting the idea that the ICM cooling can be balanced by the AGN mechanical power (e.g., Rafferty et al. 2006; McNamara & Nulsen 2007; Hlavacek-Larrondo et al. 2012).

According to Fabian (2012), the other radiative mode is considered to be the effective feedback for AGNs of which luminosity is within two orders of magnitude of the Eddington limit. The Eddington limit (or Eddington luminosity, L_{Edd}) is described as

$$L_{\text{Edd}} = \frac{4\pi G M c m_{\text{p}}}{\sigma_T} = 1.25 \times 10^{38} \left(\frac{M_{\text{BH}}}{M_{\odot}}\right) \ \text{erg}\,\text{s}^{-1}, \tag{2.18}$$

where σ_T is the Thomson cross section ($\sigma_T = 6.65 \times 10^{-25}\,\text{cm}^{-2}$). The radiative mode should be important at $z = 2 \sim 3$, where QSOs activities are peaked (e.g., Richards et al. 2006). On the other hand, since most of the AGNs in the BCGs of clusters at the local Universe has much lower luminosities than the Eddington limit (e.g., NGC 1275 is $\sim 0.4\,\%$; Rafferty et al. 2006), the radiative mode may not be important.

We, however, estimate the heating power in the radiative mode by the following discussions by King (2009) and Siemiginowska et al. (2010). The amount of required energy to heat the ICM within a cool-core of a cluster is of the order of 1 keV per baryon, e.g.,

$$E_{\text{heat}} \sim \left(\frac{1\,\text{keV}}{1\,\text{GeV}}\right) M_{\text{core}} c^2 = 1.78 \times 10^{59} \left(\frac{M_{\text{core}}}{10^{11}\,M_{\odot}}\right) \ \text{erg}, \tag{2.19}$$

where M_{core} is the ICM mass within the core. Sazonov et al. (2005) suggest that photoionization and Compton heating are the dominant processes for radiation to heat the ICM. If we assume, for example, a QSO with luminosity of $10^{47}\,\text{erg}\,\text{s}^{-1}$, which corresponds to the Eddington limit of an SMBH of $10^{9}\,M_{\odot}$, the radiation energy is orders of magnitude larger than typical luminosity of a cluster core. However, the opacity of the ICM is very small. We evaluate the opacity, τ, of the ICM in the core only for Compton scattering, as the lower limit,

$$\tau = n_e r_{\text{core}} \sigma_T = 1.03 \times 10^{-1} \left(\frac{n_e}{10^{-2}\,\text{cm}^{-3}}\right) \left(\frac{r_{\text{core}}}{50\,\text{kpc}}\right) \ \%, \tag{2.20}$$

where n_e is the electron density of the core, $r_{\rm core}$ is the radius of the cluster core, respectively. Therefore, the radiative heating energy balances with the ICM cooling rate if the ICM luminosity is 0.1 % of the QSO luminosity. This is, however, an instantaneous balance. We also have to care about the time scale of the QSO activity. The time scale is not certain, in particular, for QSOs in BCGs, as the sample is very limited. We would attempt to estimate in our study and will show the radiative mode is important in some cases.

Chapter 3

Instruments

We mainly use the data obtained from the *Suzaku*/XIS & HXD, the *Chandra*/ACIS, and the *XMM-Newton*/EPIC for the analyses in this work. We mention a brief introduction to these satellites and instruments installed on them in this section. More details are described in

- *Suzaku*: Mitsuda et al. (2007); Koyama et al. (2007b); Takahashi et al. (2007); Kokubun et al. (2007),
- *Chandra*: Weisskopf et al. (2002); Garmire et al. (2003), and
- *XMM-Newton*: Jansen et al. (2001); Turner et al. (2001); Strüder et al. (2001),

respectively.

3.1 *Suzaku*

3.1.1 Overview

Suzaku[1] (Mitsuda et al. 2007) is the Japanese fifth X-ray observatory. *Suzaku* was developed by the Institute of Space and Astronautical Science (ISAS) of Japan Aerospace Exploration Agency (JAXA) in collaboration with the National Aeronautics and Space Administration's Goddard Space Flight Center (NASA/GSFC) and many other institutions. It was launched on July 10, 2005 by JAXA with the M-V rocket (Japanese solid-fueled rocket) from the Uchinoura Space Center (USC). After deploying its solar paddles and the extensible optical bench (EOB), *Suzaku* was put into a low earth orbit at 570 km altitude with an inclination angle of 31° . The orbital period is about 96 minutes. Figure 3.1 shows the schematic views of the *Suzaku* satellite.

---

[1] `http://www.astro.isas.jaxa.jp/suzaku/doc/suzaku_td/`

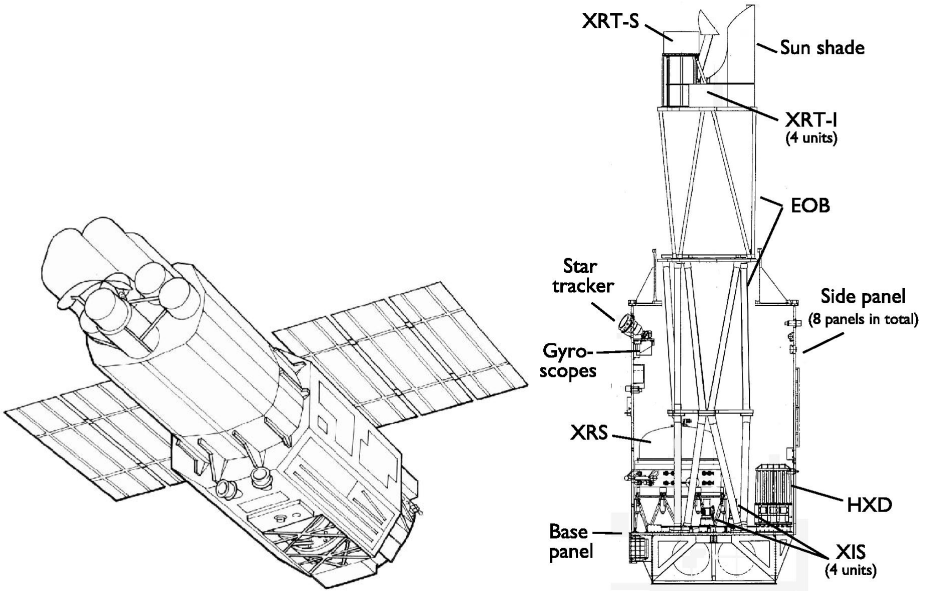

Figure 3.1: Schematic views of *Suzaku* (Figure 1 and 2 of Mitsuda et al. 2007).

Suzaku includes three scientific instruments; four X-ray CCD cameras (X-ray Imaging Spectrometer, XIS; Koyama et al. 2007b), the Hard X-ray Detector (HXD; Takahashi et al. 2007; Kokubun et al. 2007), and the X-ray micro-calorimeter (XRS; Kelley et al. 2007). Each of the XIS is on a focal plane of an X-ray Telescope (XRT; Serlemitsos et al. 2007) that is installed on the top plate of the EOB. The effective energy band of the XIS is $0.2-12$ keV (Koyama et al. 2007b), while the HXD extends the bandpass of the observatory to much higher energies ($10-600$ keV Takahashi et al. 2007; Kokubun et al. 2007). Although the XRS has a superior energy resolution (7 eV in the energy range of $0.3-12$ keV), the system became inoperable due to a thermal short between the helium and neon tanks, which resulted in the vent of the liquid helium coolant into space.

3.1.2 X-ray Imaging Spectrometer (XIS)

The XIS consists of four sensors (XIS0, 1, 2, and 3). All sensors were developed through the collaboration among the Center for Space Research at Massachusetts Institute of Technology (MIT), ISAS/JAXA, Osaka University, Kyoto University, Rikkyo University, Kogakuin University, and Ehime University. The XIS employs sensitive silicon charge-coupled device (CCD), which is operated in a photon counting mode (Tanaka et al. 1994).

The left panel of Figure 3.2 shows a sketch image of the *Suzaku*/XIS camera body, while the right panel of Figure 3.2 displays the sensor sketch of the XIS CCD (Koyama et al. 2007b). Each sensor has a single CCD chip with an array of 1024×1024 pixels, and

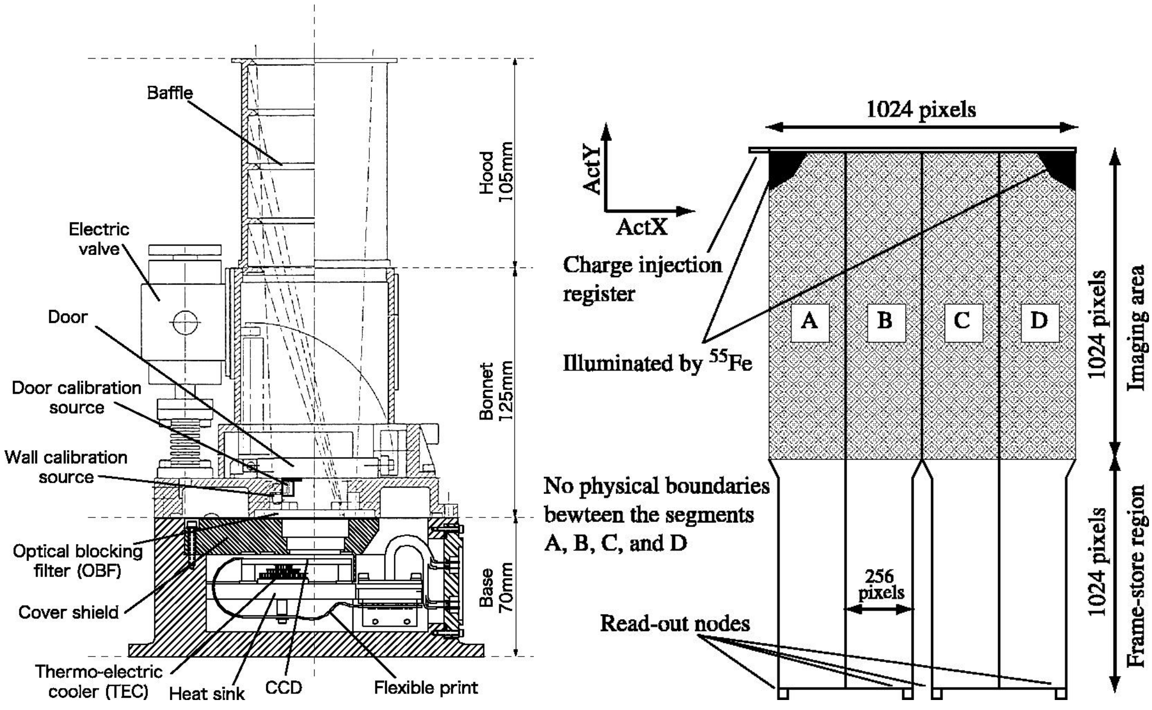

Figure 3.2: Cross section of the *Suzaku*/XIS camera body (left panel) and the schematic view of the XIS CCD (right panel) (Figure 2 and 3 of Koyama et al. 2007b).

a field of view (FOV) of the XIS is $17'.8 \times 17'.8$ region on the sky combined with the XRT. Each pixel size is $24\,\mu$m square, and the size of the CCD is $25\,\mathrm{mm} \times 25\,\mathrm{mm}$. A back-illuminated (BI) CCD is adopted for XIS1, while the others (XIS0, XIS2, and XIS3) are the front-illuminated (FI) CCDs. Figure 3.3 shows the effective area of the XIS+XRT. The basic properties of the XIS are summarized in Table 3.1.

Table 3.1: Basic Performance of the XIS

Energy range	0.2 – 12 keV
Energy resolution (FWHM)	~ 130 eV at 5.9 keV
Field of view	$17'.8 \times 17'.8$
Effective area	330 cm^2 (FI), 370 cm^2 (BI) at 1.5 keV
PSF (HPD)	$2'$
CCD format	1024×1024
Timing resolution	8 s (normal mode)

Since XIS2 was damaged on November 9, 2006, 1:03 UT by a micrometeorite, about 2/3 of the imaging area became suddenly unusable. The anomalous area was flooded with

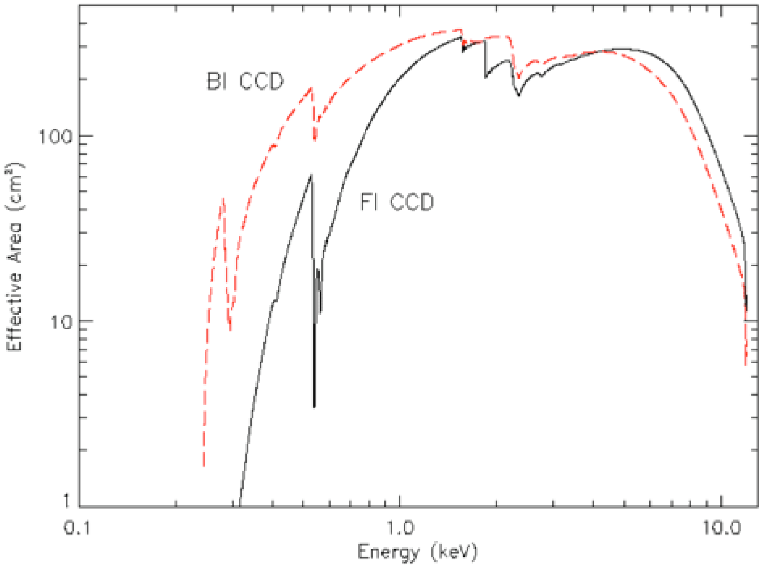

Figure 3.3: Effective area of the XIS (Figure 3 of Mitsuda et al. 2007). The black solid line shows the effective area of the XIS FI CCD. The red dashed line shows that of the XIS BI CCD (i.e. XIS1).

a large amount of charge. In spite of efforts by the *Suzaku* team, XIS2 has not yet been recovered. Therefore, we used only XIS0, 1, and 3 data in this work.

3.1.3 Hard X-ray Detector (HXD)

The Hard X-ray Detector (HXD; Takahashi et al. 2007; Kokubun et al. 2007) is a non-imaging, collimated detector covering a high energy band of $10 - 600\,\mathrm{keV}$. It has been developed jointly by the University of Tokyo, Aoyama Gakuin University, Hiroshima University, ISAS/JAXA, Kanazawa University, Osaka University, Saitama University, SLAC, and RIKEN. The HXD consists of two detectors, i.e. the HXD-PIN and the HXD-GSO. The energy band of the HXD-PIN is below 60 keV, while that of the HXD-GSO is above 40 keV. The effective areas of the HXD-PIN and the HXD-GSO are $\sim 160\,\mathrm{cm}^2$ at 20 keV, and $\sim 260\,\mathrm{cm}^2$ at 100 keV, respectively. The basic performance of the HXD is summarized in Table 3.2.

Table 3.2: Basic Performance of the HXD

Energy range	$10 - 600\,\mathrm{keV}$
Energy resolution (FWHM)	$\sim 4.5\,\mathrm{keV}$ (PIN) and $7.6/\sqrt{E_{\mathrm{MeV}}}\%$ (GSO)
Field of view	$4.^\circ5 \times 4.^\circ5 \gtrsim 100\,\mathrm{keV}$ and $34' \times 34' \lesssim 100\,\mathrm{keV}$
Effective area	$\sim 160\,\mathrm{cm}^2$ at 20 keV (PIN) and $\sim 260\,\mathrm{cm}^2$ at 100 keV (GSO)
Timing resolution	$61\,\mu\mathrm{s}$

3.2 *Chandra*

3.2.1 Overview

The *Chandra* X-ray Observatory[2] (Weisskopf et al. 2002), named in honor of Dr. Subrahmanyan Chandrasekhar, is the X-ray satellite of NASA's four Great Observatories. *Chandra* was launched and deployed by NASA's Space Shuttle *Columbia* on July 23, 1999. It was released into an elliptical orbit, whose the apogee is ∼138,800 km and the perigee is ∼10,100 km. An uninterrupted exposure time is larger than 170 ks due to its orbital period is 63.5 hours. The outline image of *Chandra* is shown in Figure 3.4.

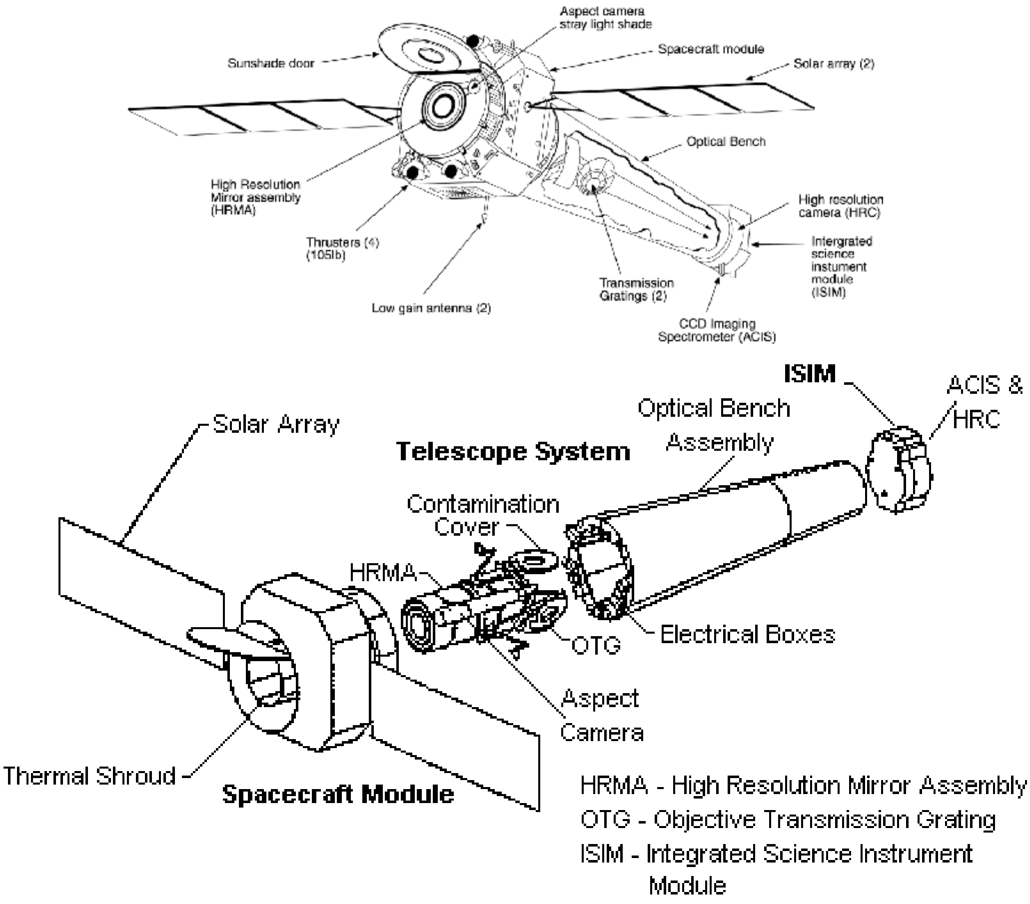

Figure 3.4: Schematic and expanded view of *Chandra*. The top panel shows the labelled sketch of *Chandra* (`http://chandra.harvard.edu/chronicle/080999/weekend.html`). The bottom panel shows the expanded view of the *Chandra* flight system (Figure 1 of Weisskopf et al. 2002).

Chandra includes four types of scientific instruments: the Advanced CCD Imaging

---

[2] http://chandra.harvard.edu/press/fact1.html

Spectrometer (ACIS; Garmire et al. 2003), the High Resolution Camera (HRC; Murray et al. 1998), the Low Energy Transmission Grating Spectrometer (LETGS; Brinkman et al. 2000), and the High Energy Transmission Grating Spectrometer (HETGS; Canizares et al. 2005). The ACIS is one of the two instruments installed on a focal plane, which is an array of CCDs. The HRC is another instrument used at the focus of the High Resolution Mirror Assembly (HRMA; van Speybroeck et al. 1997; Weisskopf & O'dell 1997; Zhao et al. 1997). The LETGS and the HETGS are activated by swinging an assembly into position behind the mirrors. The LETGS is designed to cover an energy range of 0.08 to 2 keV, while the HETGS functions in $0.4-10$ keV. Among these instruments, we used the data obtained with the ACIS. In the following section, we present a brief introduction to the ACIS.

3.2.2 Advanced CCD Imaging Spectrometer (ACIS)

The Advanced CCD Imaging Spectrometer (ACIS; Garmire et al. 2003) consists of ten CCDs manufactured by MIT Lincoln Laboratory. Those are three-phase frame transfer CCDs (Burke et al. 1997). Four of the ten chips are 2×2 mosaic array on a focal plane used for imaging (ACIS-I), the others form 1×6 array used either as an imaging or a grating detector (ACIS-S). Figure 3.5 shows schematic views of the ACIS-I and the ACIS-S. Two BI CCDs are used for the ACIS-S, while the rest of the ACIS-S and all of the ACIS-I are FI CCDs. There are two choices for the on-axis position of the HRMA, i.e., one is ACIS-S3 and another is ACIS-I3. Due to the telemetry limits, only six chips can be activated in observation. Since a BI CCD has superior quantum efficiency in the low energy band, it is adopted at the nominal aim point of the ACIS-S. The ACIS-S has the benefit to observe a target whose spectrum is dominated by low energy emission. The most valuable performance of the ACIS is an angular resolution of $0.5''$ in $0.2-10$ keV combined with the HRMA. The FOV is $17' \times 17'$. Other characteristics are summarized in Table 3.3 and the effective areas for the on-axis ACIS (i.e. ACIS-I3 and ACIS-S3) are shown in Figure 3.6.

The ACIS was damaged by cosmic soft proton (~ 100 keV) after the ACIS door was opened on day 252 of 1999. Since the radiation damage caused a serious increase of the charge transfer inefficiency (CTI) for the FI CCDs (Garmire et al. 2003), their energy resolution were degraded from the pre-launch values of about 150 eV to about 260 eV (at the summer of 2009) even after the CTI correction. However, the angular resolution of the ACIS is not degraded by the radiation damage. The X-ray imaging quality of the ACIS is significantly higher than any other X-ray observatories at the time of writing.

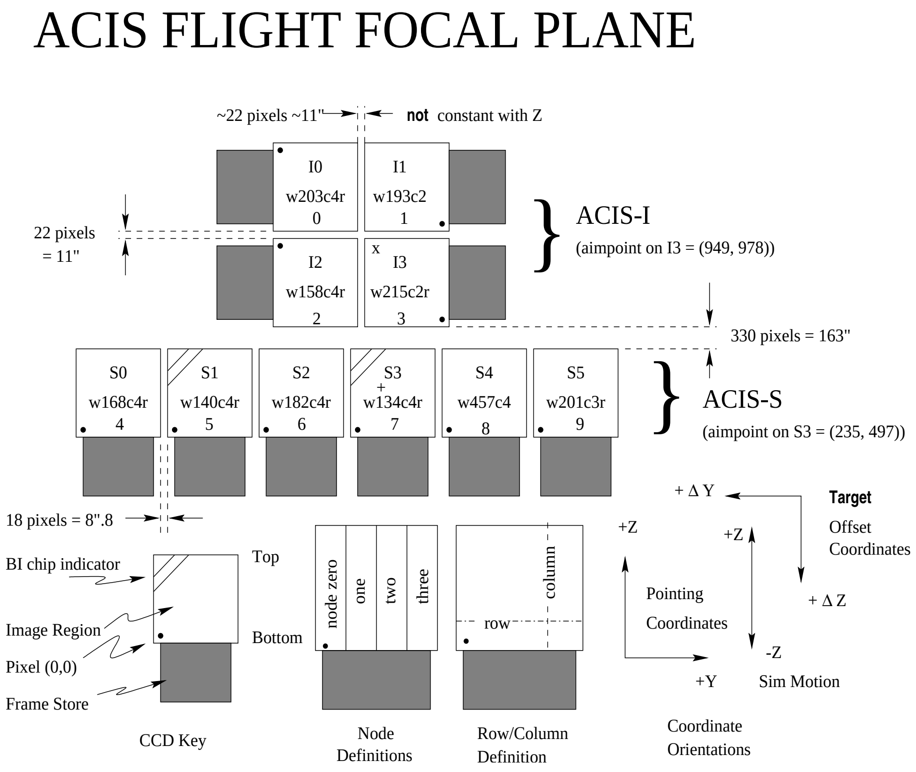

Figure 3.5: Schematic views of the ACIS-I and the ACIS-S (top view) (`http://cxc.harvard.edu/proposer/POG/html/ACIS.html`).

Table 3.3: Basic Performance of the ACIS

Energy resolution	$\sim 150\,\text{eV}$, $\sim 280\,\text{eV}$ after damaged at $5.9\,\text{keV}$
Field of view	$16'.9 \times 16'.9$
Effective area	$600\,\text{cm}^2$ at 1.5 keV, $40\,\text{cm}^2$ at $8.0\,\text{keV}$
PSF (FWHM)	$0.5''$
CCD format	1024×1024
Time resolution	3.2 sec (full frame)

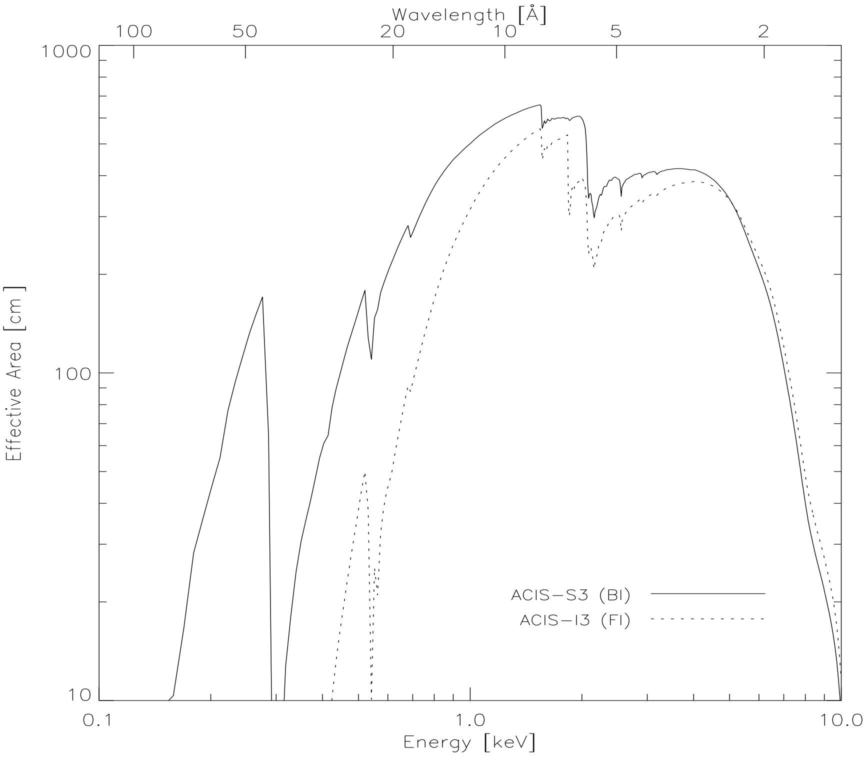

Figure 3.6: Effective areas of the ACIS (`http://cxc.harvard.edu/proposer/POG/html/ACIS.html`). The solid line shows the effective area for ACIS-I3, and the dashed line is that for ACIS-S3.

3.3 *XMM-Newton*

3.3.1 Overview

X-ray Multi-Mirror Mission (XMM) - Newton (hereafter *XMM-Newton*[3]; Jansen et al. 2001) is the second X-ray astronomy mission of European Space Agency (ESA). It was launched on December 10, 1999, by ESA with Ariane 504 from the Guiana Space Centre, Europe's space port (French Guiana) and put into a highly elliptical orbit with an apogee of about 115,000 km and a perigee of 6,000 km with an inclination angle of 54.3° . The orbital period is 47.9 hours. Figure 3.7 shows the sketch of the *XMM-Newton*.

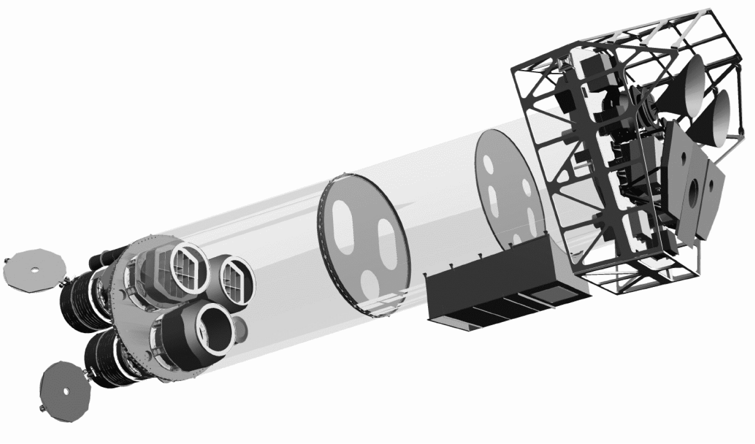

Figure 3.7: Sketch of the *XMM-Newton* observatory. To the left the three mirror modules (with the Reflection Gration Arrays mounted behind two of them) can be seen, while at the right the back-end of the instrument platform with all the radiators is visible (Figure 1 of Jansen et al. 2001).

XMM-Newton includes three types of scientific instruments: European Photon Imaging Camera (EPIC; Turner et al. 2001; Strüder et al. 2001), Reflection Grating Spectrometer (RGS; den Herder et al. 2001), and Optical/UV Monitor (OM; Mason et al. 2001). The EPIC has the performance of X-ray imaging and moderate energy resolution. The EPIC consists of two different types of CCD camera called MOS (Metal Oxide Semi-conductor; Turner et al. 2001) and PN (Strüder et al. 2001). The RGS includes two essentially identical spectrometers for high-resolution X-ray spectroscopy and spectrophotometry. Both the EPIC and the RGS are on the focal plane of the X-ray telescopes, while the OM has its own telescope. The OM is a optical/UV detector for imaging and grism spectroscopy. Among these instruments, we used the data obtained with the EPIC.

---

[3] `http://xmm.esac.esa.int/external/xmm_user_support/documentation/technical/`

The overview of the EPIC is described in the following section.

3.3.2 European Photon Imaging Camera (EPIC)

The EPIC consists of three cameras: two MOS cameras (called MOS1 and MOS2) and one PN camera. FI CCDs are used for the MOS, while the PN employs BI CCDs. Figure 3.8 shows schematic views of the FOV of the EPIC; MOS (left) and PN (right). The QE and the timing resolution of PN CCD are better than those of MOS CCDs, while MOS CCDs has better spectral resolution than that of PN CCD. Figure 3.9 shows the effective area of each camera. The basic properties of the EPIC are summarized in Table 3.4.

The event on March 9, 2005 caused an anomaly of the MOS1 CCD-6. Thus, the MOS1 is currently operated with the power of the CCD-6 off. Since the reason of this anomaly is unknown, the instruments team of the MOS considered that a micrometeorite impacted the MOS1 CCD-6.

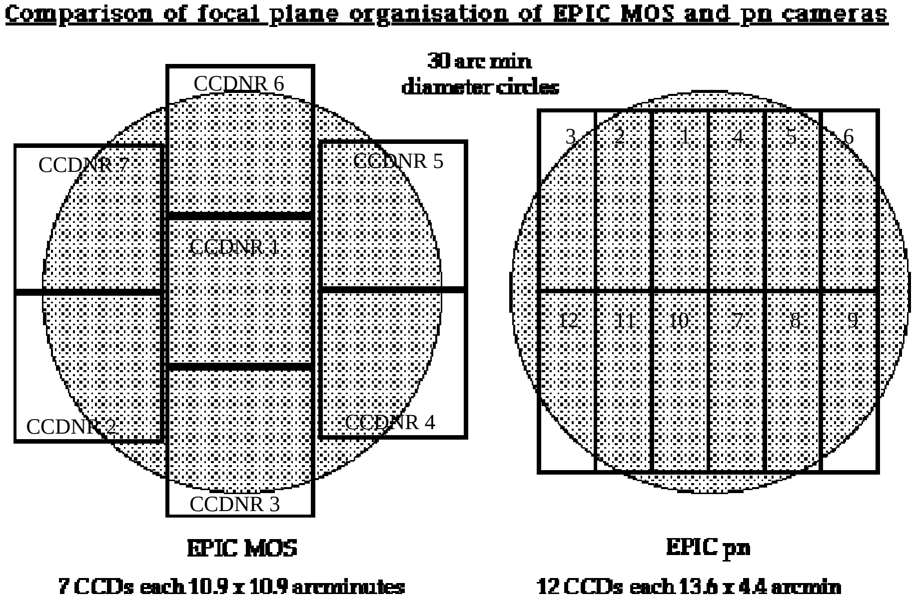

Figure 3.8: Schematic views of the FOV of the EPIC. The shaded circle shows a $30'$diameter area. The left panel shows the FOV of the MOS, while the right panel shows that of the PN. (`http://xmm.esac.esa.int/external/xmm_user_support/documentation/uhb/epic.html`)

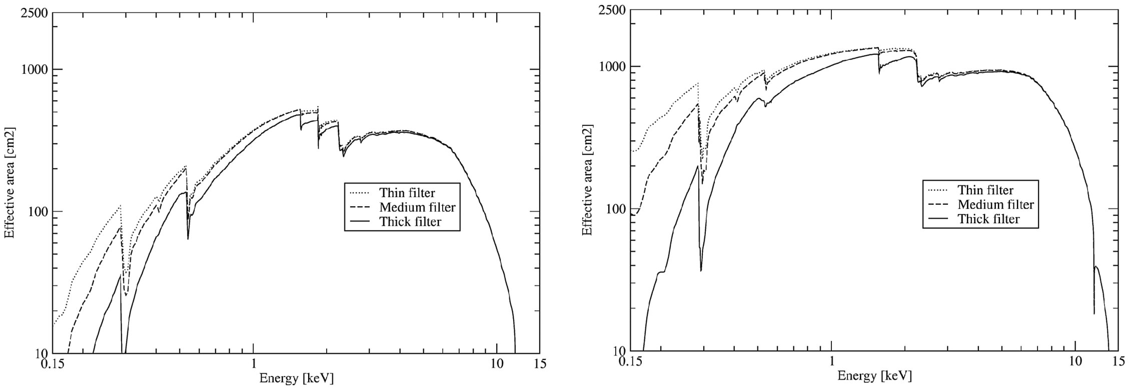

Figure 3.9: Effective area of the EPIC. The left panel shows the effective area of the MOS, while the right panel shows that of the PN (`http://xmm.esac.esa.int/external/xmm_user_support/documentation/technical/EPIC/index.shtml`).

Table 3.4: Basic Performance of the EPIC

	EPIC MOS	EPIC PN
Illumination type	Front illuminated	Back illuminated
Energy range	$0.15 - 12\,\mathrm{keV}$	$0.15 - 15\,\mathrm{keV}$
Energy resolution (FWHM)	$\sim 140\,\mathrm{eV}$ at $5.9\,\mathrm{keV}$	$\sim 170\,\mathrm{eV}$ at $5.9\,\mathrm{keV}$
Field of view	$30'$ diameter	$30'$ diameter
PSF (HPD)	$14''$	$15''$
CCD format	600×600	398×384
Timing resolution	2.5 sec (full frame)	73.4 ms (full frame)

Chapter 4

Search for Luminous AGNs in the Brightest Cluster Galaxies

In this chapter, we search for luminous AGNs in the BCGs by referring both the *Planck* SZ cluster catalogue and the *Swift*/BAT 70-Month catalogue. Both the catalogues are complete enough for us to find our targets without suffering sample bias. We then obtain a fraction that the SMBHs in the BCGs are highly luminous AGNs with the largest and least biased sample ever used. We briefly introduce both the catalogues and the procedure of the collation, and show a list of 18 candidates. Examination of those candidates yields two BCGs hosting luminous AGNs.

4.1 *Planck* SZ Cluster Catalogue

The *Planck* satellite (Planck Collaboration et al. 2011, 2013a) is a mission of European Space Agency (ESA) to measure the spatial anisotropies in temperatures of the cosmic microwave background (CMB; Penzias & Wilson 1965) with improved resolution and sensitivity. *Planck* was launched on 2009 May 14 and had been scanning the all-sky for nearly 4.5 years since August 2009. The satellite carried two kinds of scientific instruments; one is the High Frequency Instrument (HFI) consisting of 52 bolometric detectors senetitive to 83∼1000 GHz, and the other is the Low Frequency Instrument (LFI) which is an array of 22 radio receivers sensitive to 22∼77 GHz. Only the LFI was operated in the last stage of the mission. The mission aimed to reveal the early history of the Universe, to test the inflation cosmology (e.g., Sato 1981; Guth 1981), and to determine the Hubble constant. Measurement of the Sunyaev-Zel'dovich (SZ) effect (Sunyaev & Zeldovich 1972, 1980), in particular, toward clusters of galaxies was also the target.

The SZ effect is a distortion of CMB spectrum with inverse Compton scattering of

CMB photons by electrons in the hot gas along the line of sight. The distortion is proportional to the pressure of hot gas integrated along the line of sight, not depend on the distance of the hot gas. Therefore cluster search through the SZ effect has an advantage over X-ray or optical surveys to detect distant clusters. An all sky catalogue of such SZ sources was recently released by Planck Collaboration et al. (2014) [1]. The catalogue contains 1227 sources, in which 683 sources of previously known clusters, 178 sources of *Planck* new clusters, and 366 sources of cluster candidates are included, derived from the SZ effect detections using the first 15.5-Month of *Planck* observations. As was expected, the catalog contains distant clusters up to $z \sim 1$, of which mass range from 0.1×10^{15} to $1.6 \times 10^{15}\, M_{\odot}$. Although the catalogue consists of several tables with slightly different criteria, we employ the *Planck* SZ cluster catalogue of `COM_PCCS_SZ-union_R1.11.fits`.

Since our aim is to search for luminous AGNs (radio-quiet or radio-loud) in BCGs in lusters, we need special care about point-source contamination in compilation of the *Planck* SZ catalogue. In prior to the SZ detection of sources, point-sources were masked from the *Planck* maps of each HFI frequency channel. The size of mask was 1.28 FWHM of the beam size, which ranges from about $6'$ to $12'$ (Planck Collaboration et al. 2013b, 2014). According to Planck Collaboration et al. (2014), however, bright radio sources at the center of clusters have steep spectra and hence are not bright in high frequency channels. The Perseus cluster was one exception, with a point source that is so bright that the cluster was masked and thus not included in the catalogue. In Planck Collaboration et al. (2014), the *Planck* SZ catalogue was compared with various catalogues of X-ray or optical surveys of clusters. Comparison with the Meta-Catalogue of X-ray detected Clusters of galaxies (MCXC; Piffaretti et al. 2011) indicated that 11 clusters that should have been detected in the *Planck* SZ catalogue but were not. Because they are due to the point-source masks. For other two X-ray clusters, RXC J1253.6-3931 and RXC J1958.2-3011, the *Planck* SZ detections were hampered by contaminations of radio sources. In the case of RXC J1253.6-3931, Plagge et al. (2010) reported that it is associated with a radio bright Parkes-MIT-NRAO Survey source that would have been difficult to remove from the SZ maps measured by SPT. Several other clusters expected to be detected but not included in the *Planck* SZ catalogue should be regarded as overestimation of the SZ signals from the X-ray data owing to contaminations of X-ray flux from AGNs or prominent cool cores of clusters. We should examine these missing clusters in more detail with referring the point sources detected listed in the *Planck* catalogue of compact sources (Planck Collaboration et al. 2013c).

Significant fraction (19 out of 25) of nearest ($z < 0.03$) MCXC clusters were not

---

[1] `http://www.sciops.esa.int/index.php?project=planck&page=Planck_Legacy_Archive`

included in the *Planck* SZ catalogue (Planck Collaboration et al. 2014), either. Some of them fell into the point-source masks (the Perseus cluster, Abell 1060 (the Hydra cluster) and so on) or into the galactic plane mask (the Ophiuchus cluster and 3C 129.1). Remaining, including the Virgo cluster, were below the SZ detection threshold. However, since we know very luminous AGNs are not found in these nearby clusters, our results are not affected by these nearby clusters not included in the *Planck* SZ catalogue.

4.2 *Swift*/BAT 70-Month Catalogue

The *Swift* satellite (Gehrels et al. 2004) is a multiwavelength observatory for gamma-ray burst (GRB; Klebesadel et al. 1973) astronomy projected by NASA. *Swift* was launched on 2004 November. The Burst Alert Telescope (BAT; Barthelmy et al. 2005) on board *Swift* is a wide field of view (1.4 sr) hard X-ray detectors with a coded mask, design to detect GRBs and localize the burst direction to an accuracy of $1-4$ arcmin within 20 s after the start of the event. The BAT has a sensitivity limit of a few times $10^{-11}\,\mathrm{erg\,cm^{-2}\,s^{-1}}$ in the $14-195$ keV band with a medium positional uncertainty of $1.7'$ (Barthelmy et al. 2005). While searching for GRBs, the *Swift*/BAT performs an all-sky hard X-ray survey. The *Swift*/BAT team have published several complete catalogues so far; 3-Month catalogue (Markwardt et al. 2005), 9-Month catalogue (Tueller et al. 2008), 22-Month catalogue (Tueller et al. 2010), 39-Month catalogue (Cusumano et al. 2010a), 54-Month catalogue (Cusumano et al. 2010b), and 70-Month catalogue (Baumgartner et al. 2013), respectively. In this chapter, we employ the *Swift*/BAT 70-Month catalogue[2].

The *Swift*/BAT 70-Month catalogue contains 1171 hard X-ray sources in the $14-195$ keV band (Baumgartner et al. 2013), which is the most complete hard X-ray source catalogue at present. The 70 month *Swift*/BAT survey covers sources brighter than $1.03\times10^{-11}\,\mathrm{erg\,cm^{-2}\,s^{-1}}$ over 50 % of the sky, and those brighter than $1.34\times10^{-11}\,\mathrm{erg\,cm^{-2}\,s^{-1}}$ over 90 % of the sky (Baumgartner et al. 2013). Baumgartner et al. (2013) reported that the 5σ sensitivity of the 70 month survey is 0.38 mCrab or $9.2\times10^{-12}\,\mathrm{erg\,cm^{-2}\,s^{-1}}$ using the medium exposure time of 9.45 Ms, where 1 Crab corresponds to a flux of $2.386\times10^{-8}\,\mathrm{erg\,cm^{-2}\,s^{-1}}$.

---

[2] `http://swift.gsfc.nasa.gov/results/bs70mon/`

4.3 Search for Luminous AGNs in the *Planck* SZ Clusters

We search for luminous AGNs hosted by BCGs in the *Planck* SZ clusters by collating the *Planck* SZ cluster catalogue (Planck Collaboration et al. 2014) with the *Swift*/BAT 70-Month catalogue (Baumgartner et al. 2013). The *Planck* SZ cluster catalogue, the most complete cluster catalogue through the SZ effect at present, is less affected by selection bias and covers distant clusters than those of optical or X-ray surveys. We consider that hard X-ray surveys are appropriate for detecting AGNs by their intrinsic power and *Swift* is the best choice for at present. Note, however, that the angular resolution of *Swift*/BAT is not enough to separate an AGN component, the high energy tail of an ICM thermal component and a possible ICM non-thermal component. Without any other information, the *Swift*/BAT flux should be regarded as the upper limit of the AGN flux.

4.3.1 Search for AGN Candidates in BCGs in Clusters

We employ 861 clusters in the *Planck* SZ cluster cataloguethat were confirmed in follow-up observations (Planck Collaboration et al. 2014) and in the Sloan Digital Sky Survey (SDSS; York et al. 2000) galaxy catalogue. We search for luminous AGNs in *Swift* hard X-ray sources that have a *Planck* SZ cluster as a counterpart with the following procedure.

1. We calculate an angular separation ($\theta_{\rm d}$) between a *Planck* source and a *Swift* source, and select the sources with $\theta_{\rm d} < 0.2^\circ$. A total of 20 *Planck* sources have their counter parts in this way, while the 20 *Swift* sources have their counter parts.

2. We then apply further selection by their redshifts; sources of which redshifts in two catalogues, the redshift ($z_{\rm p}$) listed in *Planck* SZ cluster catalogue and that ($z_{\rm s}$) in *Swift*/BAT 70-Month catalogue, matches within 0.05, i.e., $z_{\rm p} - 0.05 < z_{\rm s} < z_{\rm p} + 0.05$, are selected. The number of the sources selected at this stage is 18. The others are not consistent with the redshift of sources each other.

3. We finally identify counterpart AGNs with sources in the 13th AGN & QSO catalogue[3] (Véron-Cetty & Véron 2010). To identify the counterparts, we calculate the angular separation $\theta_{\rm d}$ between one *Planck* source and one source in the 13th AGN & QSO catalogue, and select the AGNs with $\theta_{\rm d} < 0.2^\circ$. In the selection, we also limit the redshift difference less than 0.05, that is, $z_{\rm p} - 0.05 < z < z_{\rm p} + 0.05$.

---

[3] `http://cdsarc.u-strasbg.fr/viz-bin/qcat?J/A+A/518/A10`

A total of 18 *Planck* SZ clusters detected by the *Swift*/BAT are selected in this procedure. We obtain a total of 19 candidate AGNs in the BCGs as their counterparts as summarized in Table 4.1.

4.3.2 Selection of Luminous AGNs in BCGs in Clsuters

We further examine the 19 AGN candidates we have selected. For the *Planck* SZ cluster PSZ1 G006.45+50.56 (that corresponds to Abell 2029), there are two candidates AGNs. We consider that 2MASX J15110641+0541228 likely corresponds to the BCG with its smaller separation (θ_{d}) from the center of the cluster (column 14 of Table 4.1) than that of 2MASX J15113367+0545479, though further information is needed to conclude it. Nevertheles, the hard X-ray luminosity of the source derived from the *Swift*/BAT catalogue provides the upper limit of that of an AGN in the BCG of the cluster, in any case.

We note that the redshifts of *Planck* SZ cluster, also listed in the column 5 of Table 4.1, do not exactly match those of AGNs in it. For example, the redshift of PSZ1 G339.69-69.34 (i.e., the Phoenix cluster) is 0.62 in the *Planck* SZ source catalogue, while that of its BCG is 0.596 with optical spectroscopy (McDonald et al. 2012). We thus have employed a margin of 0.05 in redshift in the selection procedure mentioned above. The name of the AGNs, column 10 of Table 4.1, are referred to the NASA/Infrared Processing and Analysis Center (IPAC) Extragalactic Database (NED)[4].

We next evaluate contamination of thermal and non-thermal emission from ICM to the hard X-ray flux measured with the *Swift*/BAT. Ajello et al. (2009) and Ajello et al. (2010) examined possible non-thermal emission in clusters detected with the *Swift*/BAT. They evaluated excess hard X-ray emission of the clusters by subtracting the ICM thermal component and the sum of point source contribution, both were evaluated with the *XMM-Newton* observations of the clusters, from the observed *Swift*/BAT spectra. Evidence of the hard excess emission was found inly in the Bullet cluster and Abell 3667 among the sample they selected. According to their analysis, the hard X-ray excess in the Bullet cluster can be due to non-thermal emission from the ICM, while that in Abell 3667 is a high temperature ($kT \sim 13\,\mathrm{keV}$) thermal emission. For other sources, we estimate the thermal and non-thermal emission from the ICM based on previous X-ray observations, and subtract the contribution from the observed flux to derive the AGN flux or its upper limit for each source, where the AGN spectrum is assumed to be a simple power law with a photon index of 2.0.

---

[4] `http://ned.ipac.caltech.edu/`

We finally find only two *Planck* SZ clusters in which the BCGs hosts luminous AGNs ($\log L_{\mathrm{X},14-195} > 45$); one is H 1821+643 and the other is the Phoenix cluster. The source next to these two is Abell 1914, for which only the upper limit of $logL_{\mathrm{X},14-195} < 44.65$ is obtained. In fact, the temperature of the ICM in this cluster is $\sim 9\,\mathrm{keV}$ (Baldi et al. 2007; Maughan et al. 2008) and the X-ray luminosity in $0.6-9\,\mathrm{keV}$ is $3.3\times10^{45}\,\mathrm{erg\,s^{-1}}$ (Maughan et al. 2008). However, Barrena et al. (2013) reported that A 1914 shows a clear recent cluster merger by measuring the spatial and velocity dispersion of 89 member galaxies with optical observation. We thus conclude that the fraction of very luminous AGNs in BCGs in clusters is 2/861. This fraction is important to study evolution of SMBHs in BCGs in clusters. If we simply assume each SMBH get active as these two during a period of its life, the period must be 23 Myr assuming its life is 10 Gyr. Alternatively, these two source may be very peculiar case that AGN activities occurred in the past ($z = 2 - 4.5$; Richards et al. 2006) and stopped later are are happening at the local ($z < 1$) Universe by some reason. We will discuss more details in Chapter 7. We study the X-ray spectra of the Phoenix cluster and H 1821+643 in the following chapter .

Table 4.1: Full Classification of the Sample Objects

ID[1]	Name[2]	R.A.	Dec.	z[3]	Swift source	$L_{\mathrm{X},14-195}$[4]	Distance(°)	Other name[5]	AGN[6]	AGN name[7]	class[8]	B-band[9]	Distance(°)	Non-thermal[10]
17	PSZ1 G006.45+50.56	227.7117	5.7452	0.0766	SWIFT J1510.9+0547	< 44.34	0.0411884	Abell 2029	Y	2MASX J15110641+0541228	-	-19.2	0.0919365	N
-	- -	-	-	-	- -	-	-	- -	Y	2MASX J15113367+0545479	-	-19.1	0.181585	N
122	PSZ1 G044.24+48.66	239.6066	27.2404	0.0894	SWIFT J1558.4+2718	< 43.66	0.031052	Abell 2142	Y	SDSS J155829.36+271714.2	S1.2	-20.3	0.0548952	N
187	PSZ1 G057.84+87.98	194.9238	27.9600	0.0231	SWIFT J1259.7+2755	< 43.66	0.022159	Coma cluster	N	no data	-	-	-	N
224	PSZ1 G067.19+67.44	216.5164	37.8263	0.1712	SWIFT J1426.1+3747	< 44.65	0.061845	Abell 1914	N	no data	-	-	-	N
252	PSZ1 G075.71+13.51	290.2899	43.9749	0.0557	SWIFT J1921.1+4356	< 44.25	0.0290074	Abell 2319	N	no data	-	-	-	N
326	PSZ1 G094.00+27.41	275.5015	64.3429	0.3315	SWIFT J1822.0+6421	45.73	0.0252919	H 1821+643	Y	[HB89] 1821+643	S1.2	-26.5	0.006063	N
407	PSZ1 G110.99+31.74	256.0337	78.6353	0.0581	SWIFT J1704.3+7838	< 43.74	0.006795	Abell 2256	N	no data	-	-	-	N
423	PSZ1 G115.20-72.07	10.4574	-9.3493	0.0555	SWIFT J0041.9-0921	< 43.63	0.0541292	Abell 85	N	no data	-	-	-	N
568	PSZ1 G164.20-38.90	44.7285	13.5400	0.0739	SWIFT J0259.0+1334	< 44.02	0.0435323	Abell 401	N	no data	-	-	-	N
615	PSZ1 G182.42-28.28	63.3551	10.4720	0.0882	SWIFT J0413.5+1027	< 44.11	0.039504	Abell 478	N	no data	-	-	-	-
644	PSZ1 G191.00+06.65	98.7658	22.5197	0.0680	SWIFT J0635.1+2229	< 44.12	0.0302704	CIZA J0635.0+2231	N	no data	-	-	-	-
801	PSZ1 G239.29+24.75	137.2340	-9.6725	0.0542	SWIFT J0908.9-0933	< 44.10	0.0381283	Abell 754	N	no data	-	-	-	N
920	PSZ1 G266.02-21.23	104.6448	-55.9422	0.2965	SWIFT J0658.5-5556	< 43.63	0.014308	Bullet cluster	N	no data	-	-	-	Y
944	PSZ1 G272.08-40.16	67.8092	-61.4070	0.0589	SWIFT J0431.3-6127	< 44.01	0.0544774	Abell 3266	N	no data	-	-	-	N
1118	PSZ1 G316.33+28.55	206.8801	-32.8496	0.0391	SWIFT J1347.5-3254	< 43.71	0.0691377	Abell 3571	N	no data	-	-	-	N
1137	PSZ1 G324.59-11.52	249.5789	-64.3594	0.0508	SWIFT J1638.7-6420	< 44.20	0.0377639	TrA cluster	N	no data	-	-	-	N
1181	PSZ1 G339.69-69.34	356.1703	-42.6983	0.6200	SWIFT J2344.6-4246	46.27	0.0854112	Phoenix cluster	Y	2MASX J23444387-4243124	S2	-24.1	0.028794	N
1184	PSZ1 G340.86-33.36	303.0754	-56.8261	0.0556	SWIFT J2012.0-5648	< 42.52	0.0657339	Abell 3667	N	no data	-	-	-	Y

[1]: ID in the *Planck* SZ source catalogue.

[2]: Source name in the *Planck* SZ source catalogue.

[3]: Redshift listed in the *Planck* SZ source catalogue.

[4]: X-ray luminosity in the $14 - 195\,\mathrm{keV}$ band obtained with the *Swift*/BAT (Baumgartner et al. 2013).

[5]: *Swift* source name listed in the *Swift*/BAT catalogue.

[6]: Flag to indicate there are cunterpart AGNs in the location of the *Planck* SZ cluster.

[7]: AGN name from the NED database.

[8]: AGN classification from the 13th AGN & QSO catalogue (Véron-Cetty & Véron 2010).

[9]: B-band luminosity of AGN written in the 13th AGN & QSO catalogue (Véron-Cetty & Véron 2010).

[10]: Flag to indicate hard X-ray excess from the ICM reported by Ajello et al. (2009, 2010). A hyphen ”-” means no reported by them.

Chapter 5

Luminous AGNs in Brightest Cluster Galaxies

In this chapter, we present the results of the X-ray observations of the AGNs in the Phoenix cluster and H 1821+643. These two sources have been selected as the only cases whose luminous AGNs ($L_{\mathrm{X},14-195} > 1\times10^{45}$ erg s^{-1}) reside in the BCGs of clusters based on our collation of the *Planck* SZ cluster catalogue and the *Swift*/BAT 70-Month catalogue.

5.1 Type 2 QSO in the Central Galaxy of the Phoenix Cluster

In this section, we present the analyses and results of the Phoenix cluster observed with *Suzaku*, *Chandra*, and *XMM-Newton*. The Phoenix cluster is one of the two sources in which luminous AGNs reside in the BCGs of clusters (see Chapter 4.3.2). We have already published the results of the X-ray observations of this source with *Suzaku* and *Chandra* (Ueda et al. 2013a).

5.1.1 Previous Studies on the Phoenix Cluster

The Phoenix cluster was discovered by the South Pole Telescope (SPT; Ruhl et al. 2004; Padin et al. 2008; Staniszewski et al. 2009) via the Sunyaev-Zel'dovich effect, and named as SPT-CL J2344-4243 (Williamson et al. 2011). However, several previous all-sky surveys detected the Phoenix cluster as a point-like source. An X-ray emission from the Phoenix cluster was first reported as 1RXS J234444.1-424319 in the *ROSAT* All-Sky Survey Bright Source Catalogue[1] (Voges et al. 1999).

---

[1] `http://www.xray.mpe.mpg.de/cgi-bin/rosat/src-browser`

This source is classified as Seyfert 2 in the Quasar and AGN Catalog 10th Edition by Véron-Cetty & Véron (2001). The Two Micron All Sky Survey (2MASS; Skrutskie et al. 2006; Huchra et al. 2012) found an extended source 2MASX J23444387-423124, while the Palermo *Swift*/BAT hard X-ray catalog source, 2PSBC J2344.8-4245 (or *Swift* J2344.6-4246[2]), is identified as 2MASX J23444387-423124 (Cusumano et al. 2010b). The $14 - 150\,\mathrm{keV}$ band luminosity was extremely high as $1.4 \pm 0.9 \times 10^{46}\,\mathrm{erg\,s^{-1}}$. The galaxy is located at $(\mathrm{R.A., Dec.}) = (23\mathrm{h}44\mathrm{m}43.9\mathrm{s}, -42\mathrm{d}43\mathrm{m}12\mathrm{s})$, a direction of the Phoenix constellation in the southern sky, and thus its host cluster is called the Phoenix cluster. The redshift of the cluster is $z = 0.596$, and one arcsec corresponds to 6.7 kpc at its distance.

With radio, infrared, optical, ultraviolet, and X-ray observations of the Phoenix cluster, McDonald et al. (2012) reported that the X-ray luminosity within r_{500} and the total mass within r_{200} of this cluster are $8.2 \times 10^{45}\,\mathrm{erg\,s^{-1}}$ in $2 - 10\,\mathrm{keV}$ and $2.5 \times 10^{15}\,M_\odot$, respectively. The r_{200} (or r_{500}) is the radius for which enclosed average density is 200 (or 500) times the critical density of the Universe. Both are exceptionally large compared to the other known clusters.

Using *Hubble Space Telescope* and *Chandra* data (the same data as McDonald et al. 2012), McDonald et al. (2013a) estimated that the star formation rate (SFR) and cooling rate are $798 \pm 42\,M_\odot\,\mathrm{yr^{-1}}$ and $2700 \pm 700\,M_\odot\,\mathrm{yr^{-1}}$ (also from White et al. 1997), respectively. Thus, the SFR is $30 \pm 8\,\%$ of the cooling rate, which is one of the highest among typical cool-core clusters in the local Universe. McDonald et al. (2012) also reported that the central AGN has a luminosity of $\sim 3 \times 10^{45}\,\mathrm{erg\,s^{-1}}$ $(2-10\,\mathrm{keV})$ with a large absorption of $\sim 3.9 \times 10^{23}\,\mathrm{cm^{-2}}$.

Apart from these general features of the Phoenix cluster, no detailed X-ray spectroscopy, especially for the central AGN has been examined so far, probably due to the limited statistics in the previous observations. Furthermore, the *Swift*/BAT hard X-ray, a key band to evaluate the intrinsic luminosity of the AGN, would be contaminated by the thermal plasma in the cluster depending on the plasma temperature. We therefore examined the high-quality data of the deep *Suzaku* observation. To separately examine the central AGN component from the thermal emission of the ICM, we also employed the *Chandra* and *XMM-Newton*-Newton archival data

5.1.2 X-ray Observations of the Phoenix Cluster

A *Suzaku* (Mitsuda et al. 2007) observation of the Phoenix cluster was performed on 2010 November 15-16 (ObsID: 70549010, PI: W. Baumgartner). After the standard data

---

[2] `http://swift.gsfc.nasa.gov/results/bs58mon/SWIFT_J2344.6-4246`

reduction described in section 5.1.3, the exposure times were 62 ks and 47 ks for the XIS and the HXD, respectively.

The XIS data were extracted from the circular region with a radius of $3'$ centered on the BCG of the Phoenix cluster as shown in the top panel of Figure 5.1. For the extracted data, we made the NXB-subtracted light curve of XIS0, 1, and 3 in the $0.4-10$ keV band from the $r < 3'$ region with the time bin size of 1024 s. All the data points are within the range of $\pm 3\,\sigma$ ($\pm 0.10\,\mathrm{counts\,s^{-1}}$) of the mean ($1.08\,\mathrm{counts\,s^{-1}}$), and hence no significant variability (no anomaly) in the data is found, and no flickering event is included.

We also used the *Chandra* archival data of the Phoenix cluster, which are the same data used by McDonald et al. (2012). The observation was carried out on 2011 September 19 (ObsID: 13401, PI: G. Garmire). After standard data reduction mentioned in section 5.1.3, an exposure time of the ACIS-I is 12 ks. The bottom panel of Figure 5.1 shows the central region of the Phoenix cluster observed with the ACIS-I. In addition, we employed the data obtained in the *XMM-Newton* observation of this source performed on 2012 May 28 for an exposure time of 23.4 ks (ObsID: 0693661801, PI: M. Arnaud).

5.1.3 Dara Reductions for the Data of Each X-ray Satellite

In this section, we summarize the procedures of data reduction and spectral analysis for the X-ray data obtained with *Suzaku*, *Chandra*, and *XMM-Newton*. The same procedures are used not only for the data of the Phoenix cluster but also for those of other AGNs whose results are described in following sections and chapters.

Suzaku

All the *Suzaku*/XIS data were reduced with the HEASOFT[3] version 6.12. We reprocessed the data by applying `xispi` to the unfiltered event files with the latest calibration data base (CALDB), Reduction procedures as described in the document provided by the *Suzaku* team [4] were followed. We used `xselect` to extract X-ray images, light curves, and X-ray spectra from the cleaned event data. We excluded regions illuminated by calibration source (^{55}Fe), which is shown in Figure 3.2. The redistribution matrix files (RMFs) and ancillary response files (ARFs) of the XIS were generated with `xisrmfgen`[5] and `xissimarfgen` (Ishisaki et al. 2007), respectively. The non X-ray background (NXB) of the XIS was estimated by using the database of night earth observations with `xisnxbgen` (Tawa et al. 2008).

---

[3] `http://heasarc.gsfc.nasa.gov/lheasoft/`

[4] `http://heasarc.gsfc.nasa.gov/docs/suzaku/analysis/abc/`

[5] `http://heasarc.gsfc.nasa.gov/docs/suzaku/analysis/xisrmfgen.html`

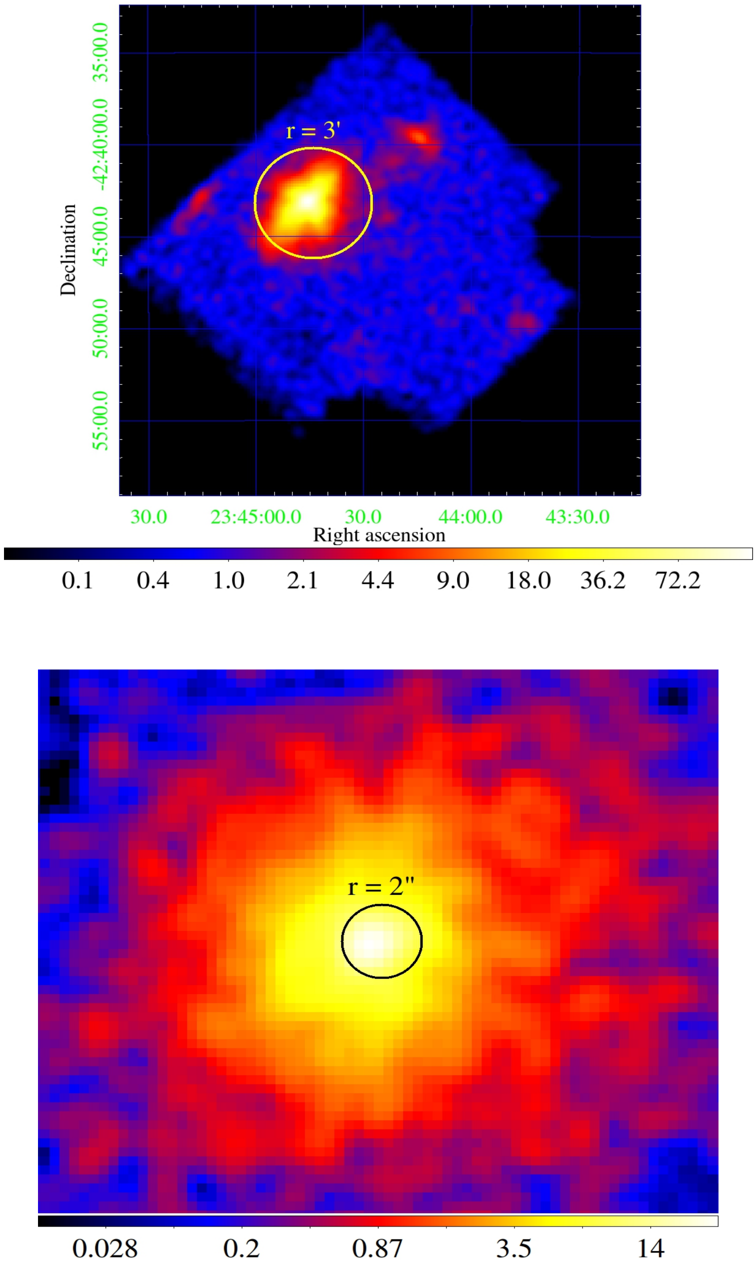

Figure 5.1: X-ray images of the Phoenix cluster in the 0.4 − 10 keV band. The background is not subtracted and the vignetting effect is not corrected. The unit of the color bar is counts pixel^{-1}. Top panel: X-ray image of *Suzaku*/XIS3. The yellow circle shows the region of $r < 3'$. Bottom panel: the *Chandra*/ACIS-I image of the central region of the Phoenix cluster. The image is smoothed with a two-dimensional Gaussian of $\sigma = 3$ pixels. The black line is the $r = 2''$ circle.

The *Suzaku*/HXD data were also reduced with the HEASOFT of the same version as for the XIS data. We carried out the data reprocessing with the latest CALDB and the software `aepipeline`. The following reduction was based on the document by the *Suzaku* team[6]. The modeled NXB data distributed by the *Suzaku*/HXD team in their Web page[7] were employed. The response (RSP) files were also distributed for each observation epoch [8]; we employed `ae_hxd_pinXXXXXe9_20100731.rsp` for the analysis of the Phoenix cluster and 3C 433, `ae_hxd_pinXXXXXe10_20101013.rsp` for ESP 39607, and `ae_hxd_pinXXXXXe11_20110601.rsp` for H 1821+643 and IRAS 09104+4109, where `XXXXX` denotes either of `xinom`, `hxnom`, or `flat`. The RSP files with `xinom` in their name are for the observations at the XIS nominal position, that with `hxnom` are for the the HXD nominal position, whereas that with `flat` are for the CXB flux.

Chandra

We used the *Chandra* archival data of the Phoenix cluster to separate its ICM thermal component and the AGN component. We reprocessed and reduced the level 2 *Chandra*/ACIS-I event data by using the *Chandra* Interactive Analysis of Observations (CIAO) version of 4.4.1 and the CALDB version 4.5.3. The RMFs and ARFs were generated by using `specextract`.

XMM-Newton

We also employed the *XMM-Newton* archival data to measure the temperature and abundance of the ICM in the Phoenix cluster. The *XMM-Newton* data were reduced with the *XMM-Newton* Science Analysis System (SAS) of version 13.0.1 and the current calibration files (CCFs) available at the time of analysis. We extracted X-ray images, light curves, and X-ray spectra with `evselect`. The RMFs and ARFs for the EPIC were generated by using `rmfgen` and `arfgen`, respectively.

5.1.4 Procedures of Spectral Analyses

All the X-ray spectra were analyzed with the XSPEC software (Arnaud 1996) version 6.12. The cosmic X-ray background (CXB, e.g. Giacconi et al. 1962) was modeled with a cut-off power-law model whose parameters were given by Boldt (1987). The normalization of the CXB for the HXD was fixed at the value explicitly supplied by the HXD

---

[6] `http://heasarc.gsfc.nasa.gov/docs/suzaku/analysis/abc/`

[7] `http://www.astro.isas.jaxa.jp/suzaku/analysis/hxd/pinnxb/`

[8] `http://www.astro.isas.jaxa.jp/suzaku/caldb/hxd/`

team[9] from . Other X-ray background components, the Milky Way halo (MWH) and the local hot bubble (LHB), were reproduced with the **APEC** models (Smith et al. 2001) of 0.23 keV and 0.07 keV, respectively, following Ueda et al. (2013b). The abundances of both the components are fixed at 1 solar and the redshifts at 0. These X-ray background components and the Galactic absorption (**wabs** model, Morrison & McCammon 1983) were included in the spectral models used for each spectrum of targets.

The relative normalization of the XIS spectra and that of the HXD were adjusted to the values determined from the cross-calibration based on the observations of the Crab nebula. According to the *Suzaku*Memo [10], the normalization for the HXD-PIN spectrum should be 1.164 times that for the XIS0 spectrum obtained in observations at the XIS nominal position, while the factor is 1.181 for observations at the HXD nominal position.

In this work, we adopt the abundance table of Anders & Grevesse (1989), the Hubble constant of $H_0 = 70\,\mathrm{km\,s^{-1}\,Mpc^{-1}}$, $\Omega_\mathrm{M} = 0.27$, and $\Omega_\Lambda = 0.73$. Unless otherwise specified, all errors in the text and tables represent at 90 % confidence level (90 % CL), while error bars in plots of X-ray spectra are those at 68 % CL.

5.1.5 X-ray Spectral Analyses and Their Results on the Phoenix Cluster

In the analysis of the X-ray spectra obtained with *Suzaku*, the NXB is subtracted. The emission models of the CXB, the MWH, and the LHB are described in section 5.1.3, respectively. A column density of the Galactic absorption (N_H) is estimated to be $1.52 \times 10^{20}\,\mathrm{cm^{-2}}$ with (Kalberla et al. 2005) and we fixed the column density to this value in spectral fitting. Other information is presented in Section 5.1.3.

Suzaku/XIS & HXD Spectra in the $r < 3'$ Region

We show the *Suzaku*/XIS image of the Phoenix cluster field in the top panel of Figure 5.1. The spectra are extracted from the $r < 3'$ region (the solid circle in the top panel of Figure 5.1); those from XIS0 and XIS3 are restricted to the $0.4 - 10$ keV range, while the XIS1 spectrum is restricted to $0.4 - 7$ keV. In the rest frame of $z = 0.596$, $3'$ corresponds to 1.2 Mpc, and hence the $r < 3'$ circle includes the major fraction of the cluster emission.

Since the *Suzaku*/HXD is a non-imaging instrument, the spectral data are from the PIN field of $34' \times 34'$. We employ the energy range of $16 - 40$ keV. The HXD count rate from the source (the NXB and the CXB subtracted) is $(1.5 \pm 0.2) \times 10^{-2}\,\mathrm{counts\,s^{-1}}$

---

[9] `http://heasarc.gsfc.nasa.gov/docs/suzaku/analysis/abc/node10.html`

[10] `http://www.astro.isas.jaxa.jp/suzaku/doc/suzakumemo/suzakumemo-2008-06.pdf`

in $16-40\,\mathrm{keV}$, which corresponds to 7.3 % of the NXB, significantly larger than the systematic error in the NXB of 2.1% – 2.7 % (1σ) (Takahashi et al. 2010).

In addition to the X-ray background model (see Section 5.1.3), we apply a single-temperature (1T) thin thermal plasma model (**APEC**) as the spectrum of the Phoenix cluster. Then, we obtain the gas temperature, abundances, and redshift of the Phoenix cluster, as $16.7^{+0.9}_{-0.8}\,\mathrm{keV}$, 0.81 ± 0.09 solar, and $0.656^{+0.007}_{-0.005}$, respectively. This 1T model, however, shows the overall spectral shape with the concave residual, in excess at the low- and high-energy bands (see the top left panel of Figure 5.2). Furthermore, the best-fit redshift $z = 0.656$ is inconsistent with the optical observations (McDonald et al. 2012). We also find a line-like residual at 4.3 keV, which corresponds to $\sim 7\,\mathrm{keV}$ after correcting the redshift of 0.656. Thus, the residual may be either due to misidentification of the K-shell lines, and hence gave a larger plasma temperature as 16.7 keV, or due to an additional iron K-shell line.

The excess at the low-energy band may indicate the presence of another thin thermal plasma component with a low temperature. Two-temperature structure is already suggested in the 1T fitting of the spatially resolved *Chandra*/ACIS-I spectra (McDonald et al. 2012), which shows a low temperature in the inner region of $r \lesssim 100\,\mathrm{kpc}$ and a high temperature in the outer region. The excess at the high-energy band suggests the presence of a power-law component at the cluster center.

Chandra/ACIS-I Spectra from the Inner and Outer Regions

We show the *Chandra*/ACIS-I image to highlight the core and surrounding envelope of the Phoenix cluster in the bottom panel of Figure 5.1. Then, we extract the *Chandra*/ACIS-I spectra from the inner region of $r < 2''$ and the outer region of the $2'' < r < 3'$ annulus.

To examine the high temperature plasma in the outer region, we fit the spectrum with an **APEC** model fixing the redshift to $z = 0.596$. This model gives a nice fit with $\chi^2/\mathrm{dof} = 89/122$, as is shown in the top right panel of Figure 5.2. The best-fit temperature and abundance are constrained to be $10.9^{+1.8}_{-1.1}\,\mathrm{keV}$ and $0.33^{+0.18}_{-0.16}$ solar, respectively. They are roughly consistent with those obtained by McDonald et al. (2012).

We then examine the spectrum from the inner region of $r < 2''$. As is shown in the bottom left panel of Figure 5.2, this spectrum has a local minimum at about 2 keV, which indicates the presence of a soft component plus highly absorbed hard component. The former would be a low-temperature plasma, while the latter is likely an AGN. We therefore fit the spectrum with an **APEC** model (for low-temperature plasma) plus an absorbed power-law (absPL) continuum (for AGNs). This model is accepted with $\chi^2/\mathrm{dof} = 45/42$. We thus conclude that the X-rays from the inner region of the Phoenix cluster consist of a low-temperature component and an AGN power-law component. However, the physical parameters are only loosely constrained. The best-fit photon index and absorption column density for the power-law component are $\Gamma = 0.71^{+0.82}_{-0.66}$ and $N_{\rm H}= 1.9^{+2.4}_{-1.2} \times 10^{23}\,{\rm cm}^{-2}$, respectively, while the temperature and abundance for the low-temperature plasma are $4.89^{+6.07}_{-1.80}$ keV and $1.48^{+2.26}_{-1.13}$ solar, respectively. Table 5.1 summarizes the best-fit values of these fittings.

Suzaku/XIS Fit in the 3.5-5.0 keV

In the 1T model fit for the *Suzaku* spectra (Section 5.1.5), we also found a significant line-like residual at the energy of $\sim$4 keV. Converting it to the rest frame, the line energy corresponds to either the K-shell lines from neutral iron (Fe I), He-like Fe XXV or H-like Fe XXVI. We therefore zoom up the XIS spectrum in the $3.5 - 5.0$ keV range, and fit with a power-law continuum plus three Gaussian lines, in which the line energies are fixed to those of the K-shell transition from Fe I, Fe XXV, and Fe XXVI at the redshift $z = 0.596$. The spectrum and the best-fit results are shown in the bottom right panel of Figure 5.2. The Fe I line is detected at $3.5\,\sigma$ level. The equivalent width (EW) defined to the summed continuum of the thermal (i.e., the ICM emissions) and non-thermal (i.e., the central AGN emission) components is 23^{+10}_{-11} eV at the observer frame. Since a thin thermal plasma cannot emit the Fe I line, the most likely origin is an AGN in the BCG.

As we suggest in Section 5.1.5, we find that the 1T model fit of the wide-band spectra misidentified the Fe XXV line to that of Fe XXVI and Fe I to Fe XXV, and hence misled to a larger redshift of 0.656 and higher temperature of $kT \sim 17$ keV.

Simultaneous Fit for the *Suzaku*/XIS & HXD and *Chandra*/ACIS-I Spectra in the $r < 3'$ Region

We finally carry out the simultaneous fit for the X-ray spectra extracted in the same $r < 3'$ region from the *Suzaku*/XIS & HXD and *Chandra*/ACIS-I. The model includes all the components found in the previous subsections. Schematically the spectral model is given as **wabs** × (**APEC**$_{\rm low}$ + **APEC**$_{\rm high}$ + **zwabs** × **power-law** + **zgauss**). We fix the temperature and abundance of the **APEC**$_{\rm high}$ component as those obtained in the spectral fit with the *Chandra*/ACIS-I spectrum of the $2'' < r < 3'$ region. The line center energy was fixed at 6.40 keV (i.e., the Fe I line) at the rest frame. Since other parameters determined in the previous subsections are not well constrained, we treat them as free parameters. This model (2T+absPL+Fe I) nicely reproduces the over-all spectra with $\chi^2/{\rm dof} = 790/732$. The best-fit model and the data residual are shown in Figure 5.3, while the best-fit parameters are summarized in Table 5.1. All the best-fit parameters are consistent with those determined by the individual spectral fit given in Sections 5.1.5 and 5.1.5, but are more accurately determined. For comparisons with the previous results, we calculate the $10 - 50\,\mathrm{keV}$ and $14 - 150\,\mathrm{keV}$ band luminosities for the power-law component as $9.4^{+0.1}_{-0.2} \times 10^{45}\,\mathrm{erg\,s^{-1}}$ and $2.1^{+0.7}_{-0.8} \times 10^{46}\,\mathrm{erg\,s^{-1}}$, respectively. The EW of the Fe I line defined to the continuum emission of the central AGN (i.e., the absorbed power-law component) is 149^{+139}_{-58} eV at the rest frame.

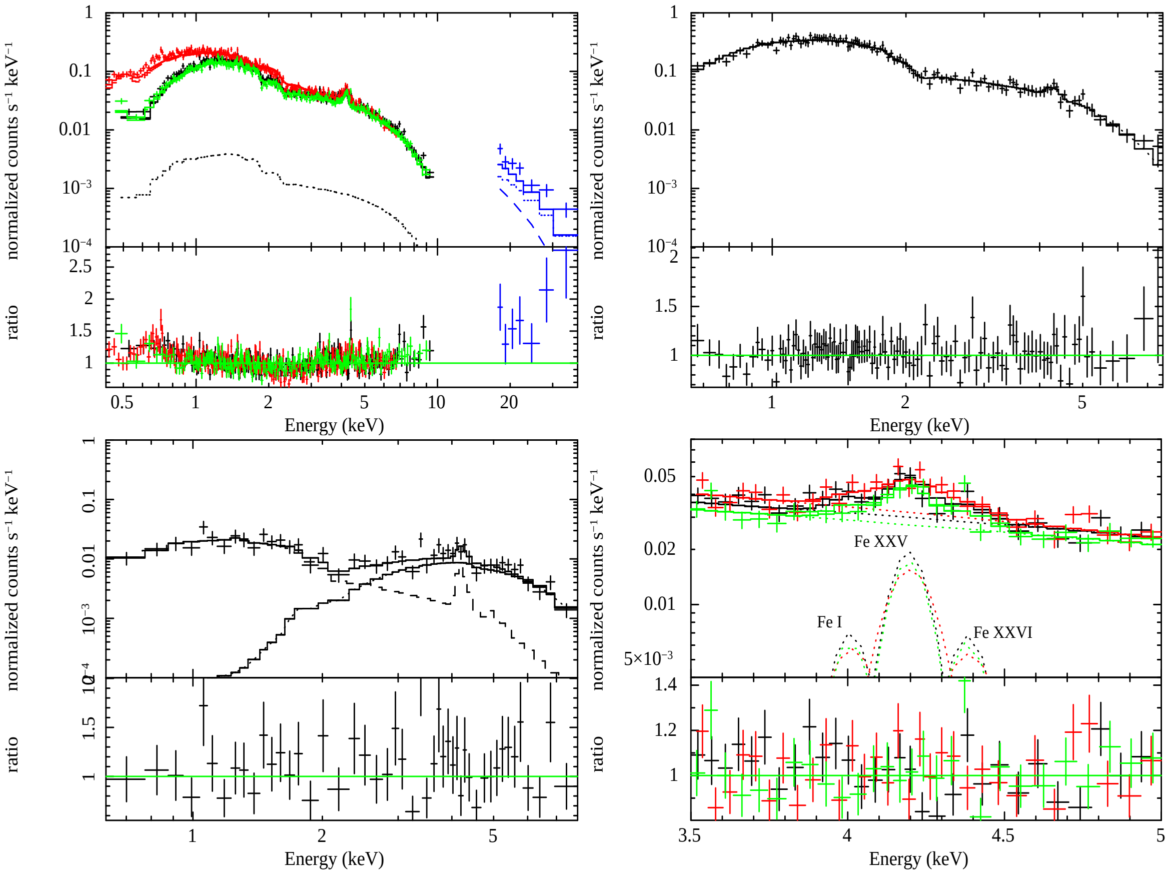

Figure 5.2: X-ray spectra of the Phoenix cluster. The ratios of the data to the model are plotted in the bottom panels. Top left panel: *Suzaku*/XIS0 (black), XIS1 (red), XIS3 (green), HXD (blue) spectra in the $r < 3'$ regions centered at the BCG fitted with a 1T model. The dashed lines show the best-fit model of the ICM for XIS0 and the HXD. The dotted lines represent the X-ray background model consisting of CXB, MWH, and LHB for XIS0 and HXD. Top right panel: *Chandra*/ACIS-I spectrum fitted with a 1T model. The region is $2'' < r < 3'$. Bottom left panel: *Chandra*/ACIS-I spectrum in the core region ($r < 2''$) fitted with a 1T model and an absorption power-law model. Bottom right panel: *Suzaku*/XIS spectra in 3.5–5.0 keV fitted with a power-law continuum and three Gaussian lines.

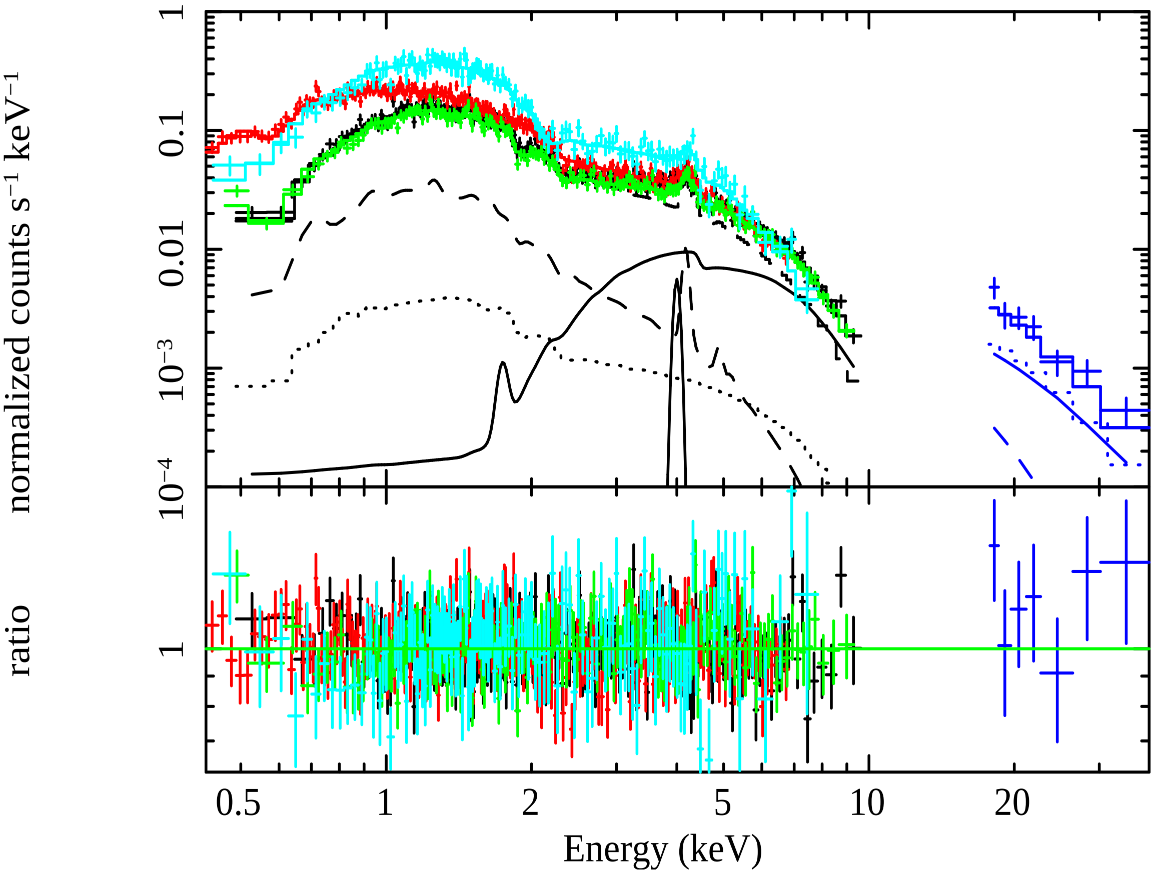

Figure 5.3: *Suzaku*/XIS & HXD and *Chandra*/ACIS-I spectra simultaneously fitted with a 2T+absPL+Fe I model expressing the cluster thermal emission and the central AGN emission. The same colors and lines are used as those in Figure 5.2 for the *Suzaku*/XIS0, XIS1. XIS3, and HXD data. The *Chandra*/ACIS-I data are plotted in cyan. The solid lines show an absorbed power-law component and a neutral iron K-line (Fe I) for XIS0 and HXD.

Table 5.1: Best-fit Results of the Spectral Fitting with the *Chandra*/ACIS-I in $0.6 - 8\,\mathrm{keV}$ and the *Suzaku*/XIS & HXD and the *Chandra*/ACIS-I in $0.4 - 40\,\mathrm{keV}$

Instruments	Region	$\mathrm{APEC_{low}}$		$\mathrm{APEC_{high}}$		zwabs×power-law+zgauss		χ^2/d.o.f.
Chandra/ACIS-I	$r < 2''$	kT (keV)	$4.89^{+6.07}_{-1.80}$			$N_{\mathrm{H}}\,(\times 10^{23}\,\mathrm{cm^{-2}})$	$1.9^{+2.4}_{-1.2}$	45/42
		$Z_{\odot}$ (solar)	$1.48^{+2.26}_{-1.13}$			Photon index	$0.71^{+0.82}_{-0.66}$	
		Redshift	0.596 (fix)			EW of Fe I (eV)	134^{+207}_{-134}	
Chandra/ACIS-I	$2'' < r < 3'$			kT (keV)	$10.9^{+1.8}_{-1.1}$			89/122
				$Z_{\odot}$ (solar)	$0.33^{+0.18}_{-0.16}$			
				Redshift	0.596 (fix)			
Suzaku/XIS & HXD	$r < 3'$	kT (keV)	$2.95^{+0.53}_{-0.48}$	kT [keV]	10.9 (fix)	$N_{\mathrm{H}}\,(\times 10^{23}\,\mathrm{cm^{-2}})$	$3.2^{+0.9}_{-0.8}$	790/732
and *Chandra*/ACIS-I		$Z_{\odot}$ (solar)	$0.76^{+0.63}_{-0.31}$	$Z_{\odot}$ (solar)	0.33 (fix)	Photon index	$1.54^{+0.27}_{-0.24}$	
		Redshift	$0.599^{+0.004}_{-0.006}$			EW of Fe I (eV)	149^{+139}_{-58}	

5.1.6 Discussion on the Phoenix Cluster

With the simultaneous fit of the *Suzaku*/XIS & HXD and the *Chandra*/ACIS-I data, we have discovered that the X-ray spectrum of the Phoenix cluster can be approximated by three components: two thin thermal plasma components with different temperatures and spatial distributions, and a power-law component in the cluster center. We also determine the redshift of the Phoenix cluster as $z = 0.599^{+0.004}_{-0.006}$ by the X-ray spectra alone. This value is consistent with the mean value ($z = 0.596 \pm 0.002$) of 26 member galaxies (McDonald et al. 2012). In the following subsections, we separately discuss the thermal emission from the ICM and the power-law component of the AGN. We then discuss possible interactions between these components through the viewpoint of the feeding and feedback processes in the cluster, BCG, and SMBH. We refer all the physical parameters at the rest frame of $z = 0.596$ unless otherwise specified.

Thermal Emission from the ICM

Although the ICM may consist of multi-temperature plasmas in pressure equilibrium, it can be nicely approximated by two temperature plasma: the low-temperature plasma of $2.95^{+0.53}_{-0.48}$ keV and the high temperature plasma of $10.9^{+1.8}_{-1.1}$ keV. The X-ray luminosity in the $2-10$ keV band within 1.2 Mpc is $L_{\rm X,low} = 1.0^{+0.4}_{-0.5} \times 10^{45}\,{\rm erg\,s^{-1}}$ and $L_{\rm X,high} = 7.0^{+0.7}_{-0.6} \times 10^{45}\,{\rm erg\,s^{-1}}$ for the low-temperature and high-temperature plasmas, respectively. The high-temperature plasma is prevailing in the whole cluster with the abundances of $0.33^{+0.18}_{-0.16}$ solar, typical value for clusters. The low-temperature plasma has a higher abundance of $0.76^{+0.63}_{-0.31}$ solar and is confined in the core of the cluster. Possibly in the cluster core, a large amount of metals is supplied from supernovae in the BCG. These features are commonly observed in nearby cool-core clusters with cD galaxies (i.e., BCG) at their centers (e.g., Matsushita 2011).

Following White et al. (1997), which is the same method as McDonald et al. (2013a), we estimate the cooling rate to be $2290^{+1260}_{-770}\ M_{\odot}\,{\rm yr^{-1}}$. This value is consistent with that of McDonald et al. (2013a).

Radial Profiles of Temperature and Abundance of the ICM

We can obtain the radial profiles of temperature and abundance of the ICM by using the data obtained with *Chandra*/ACIS-I and *XMM-Newton*/EPIC more accurately than those with *Suzaku*. The top panel of Figure 5.4 shows the radial profile of temperature of the ICM, while the bottom panel of Figure 5.4 shows that of abundance of the ICM. The *Chandra* results are consistent with those of *XMM-Newton*. The ICM temperature increases from the central region ($\sim$ 6 keV) toward the outer region ($\sim$ 16 keV) , and the abundance distribution of the ICM is centrally peaked in the Phoenix cluster. These distributions are qualitatively typical for those observed in nearby cool-core clusters (e.g., Matsushita 2011).

What Is the Origin of the Fe I Line?

As mentioned in Section 5.1.5, we discover the Fe I line at the rest frame in the redshift of $z = 0.596$. We discuss whether the Fe I line is due to the central AGN or to other possibilities.

One possibility is due to gain error of the *Suzaku*/XIS. The gain error of the *Suzaku*/XIS is $\sim 0.1\,\%$ at 6 keV (6 eV for the Fe I line), which is estimated using several targets and Mn I Kα lines from the calibration source of ^{55}Fe (e.g., Koyama et al. 2007a; Ota et al. 2007; Ozawa et al. 2009; Tamura et al. 2011). The energy difference between Fe I and Fe XXV at the observer's frame is $\sim$ 200 eV, which is significantly larger than the gain error of the *Suzaku*/XIS.

A second possibility is velocity-broadened (e.g., bulk motion and/or turbulence of the ICM) Fe XXV line (6.7 keV at the rest frame), which may partly mimic the Fe I line. We fitted the X-ray spectra (the lower right panel of Figure 5.2) with a broadened line of the Fe XXV line. Then, we obtain the line width of Fe XXV to be $\sim$ 188 eV at the observer's frame, which corresponds to a velocity of $\sim 13,000\,\mathrm{km\,s^{-1}}$ at the rest frame (Ota 2012). This velocity is too huge for the realistic motion of the ICM. Furthermore, McDonald et al. (2012) reported that the X-ray surface brightness of the Phoenix cluster shows a relaxed morphology of the ICM, suggesting that bulk motion is not prominent.

A third possibility is a contamination of other point sources than the AGN in the BCG within $3'$ radius. We evaluate such an amount by examining the $2 - 10$ keV intensity of the sources based on using the *Chandra* 11.9 ks observation. The emission within $2''$ from the central AGN contains a total of 501 counts in the $2 - 10$ keV band. Based on our fitting result shown in the lower left panel of Figure 5.2, we estimate that 361 counts are owing to the central AGN and the rest primarily consists of the ICM thermal emission. On the other hand, there are six other point sources within $3'$ radius around the central AGN. The most intense one has 8 counts in the $2 - 10$ keV band, and the sum of the counts from the six point sources is only 15 counts, which is $4\,\%$ of that of the central AGN. Supposing that most of the six point sources are type I AGNs with typical Fe I EW of $\sim$ 100 eV (see, e.g., the black triangles in the right panel of Figure 5.6), the possible contribution for the Fe I EW of the central AGN is only 4 eV.

As discussed above, we can reject three possibilities for the origin of the Fe I line. We

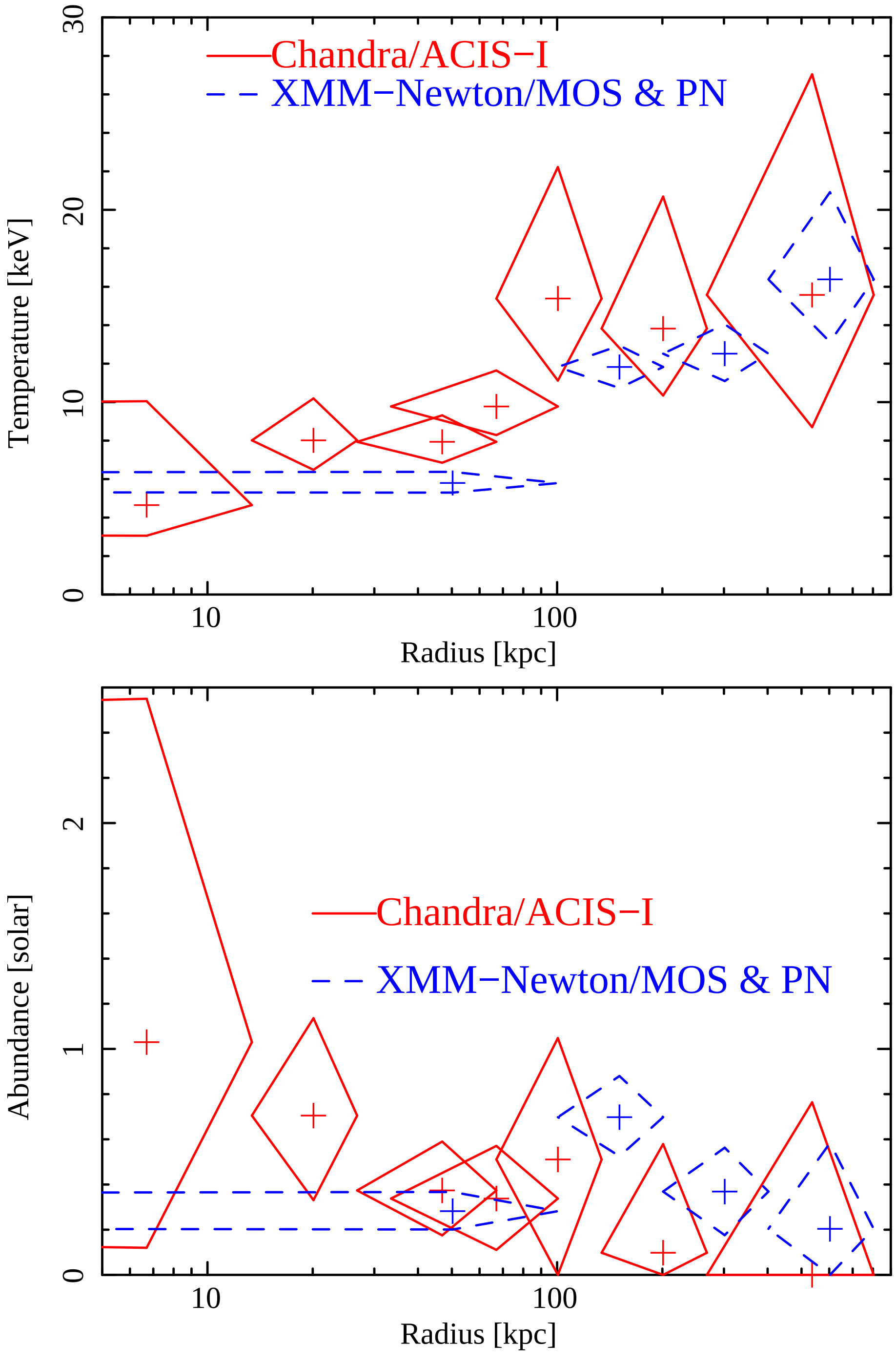

Figure 5.4: Radial profiles of temperature and abundance of the ICM obtained with *Chandra*/ACIS-I and *XMM-Newton*/MOS & PN. Top panel: Radial profile of temperature of the ICM. The red diamonds show the ICM temperatures obtained with *Chandra*. The blue dashed diamonds are that obtained with *XMM-Newton*. Bottom panel: the same as the top panel but for the abundance of the ICM.

hence regard the most natural idea as that the Fe I line comes from the central AGN in the BCG of the Phoenix cluster.

Properties of the Type 2 QSO at the Center

We have discovered that the power-law component in the cluster center has a Fe I K-shell line with EW of 149^{+139}_{-58} eV. The power-law photon index, Γ, is determined for the first time as $1.54^{+0.27}_{-0.24}$. The absorption column density of $3.2^{+0.9}_{-0.8} \times 10^{23}\,\mathrm{cm}^{-2}$ is consistent with, but is more accurate than that in previous work (McDonald et al. 2012). The absorption-corrected luminosity of $(4.7 \pm 0.7) \times 10^{45}\,\mathrm{erg\,s^{-1}}$ $(2-10\,\mathrm{keV})$ is slightly higher than that in McDonald et al. (2012), but their consistency cannot be examined because they did not mention its error.

A large N_{H}, a photon index in the range of $1.5-2.0$, and a strong Fe I line are common features in type 2 AGNs (Awaki et al. 1991a). Together with an extremely high X-ray luminosity, the central AGN of the Phoenix cluster can be regarded as a type 2 QSO. This is the second case of a type 2 QSO in a cluster after IRAS 09104+4109 (Kleinmann et al. 1988; O'Sullivan et al. 2012).

The X-ray luminosity of $2.1^{+0.7}_{-0.8} \times 10^{46}\,\mathrm{erg\,s^{-1}}$ $(14-150\,\mathrm{keV})$ is similar to the *Swift*/BAT result of $(1.4 \pm 0.9) \times 10^{46}\,\mathrm{erg\,s^{-1}}$ within errors (Cusumano et al. 2010b). As is seen in Figure 3, the power-law component (AGN) is dominated over the ICM plasma in the $14-150\,\mathrm{keV}$ band. Therefore the luminosity given by Cusumano et al. (2010b) is surely due to the type 2 QSO, and we see no large time variability in the type 2 QSO during the *Swift*/BAT (2004 - 2010) and the *Suzaku* observation (2010). Note that the luminosity estimated from the *Chandra*/ACIS-I spectrum by us is $L_{\mathrm{X}} = (4.0 \pm 0.5) \times 10^{45}\,\mathrm{erg\,s^{-1}}$ in $2-10\,\mathrm{keV}$ with the N_{H} and Γ fixed to the best-fit parameters of Table 5.1, which is also consistent with the result of a simultaneous fit. We also confirm these results with the *XMM-Newton* observations.

Although the X-ray luminosity is exceptionally large as $10^{45}\,\mathrm{erg\,s^{-1}}$ $(2-10\,\mathrm{keV})$, the N_{H} and EW are on the general trend of the correlation shown in Fukazawa et al. (2011), who compiled the *Suzaku* results of 88 AGNs. The X-ray spectra of the type 1 and type 2 AGNs are interpreted in the unified scheme of AGNs. The differences in the observational properties of type 1 and type 2 AGNs are primarily due to observers' line of sight: face-on (type 1) or edge-on (type 2) to the molecular torus surrounding the nucleus. In this scheme, the X-ray spectra of type 2 AGNs consist of two components; one is penetrating through the torus, and the other is scattered at the surface of the torus. The former is called a direct component, and the latter is a reflection component. The Fe I line is mainly associated with the reflection component. Since our spectral fit in Section 5.1.5 implicitly assumed that the continuum flux of the AGN is dominated by the direct component only, we try the two-component structure of the type 2 QSO with the **pexmon** model (Nandra et al. 2007) in XSPEC. The **pexmon** model represents an exponentially cut-off power-law spectrum reflected from neutral material. The direct, reflection components, and the fluorescent lines of Fe-K and Ni-K are included in a self-consistent manner. We assume the inclination angle, the cut-off energy of the power-law component, and the Fe abundance to be $\theta_{\rm i} = 60^\circ$, 300 keV, and 1 solar, respectively. Then, the X-ray spectra of the AGN component are reproduced with the best-fit value for the reflection fraction (R) of $0.77^{+0.48}_{-0.38}$, where R is defined as the ratio of the solid angle of the reflector Ω to 2π steradian, i.e., $R = \Omega/2\pi$. This R value and the initial assumption of viewing angle of $\theta_{\rm i} = 60^\circ$ are consistent with the type 2 AGN picture of the torus edge-on geometry. Figure 5.5 shows the fitting results of X-ray spectra simultaneously fitted with the cluster thermal emission, absorbed power-law component (i.e., direct component), and a reflection component from the torus.

Ricci et al. (2011) derived R values for 165 Seyfert galaxies using the hard X-ray spectra with *INTEGRAL* (Winkler et al. 2003) /IBIS (Ubertini et al. 2003) & ISGRI (Lebrun et al. 2003). They showed that Seyfert galaxies with $10^{23}\,{\rm cm}^{-2} < N_{\rm H} < 10^{24}\,{\rm cm}^{-2}$ (Compton thin AGNs), have R of $2.2^{+4.5}_{-1.1}$ on average, which is consistent with the type 2 QSO in the Phoenix cluster within large uncertainties. Ikeda et al. (2009) performed Monte Carlo simulations of the X-ray spectra in various torus geometries. The absorption column density and the EW of the Fe I line for the type 2 QSO (149^{+139}_{-58} eV) in the Phoenix cluster are consistent with those from the simulation for the torus half-opening angle of 30° (see the left panel of Figure 13 in Ikeda et al. 2009). Then, the expected EW of the Fe I line is ~ 200 eV.

The top panel of Figure 5.6 shows a relation of the EW of the Fe I line and the absorption column density ($N_{\rm H}$) for our results of the Phoenix cluster and 86 Seyfert galaxies data (Fukazawa et al. 2011, but we excluded the AGN data of which no significant $N_{\rm H}$, X-ray luminosity, and EW of Fe I were determined). The type 2 QSO in the Phoenix cluster is on the same trend of these type 1 and type 2 AGNs. In general, a higher X-ray luminosity AGN exhibits a smaller EW of the Fe I line, known as the X-ray Baldwin effect (Iwasawa & Taniguchi 1993). The bottom panel of Figure 5.6 shows the X-ray Baldwin effect by Fukazawa et al. (2011) (the data selection is the same as the left panel of Figure 5.6). The type 2 QSO in the Phoenix cluster has exceptionally larger flux than any other high luminosity AGNs. Extrapolation of these data points by a linear function to the higher luminosity of $\sim 10^{46}\,{\rm erg\,s^{-1}}$, gives an EW no larger than a few 10 eV, far smaller than that of the type 2 QSO in the Phoenix cluster of ${\rm EW} = 149^{+139}_{-58}$ eV. These

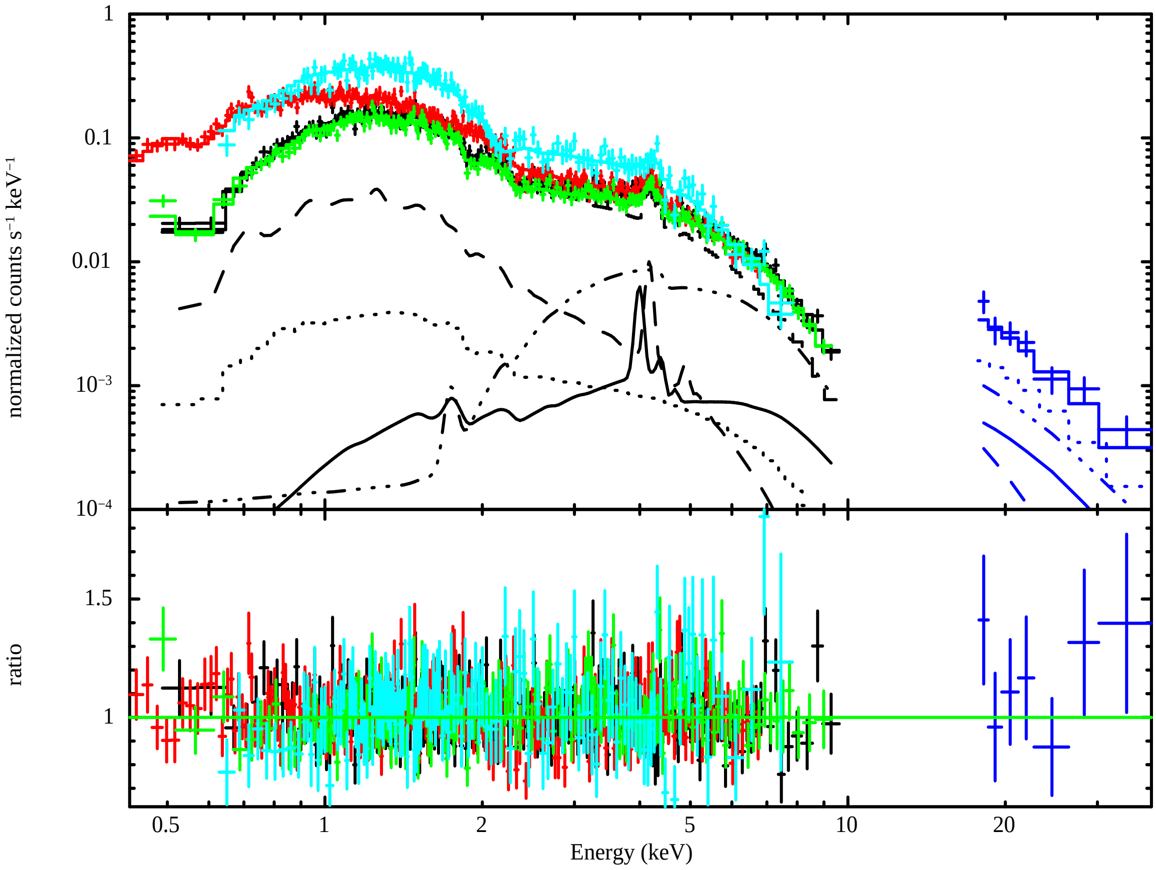

Figure 5.5: *Suzaku*/XIS & HXD and *Chandra*/ACIS-I spectra simultaneously fitted with the cluster thermal emission, absorbed power-law component (i.e., direct component), and a reflection component from the torus. The same colors and lines are used as those in Figure 5.3 for the *Suzaku*/XIS0, XIS1. XIS3, HXD, and *Chandra*/ACIS-I data. The solid lines show a reflection component from the torus. The dashed and dotted lines show an absorbed power-law component.

indicate that the type 2 QSO in this cluster has a torus of larger covering factor than those of the general trend of bright AGNs (see Figure 5 of Fukazawa et al. 2011).

Type 2 QSO - ICM Interaction

In Section 5.1.6, we show that the AGN in the BCG of the Phoenix cluster is a type 2 QSO with an unobscured X-ray luminosity of $(4.7 \pm 0.7) \times 10^{45}\,\mathrm{erg\,s^{-1}}$ $(2-10\,\mathrm{keV})$. The EW of the Fe I line of $\sim 150\,\mathrm{eV}$ is exceptionally large for objects with such high luminosity. Furthermore, since the type 2 fraction is smaller for higher luminosity (e.g., Ueda et al. 2003; Hasinger 2008), type 2 QSO in the Phoenix cluster is a rare case. This may be related to other extraordinary properties of this object, i.e., a very active SMBH in the BCG, a huge cooling rate of the ICM, and a large SFR in the BCG.

Assuming the bolometric correction factor of 130 (Marconi et al. 2004), the bolometric luminosity of this type 2 QSO is $L_{\mathrm{bol,QSO}} = (6.2 \pm 0.9) \times 10^{47}\,\mathrm{erg\,s^{-1}}$, which corresponds to $\sim 27\,\%$ of the Eddington limit. Adopting the accretion efficiency of $\eta = 0.1$, the accretion rate is estimated to be $\sim 110\,M_{\odot}\,\mathrm{yr^{-1}}$. This is $\sim 5\,\%$ of the ICM cooling rate. Another $35\,\%$ of the cooled gas may be consumed by the violent star formation ($\sim 798\,M_{\odot}\,\mathrm{yr^{-1}}$, McDonald et al. 2013a) in the BCG. We denote these two rates as ϵ_{acc} and ϵ_{SFR}. The sum of ϵ_{acc} and ϵ_{SFR} ($40\,\%$) is larger than typical cool-core clusters.

The mass of the torus can be estimated using the observed column density of $3.2 \times 10^{23}\,\mathrm{cm^{-2}}$ and assuming a spherical ring with the inner radius of $0.9\,\mathrm{pc}$. The inner radius of the torus is given by the $0.03 L_{43}^{0.5}\,\mathrm{pc}$ relation (Suganuma et al. 2006, where L_{43} is X-ray luminosity in unit of $10^{43}\,\mathrm{erg\,s^{-1}}$). The estimated torus mass is however largely dependent on the assumed outer radius, such as $3.0 \times 10^{4}\,M_{\odot}$, $1.2 \times 10^{6}\,M_{\odot}$, $1.1 \times 10^{8}\,M_{\odot}$, and $1.1 \times 10^{10}\,M_{\odot}$ for the outer radius of $1\,\mathrm{pc}$, $10\,\mathrm{pc}$, $100\,\mathrm{pc}$, and $1000\,\mathrm{pc}$, respectively. If the accretion rate of $110\,M_{\odot}\,\mathrm{yr^{-1}}$ has been constantly supplied by the torus, the torus mass is exhausted within 3×10^{2} to $1 \times 10^{8}\,\mathrm{yr}$, shorter than the evolution time of a SMBH, BCG, and cluster. Furthermore, if the outer radius is smaller than $1000\,\mathrm{pc}$, the lifetime of this torus is shorter than the nominal QSO lifetime of $10-20\,\mathrm{Myr}$ reported by Hopkins et al. (2005). Possibly, some fraction of the cooling gas would be supplied continuously to the torus. Taniguchi et al. (1997) applied this idea to IRAS 09104+4109 as a dust-enshrouded type 2 QSO in the center of a massive cooling-flow cluster (e.g., Fabian & Crawford 1995; Crawford & Vanderriest 1996; O'Sullivan et al. 2012) and estimated the mass of the torus to be $\sim 1 \times 10^{7}\ M_{\odot}$ for a compact torus less than $10\,\mathrm{pc}$, or $\sim 1 \times 10^{9}$ $M_{\odot}$ for an extended torus of $\sim 100\,\mathrm{pc}$. Fabian & Crawford (1990) shows that a QSO in the cluster center can be fueled in a self-sustaining way through Compton cooling of the surrounding ICM. In the type 2 QSO of the Phoenix cluster, the cooled gas would be also

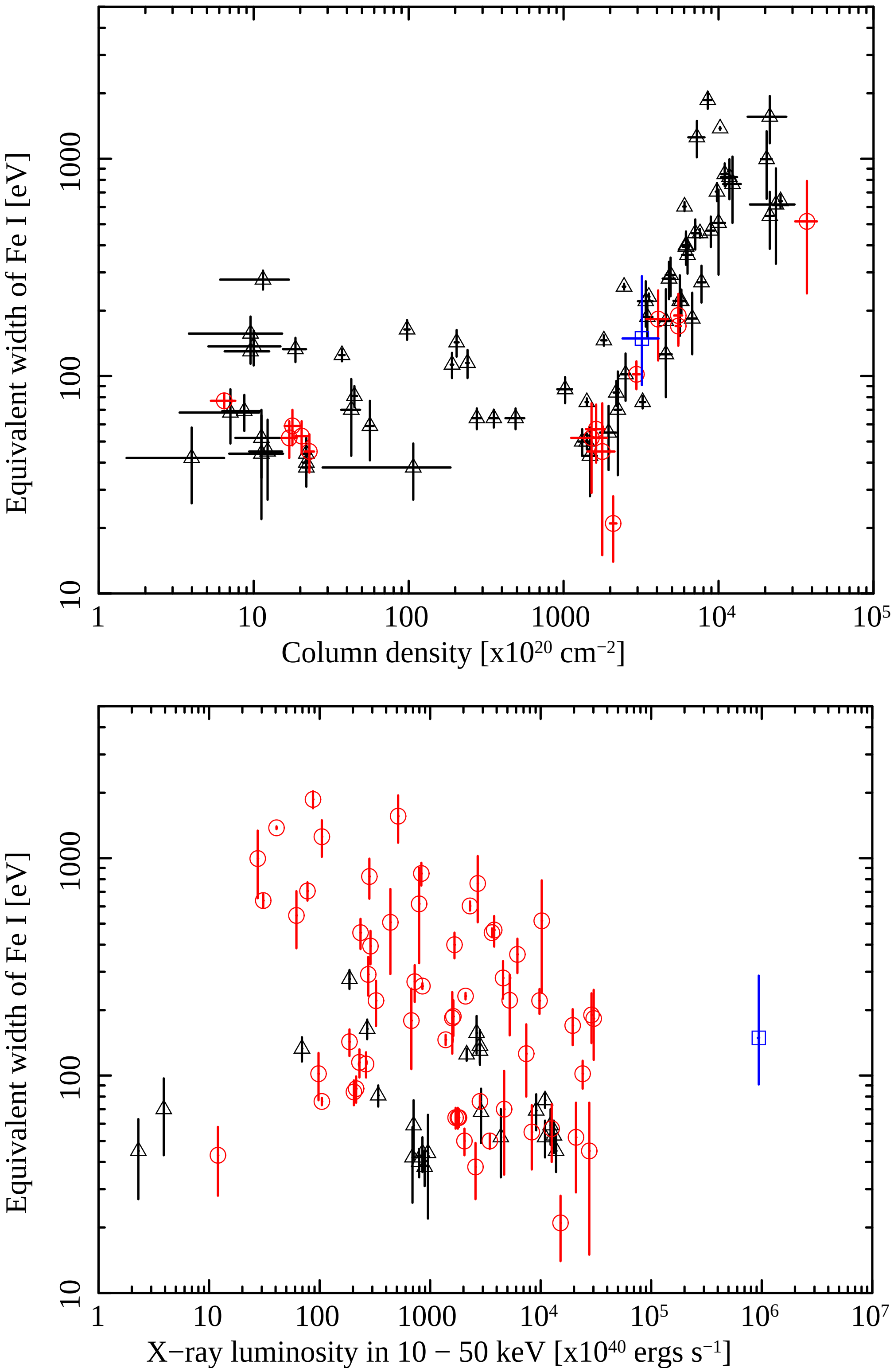

Figure 5.6: Top panel: relation of the EW of the Fe I line and absorption column density (N_{H}). The black triangles are AGNs with X-ray luminosity in $10-50\,\mathrm{keV}$ ($L_{\mathrm{X},10-50}$) of $L_{\mathrm{X},10-50} < 10^{44}\,\mathrm{erg\,s^{-1}}$ (Fukazawa et al. 2011, but we excluded the AGN data of which no significant N_{H}, X-ray luminosity, and EW of Fe I were determined), while the red circles are $L_{\mathrm{X},10-50} > 10^{44}\,\mathrm{erg\,s^{-1}}$. The blue square shows the type 2 QSO in the Phoenix cluster (this work). Bottom panel: relation of the EW of the Fe I line and the X-ray luminosity in $10-50\,\mathrm{keV}$. The black triangles represent the AGNs with $N_{\mathrm{H}} < 10^{22}\,\mathrm{cm^{-2}}$, the red circles are $N_{\mathrm{H}} > 10^{22}\,\mathrm{cm^{-2}}$, and the blue square is the type 2 QSO in the Phoenix cluster.

supplied continuously to the torus and would finally accrete on the SMBH.

In idealized cool-core clusters, a large cooling rate should be converted to the cooling flow, which finally should appear as significant cold gas near the cluster center. However no clear evidence for the fate of cold gas has been observed (e.g., Makishima et al. 2001; Tamura et al. 2001; Peterson et al. 2001). This is called the "cooling flow problem" (e.g., Fabian 1994). Some unknown mechanisms to suppress the cooling flow should be working. The most plausible explanation for the suppression of the cooling flow is heating by the AGN activity (called the "AGN feedback"; e.g., Fabian 1994; McNamara & Nulsen 2007). Its alternative is conduction of heat from the outer part of the ICM (e.g., Fabian 2003).

As we noted, the masses responsible for the violent star formation and accretion on the SMBH are 40 % of the cooling rate. The remaining 60 % of the gas may be cooled and deposited in the ICM within 100 kpc to the BCG scale. The point here is that the fraction of 40 % is significantly higher than those of other nominal cool-core clusters ($\sim 10\,\%$ or less, Blanton et al. 2003; McDonald et al. 2011, 2012). A question is why the cooling flow suppression, i.e., the AGN feedback, in the Phoenix cluster is less effective than the other cool-core clusters. As one possibility, McDonald et al. (2012) proposed that the Phoenix cluster is in a very rare epoch in the SMBH, BCG, and cluster evolution, where the SMBH is powered by the cooling flow, but has not yet fully coupled with the ICM. Hence the quenching fraction of the total cooling is smaller than those in typical nearby cool-core clusters. If the AGN feedback is mainly due to jet interaction with the ICM (Perucho et al. 2011), the so-called kinetic mode (Fabian 2012), the time from the latest onset of AGN activity must be shorter than the light-crossing time of the cluster core, i.e., $\sim 0.3\,\mathrm{Myr}$. This is very short compared with the typical timescale of AGN activity, and the Phoenix cluster must be in a very rare epoch.

Alternatively, the AGN feedback to the ICM can take place through radiation from the QSO, called the radiative-mode or quasar-mode (Fabian 2012). As mentioned in Fabian (2012), this mode must be very important in the distant Universe but hard to be observed in the nearby Universe. The Phoenix cluster is thus an exceptional and possibly very important case. On this point, we suggest that inefficient AGN feedback in the Phoenix cluster is related to the larger EW of the Fe I line than that predicted from the general trend of the X-ray Baldwin effect. Possible explanation of the X-ray Baldwin effect is that strong X-rays from the central AGN would reduce the mass of the torus by the X-ray evaporation (Pier & Voit 1995; Kallman et al. 2004; Fukazawa et al. 2011), and hence reduce the EW of the Fe I line. As mentioned above, we suggest that some fractions of the massive cooling flow are supplied to the torus to compensate such an evaporation. Then, at least, a significant part of the torus is maintained (i.e., not evaporated all neutral materials yet) against an intense irradiation of bright SMBH. This torus may shield the radiation from the SMBH to suppress the heating of the ICM further. Although we have little observational evidence of radiative-mode AGN feedback from a central AGN to ICM, the shielding effect by the torus might be an important mechanism in SMBH and BCG evolution.

5.1.7 Summary of Our X-ray Study of the Phoenix Cluster and the Type 2 QSO in its BCG

We have studied the X-ray spectra of the Phoenix cluster observed with the *Suzaku*/XIS & HXD, the *Chandra*/ACIS-I, and the *XMM-Newton*/EPIC and have separately determined the ICM components and the central AGN component. We confirmed that the ICM can be approximated by low-temperature ($kT = 2.95^{+0.53}_{-0.48}\,\mathrm{keV}$) and high-temperature ($kT = 10.9^{+1.8}_{-1.1}\,\mathrm{keV}$) components. The low-temperature component is concentrated at the cluster core and has a high abundance of $0.76^{+0.63}_{-0.31}$ solar, while the high-temperature component distributes over the cluster and has a abundance of $0.33^{+0.18}_{-0.16}$ solar. These properties of the ICM are similar to those observed in nearby cool-core clusters. The major difference is its huge cooling rate of $\dot{M}_{\mathrm{total}} = 2290^{+1260}_{-770}\,M_{\odot}\,\mathrm{yr}^{-1}$.

The X-ray spectrum of the central AGN in the Phoenix cluster is characterized with an strongly absorbed ($N_{\mathrm{H}} = 3.2^{+0.9}_{-0.8}\times10^{23}\,\mathrm{cm}^{-2}$) power-law continuum plus the K-shell line from a neutral iron (Fe I). The EW of the Fe I line (149^{+139}_{-58} eV) and the absorption column density are typical for Compton-thin type 2 AGNs. However the EW is significantly larger than that of the general trend of the X-ray Baldwin effect, extrapolated to a luminosity as high as that of the type 2 QSO in the Phoenix cluster.

The high X-ray luminosity and large EW of the Fe I line motivated us to examine a possibility that luminous AGNs in BCGs may have unique properties reflecting their environment. We particularly focus on the Fe I line and the absorption column density that provide information of surrounding matter around SMBHs. We will discuss this point in Chapter 7 after presenting the other two AGNs in BCGs and also the other type 2 QSOs in field (not in clusters).

5.2 Type 1 QSO in the Central Galaxy of H 1821+643

In this section, we study the X-ray properties of the luminous AGN in the BCG of H 1821+643, which is the second source selected in Chapter 4.3.2 by referring both the *Planck* SZ cluster catalogue with the *Swift*/BAT 70-Month catalogue. We analyze the X-ray spectra of the AGN, which should be classified as a type 1 QSO, obtained with *Suzaku*/XIS & HXD. Surrounding matter around the SMBH in this type 1 QSO suggested from the X-ray observation will be discussed in Chapter 7, together with those in other QSOs studied in this work.

5.2.1 Previous Observations of H 1821+643

H 1821+643 (or E 1821+643) was first discovered with *Einstein* X-ray observatory and later identified as a radio-quiet type 1 QSO at the redshift $z = 0.297$ (Pravdo & Marshall 1984). Following multi-wavelength (far-IR, optical, UV, and X-ray) observations of this source (Neugebauer et al. 1986; Kolman et al. 1991; Kii et al. 1991) revealed that this source is a highly luminous QSOs. Hutchings & Neff (1991) suggested that the host galaxy of H 1821+643 is a giant elliptical galaxy, and Schneider et al. (1992) found that the host galaxy is the central galaxy in a rich clusters of galaxies, and Lacy et al. (1992) reproted the cluster has an Abell richness class greater than 2. A radio luminosity of H 1821+643 at 5 GHz is $10^{23.9}\,\mathrm{W\,Hz^{-1}\,sr^{-1}}$ and that at 151 MHz is $10^{25.3}\,\mathrm{W\,Hz^{-1}\,sr^{-1}}$ (Blundell & Rawlings 2001), leading to the classification of this source as a radio-quiet quasar. However, H 1821+643 is also classified as a FR I radio galaxy with a jet like structure of 300 kpc (Blundell & Rawlings 2001). The mass of its SMBH is estimated to be $\sim 3 \times 10^9\,M_\odot$ (Kolman et al. 1993; McGill et al. 2008).

Kii et al. (1991) observed this source with the Large Area Counters (LAC) (Turner et al. 1989) onboard *Ginga* satellite (Makino 1987) and first detected an iron K-line, whose center energy was 6.6 ± 0.3 keV and the EW was 275 ± 105 eV at rest frame. The energy resolution of the LAC was, however, not high enough to identify the line was Fe I or Fe XXV. With *ASCA* (Tanaka et al. 1994), Yamashita et al. (1997) observed this source and reported that the center energy of the iron K-line was 6.58 ± 0.05 keV and its EW was consistent with that reported by Kii et al. (1991). Since the line center energy indicates the line is originated in moderately ionized matter, and they found the line was marginally broad with an upper limit of 180 eV in Gaussian width, they concluded that the origin of iron K-line was the QSO.

However, Hall et al. (1997) found the evidence of extended X-ray emission around H 1821+643 with *ROSAT*, indicating the presence of thermal emission from ICM. Fang et al. (2002) observed this source with the *Chandra*/HETG and detected two separate iron K-lines, one at 6.44 ± 0.04 keV and the other at $6.94^{+0.05}_{-0.07}$ keV. The EW of the lines were 113^{+42}_{-36} eV and 49 ± 31 eV at the rest frame, respectively. Fang et al. (2002) also measured the X-ray spectrum of extended emission from the ICM; the ICM has a temperature of $kT = 10.8^{+1.0}_{-0.9}$ keV and an abundance of $Z_{\odot} = 0.35 \pm 0.08$ solar) in a circular region of $3'' < r < 100''$. The X-ray luminosity of the ICM in $2 - 10$ keV within this region is $L_{\mathrm{X},2-10} = 2.54 \times 10^{45}\,\mathrm{erg\,s^{-1}}$. Jiménez-Bailón et al. (2007) observed this source with the *XMM-Newton*/EPIC and found similar iron-K line features to those reported by Fang et al. (2002). They provided the temperature of the ICM of $kT = 8^{+13}_{-7}$ keV with the Raymond-Smith model (Raymond & Smith 1977) by fixing the metal abundance at 0.3 solar. The X-ray luminosity of the thermal emission of the ICM within $r < 20''$ region was $L_{\mathrm{X},2-10} = 1.1^{+1.2}_{-0.2} \times 10^{45}\,\mathrm{erg\,s^{-1}}$, which corresponds to 30 ± 6 % of the total luminosity in this band. The X-ray luminosity of the QSO was $L_{\mathrm{X},2-10} = 3.44^{+0.13}_{-0.09} \times 10^{45}\,\mathrm{erg\,s^{-1}}$ (Jiménez-Bailón et al. 2007).

The origin of two line features with the center energies of ~ 6.4 keV and ~ 6.9 keV is still not clear. Fang et al. (2002) attributed ~ 6.4 keV line to the Fe I line from neutral iron in an accretion disk or in a torus, while the other to highly ionized iron K-line (i.e., Fe XXV and Fe XXVI complex) from optically thin atmosphere atop the accretion disc. On the other hand, Yaqoob & Serlemitsos (2005) reanalyzed the data obtained with the *Chandra*/HETG to conclude that the feature could be explained with a broad iron emission line with an absorption line superimposed on the red wing of the broad line. The absorption line was attributed to the resonance absorption of highly ionized iron, either in inflowing matter or in an outflow that is strongly gravitationally redshifted and located very closed to the accretion disc (Yaqoob & Serlemitsos 2005). However, Jiménez-Bailón et al. (2007) found an absorption line at $6.57^{+0.05}_{-0.07}$ keV, which was not consistent with that obtained by Yaqoob & Serlemitsos (2005). The contribution from the ICM thermal emission to the ~ 6.9 keV line was considered to be negligible by Fang et al. (2002), while Jiménez-Bailón et al. (2007) suggested that the measured flux of that line with *XMM-Newton* could be fully explained with the thermal emission from the ICM.

Russell et al. (2010) investigated the ICM in this source more in detail with the *Chandra*/ACIS-S. According them, the ICM temperature decreases from 9.0 ± 0.6 keV in a $23.6'' < r < 29.5''$ region down to 1.3 ± 0.2 keV in a $3.4'' < r < 4.2''$ region. The metal abundance of the ICM is uniform over the entire region of the clusters with ~ 0.3 solar, where r_{200} corresponds to $2.5^{+1.3}_{-0.7}$ Mpc. A radiative cooling time of the central region is 1.0 ± 0.1 Gyr, which is typical of a strong cool-core cluster (e.g., Peterson & Fabian 2006). Russell et al. (2010) suggested that the QSO had not significantly affected the large-scale

ICM properties, i.e., the AGN feedback to the ICM is not apparently seen in this object.

5.2.2 *Suzaku* Observations of H 1821+643

H 1821+643 is located on (R.A., Dec.) = (18h21m57.3s, +64d20m36s). An $1''$ corresponds to 4.5 kpc at the rest frame of $z = 0.297$. *Suzaku* observations of H 1821+643 were performed on 2013 April 16 and 20 (ObsID: 708037010 and 708037020, PI: C.S. Reynolds). After the standard data reduction described in section 5.1.3, total exposures of 374.8 ks and 360.0 ks for the XIS and the HXD, respectively, were obtained. The XIS data were extracted from a circular region with a radius of $3'$ centered on the target. We employed the ARF of the HXD for the XIS nominal position. For the CXB, the ARF for the flat sky was used.

5.2.3 Analyses of the *Suzaku* X-ray Spectra of H 1821+643

We followed the data reduction procedures presented in Section 5.1.3. We subtracted the NXB spectra of the XIS and the HXD from the X-ray spectra within the $r < 3'$ region. A column density of the Galactic absorption toward this source is $3.4 \times 10^{20}\,\mathrm{cm}^{-2}$ (Kalberla et al. 2005) and the redshift of H 1821+643 is $z = 0.297$. We fixed these values in our spectral fits.

After the subtraction of the NXB, the count rate of the HXD in the $16 - 40$ keV band is $(4.56 \pm 0.08) \times 10^{-2}\,\mathrm{count\,s}^{-1}$, which corresponds to 18.9 % of the NXB. Since the contribution of the CXB in this band is 5.9 %, the source flux of the HXD is 13 %, which is significantly larger than that of systematic errors in the NXB model, (Fukazawa et al. 2009; Takahashi et al. 2010). Since Fang et al. (2002) reported a presence of a soft X-ray excess below 1 keV, we ignored the X-ray band below 1 keV in the XIS spectra to exclude a contamination from the soft X-ray excess. We hence used the X-ray spectra in $1.0 - 40$ keV in the spectral analyses.

Figure 5.7 shows the X-ray spectra obtained with the *Suzaku*/XIS in the iron K-band at the observer's frame. We detect the lines of Fe I, Fe XXV, and Fe XXVI clearly for the first time. The EW of Fe I is 42^{+5}_{-4} eV at the rest frame, while the EW of Fe XXV is 77^{+5}_{-6} eV at the rest frame. The EW of Fe I is smaller than 113^{+42}_{-36} eV obtained by the Fang et al. (2002) with *Chandra*/HETG. This might be due to source variability or to the fact that a contribution of the Fe XXV line was neglected in the analysis by Fang et al. (2002). In fact, we obtain the sum of EWs of Fe I plus Fe XXV is ~ 120 eV, which is consistent with the EW of Fe I reported by them.

The X-ray emission from H 1821+643 should consist of many components, i.e., thermal

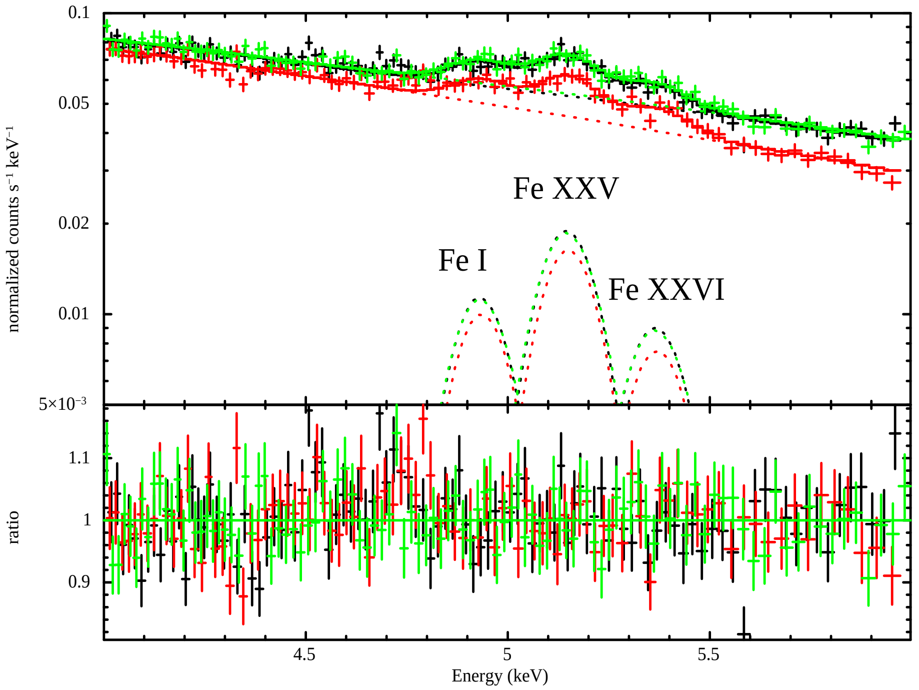

Figure 5.7: X-ray spectra in Fe K-band at observer's frame obtained with *Suzaku*/XIS. 縲 The line colors are the same as the bottom right panel of Figure 5.2.

emissions from the ICM in the center (low temperature component), in the entire region (high temperature component), and the emission from the central QSO. To determine the temperature of the thermal emission from the ICM in the entire region, which is dominant in the ICM thermal emission, we calculate the temperature with the line flux ratio of Fe XXV to Fe XXVI. Since the line flux of Fe XXV is $1.80^{+0.13}_{-0.12} \times 10^{-5}\,\mathrm{photons\,cm^{-2}\,s^{-1}}$ and that of Fe XXVI is $8.90^{+1.19}_{-1.22} \times 10^{-6}\,\mathrm{photons\,cm^{-2}\,s^{-1}}$, the flux ratio becomes $0.493^{+0.07}_{-0.08}$. Figure 5.8 shows the flux ratio of Fe XXV to Fe XXVI as a function of plasma temperature in the kT range of $2-16\,\mathrm{keV}$. Observed flux ratio of ~ 0.5 corresponds to $kT \sim 8.0\,\mathrm{keV}$. We thus fixed the ICM temperature of the entire region at 8.0 keV in our spectral analysis. We also fixed the metal abundance of the ICM to 0.3 solar, which is typical for clusters (e.g., Matsushita 2011) and is consistent with the previous result of this source obtained by Russell et al. (2010).

We show the *Suzaku*/XIS & HXD spectra in $1-40\,\mathrm{keV}$ in Figure 5.9. To fit the X-ray spectra of the XIS and the HXD, we employ two temperature model for the ICM in the center and in the entire region, and a (direct) power-law component plus a single Gaussian line from Fe I for the emission from the QSO. The model is schematically given as **wabs** × (**APEC**$_{\mathrm{low}}$ + **APEC**$_{\mathrm{high}}$ + **zwabs** × **power-law** + **zgauss**). As mentioned above, we fixed some parameters for **APEC**$_{\mathrm{high}}$ model. Moreover, to describe the thermal

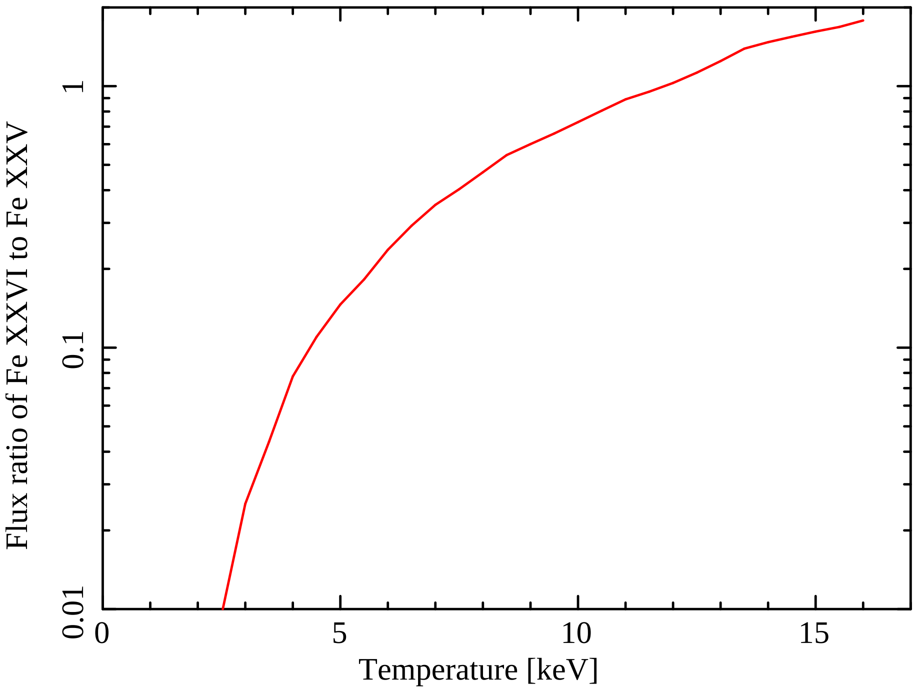

Figure 5.8: Flux ratio of Fe XXV to Fe XXVI as a function of plasma temperature in the kT range of 2 – 16 keV. The flux ratio is calculated with the APEC model in XSPEC.

emission from the cluster center, we fixed the abundance of $\mathbf{APEC}_{\rm low}$ to 0.5 solar, which is typical for a low temperature component in cluster cores and is consistent with that obtained by Russell et al. (2010). The fit shows the temperature of low-temperature (low-T) plasma to be $kT = 1.14^{+0.04}_{-0.08}$ keV, the photon index to be $\Gamma = 1.75 \pm 0.02$, and the EW of the Fe I to the power-law component of the type 1 QSO is 82 ± 7 eV at the rest frame. The upper limit of the absorption column density at the QSO rest frame is obtained as $N_{\rm H} < 10^{20}\,{\rm cm}^{-2}$. We, however, find an excess of the data to the model in the HXD band of 16 – 25 keV, which may indicate presence of a Compton hump, which is a feature expected for a reflection component (e.g., Miller 2007).

We hence apply a reflection model of **pexmon**. The bottom panel of Figure 5.9 shows the X-ray spectra fitted with a model **wabs** × ($\mathbf{APEC}_{\rm low}$ + $\mathbf{APEC}_{\rm high}$ + **zwabs** × **power-law** + **pexmon**). The cut-off energy of the reflection component is fixed at 300 keV, and the abundance of **pexmon** is 1 solar including that of iron. The inclination angle (θ_i) is also fixed to 30°. The spectral fit with this model yields the temperature of the low-T plasma to be $kT = 1.04^{+0.05}_{-0.04}$ keV, and the photon index of the power law component to be $\Gamma = 1.88 \pm 0.02$, and the reflection fraction ($|R| = \Omega/2\pi$) to be $|R| = 0.80^{+0.06}_{-0.07}$. If we fix θ_i to 0°, $|R|$ becomes $0.75^{+0.07}_{-0.05}$. Table 5.2 summarizes the best-fit results of the spectral fitting.

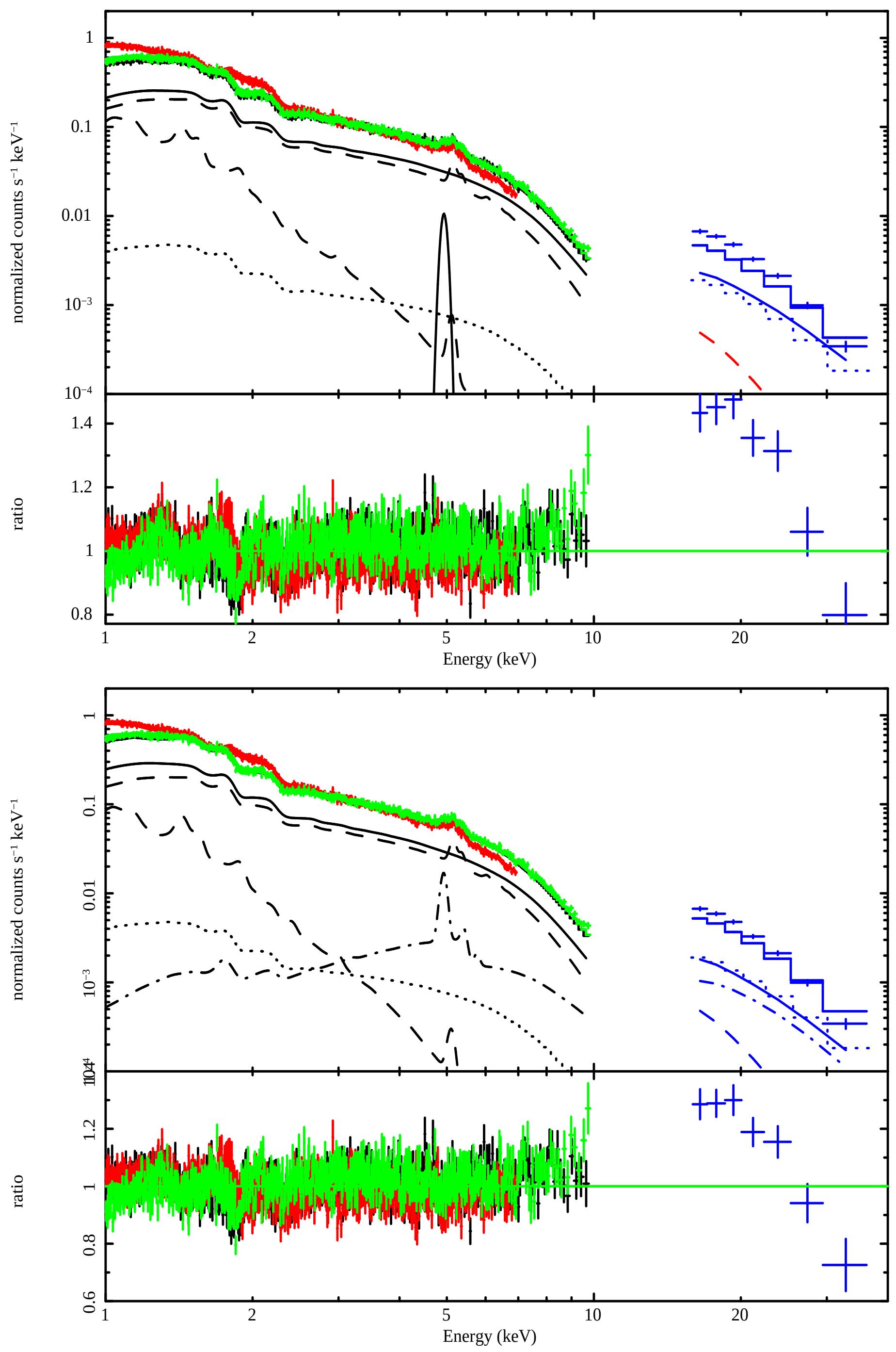

Figure 5.9: X-ray spectra of H 1821+643 in $1-40$ keV obtained with the *Suzaku*/XIS & HXD. Top panel: X-ray spectra fitted with two thermal components, a power-law component, and a Gaussian line representing Fe I. The same colors and lines are used as in Figure 5.3. We found an excess in the HXD band of $16-25$ keV, which suggest presence of the Compton hump, i.e., a reflection component. Bottom panel: X-ray spectra fitted with two thermal emissions, a direct power-law component, and a reflection component. The same colors and lines are used as in Figure 5.5.

Table 5.2: Best-fit Results of the Spectral Fitting with the *Suzaku*/XIS & HXD in the $1-40\,\mathrm{keV}$ band.

Fitting model	The ICM emission		Type 1 QSO emission		χ^2/d.o.f.
2APEC+PL+zgauss	kT_{high} (keV)	8.0 (fix)	Photon index	1.75 ± 0.02	3307/1790
	$Z_{\odot\mathrm{high}}$ (solar)	0.3 (fix)	EW of Fe I (eV)	82 ± 7	
	kT_{low} (keV)	$1.14^{+0.04}_{-0.08}$	N_{H} ($10^{22}\,\mathrm{cm}^{-2}$)	< 1	
	$Z_{\odot\mathrm{low}}$ (solar)	0.5 (fix)			
	Redshift	0.297 (fix)			
2APEC+PL+pexmon	kT_{high} (keV)	8.0 (fix)	Photon index	1.88 ± 0.02	3048/1791
	$Z_{\odot\mathrm{high}}$ (solar)	0.3 (fix)	N_{H} ($10^{22}\,\mathrm{cm}^{-2}$)	< 1	
	kT_{low} (keV)	$1.04^{+0.05}_{-0.04}$	$\lvert R\rvert(=\Omega/2\pi)$	$0.80^{+0.06}_{-0.07}$	
	$Z_{\odot\mathrm{low}}$ (solar)	0.5 (fix)	$Z_{\odot}$ (solar)	1.0 (fix)	
	Redshift	0.297 (fix)	cut-off (keV)	300 (fix)	

5.2.4 Discussion and Summary on the X-ray Properties of H 1821+643

With the X-ray spectra in the $1.0-40\,\mathrm{keV}$ band obtained with the *Suzaku*/XIS & HXD, we have revealed the X-ray properties of the type 1 QSO in the BCG of H 1821+643and the ICM of the cluster hosting it. The thermal emission from the ICM consists of two temperature plasmas; one has a temperature of $\sim 8.0\,\mathrm{keV}$, which dominates the ICM thermal emission in the entire cluster, and the other has a temperature of $\sim 1.0\,\mathrm{keV}$, which is distributed within the cluster core. Both temperatures are consistent with those obtained by Russell et al. (2010) with the *Chandra*/ACIS-S. The X-ray luminosity of the ICM in the $2-10\,\mathrm{keV}$ band was $(2.1 \pm 0.2) \times 10^{45}\,\mathrm{erg\,s^{-1}}$ within $r < 3'$ region.

We clearly detected the lines of Fe I, Fe XXV, and Fe XXVI separately, for the first time. The latter two are attributed to the thermal emission from the ICM, while the Fe I line is most likely a fluorescence line from neutral matter around the SMBH, e.g., an accretion disk and/or a tours. The EW of Fe I was $82 \pm 7\,\mathrm{eV}$ at the rest frame, while only the upper limit of the intrinsic absorption was obtained; $N_{\mathrm{H}}< 1 \times 10^{20}\,\mathrm{cm}^{-2}$, which is consistent with that reported by Fang et al. (2002). The X-ray luminosity of the type 1 QSO in $2-10\,\mathrm{keV}$ was $(2.16 \pm 0.02) \times 10^{45}\,\mathrm{erg\,s^{-1}}$, leading to the accretion rate of $\sim 37\,M_{\odot}\,\mathrm{yr}^{-1}$ assuming the accretion efficiency of 0.1, which corresponds to the 57 % of the Eddington luminosity. This is consistent with that derived in Russell et al. (2010). In the discussion in following chapters, we refer the X-ray luminosity in $10-50\,\mathrm{keV}$ is $(3.2 \pm 0.1) \times 10^{45}\,\mathrm{erg\,s^{-1}}$ obtained by us.

The spectral fit with a reflection model enables us to evaluate the geometry of the reflector, possibly a torus. The reflection fraction (R) of the reflector is obtained as $R = 0.80^{+0.06}_{-0.07}$ assuming the inclination angle (θ_i) of 30°. If we fix $\theta_i = 0°$, the R becomes $0.75^{+0.07}_{-0.05}$. These indicate that the covering factor of the reflector larger than 0.7 even if we observe this type 1 QSO in a face on geometry. The values of R for H 1821+643in these assumptions are comparable to that obtained for the type 2 QSO in the BCG of the Phoenix cluster. We will discuss more details of the properties of the type 1 QSO in the BCG of H 1821+643 in Chapter 7.

Chapter 6

Other Sample of Type 2 QSOs

In this chapter, we describe the results of the *Suzaku* observations of three type 2 QSOs. The first target is in the central galaxy of clusters of galaxies IRAS 09104+4109 and the second and third are ESP 39607 and 3C 433, respectively, which are in filed galaxies.

IRAS 09104+4109 is the first type 2 QSO that was discovered in the BCG of a rich cluster of galaxies was (e.g., Kleinmann et al. 1988; Iwasawa et al. 2001). Although extensive studies have been made on this source, the source was not included in our sample of luminous AGNs in BCGs described in Chapter 4. This is because, IRAS 09104+4109 is not included either in the *Planck* SZ cluster catalogue and the *Swift*/BAT 70-Month catalogue. As will be explained in Section 7.5.1, the hard X-ray luminosity of this QSO is just below the sensitivity limit of the *Swift*/BAT 70-Month catalogue, and the mass of the host cluster of IRAS 09104+4109estimated from the X-ray observations is also just below the threshold of the *Planck* SZ cluster catalogue. We hence have enough reason to add this source to supplementary sample of luminous AGNs in BCGs.

We also search for type 2 QSOs in field galaxies as control sample. By referring the 1210 sources in the *Swift*/BAT 70-Month catalogue and the target list observed with we find 16 sources included in both at redshift of $z > 0.2$. Among them, the number of sources identified with type 2 AGNs based on the column 20 of the *Swift*/BAT 70-Month catalogue is 2. One is the Phoenix cluster, and the other is ESP 39607. If we limit those sources of which redshift $z > 0.1$, we obtain the Phoenix cluster, ESP 39607, and 3C 433. As will be examined in Section 6.4, ESP 39607 and 3C 433 do not reside in rich clusters. We thus add these two source to the control sample of type 2 QSOs in field galaxies not in BCGs of clusters.

6.1 Previous Results

6.1.1 IRAS 09104+4109

IRAS 09104+4109 was first discovered as one of the hyper-luminous infrared galaxies detected by the infrared satellite *IRAS* survey (Kleinmann et al. 1988). This "galaxy" is located in redshift $z = 0.442$ (Kleinmann et al. 1988). A series of infrared (IR) observations clarified that a dust-enshrouded and luminous SMBH (i.e., type 2 QSO) exists in the central nuclear region (e.g., Kleinmann et al. 1988; Taniguchi et al. 1997). On the other hand, the *ROSAT*/High Resolution Imager (HRI) observation of this source revealed an spatial extended X-ray emission from the ICM, which indicated that this galaxy resides at the center of a cluster of galaxies (Fabian & Crawford 1995). IRAS 09104+4109 is the first case of a type 2 QSO in the BCGs of clusters of galaxies. *ROSAT* observations also showed that this cluster has a massive cooling flow (Fabian & Crawford 1995; Crawford & Vanderriest 1996). The star formation rate of the BCG of IRAS 09104+4109 is estimated to be $41 \pm 12\,M_\odot\,\mathrm{yr}^{-1}$ (Bildfell et al. 2008). Hereafter, we call the host cluster IRAS 09104+4109 in this work.

Iwasawa et al. (2001) discovered a strong neutral iron K-line (Fe I) for the first time in the X-ray spectrum of this the type 2 QSO with *Chandra*. The Fe I line is originated in a fluorescence line from surrounding matter around the SMBH, most likely a torus. With *XMM-Newton* 14 ks observations, Piconcelli et al. (2007) obtained the EW of Fe I of $\sim 400\,\mathrm{eV}$ to the direct power law component at the rest frame and the column density (N_H) of $5 \times 10^{23}\,\mathrm{cm}^{-2}$. Vignali et al. (2011) confirmed the EW of Fe I is $\sim 400\,\mathrm{eV}$ at the rest frame based on the 76.2 ks observation of this source with *Chandra*. They also reported that the N_H of the torus is $\sim 3 \times 10^{23}\,\mathrm{cm}^{-2}$, which is almost consistent with that by Piconcelli et al. (2007). The X-ray luminosity of the type 2 QSO in $2 - 10\,\mathrm{keV}$ ($L_{\mathrm{X},2-10\,\mathrm{keV}}$) is $\sim 3 \times 10^{44}\,\mathrm{erg\,s}^{-1}$ according to Vignali et al. (2011). Piconcelli et al. (2007) estimated that the mass of SMBH in the BCG is $\sim 2.4 \times 10^9\,M_\odot$. The mass of the putative torus of which size is $\sim 100\,\mathrm{pc}$ is estimated to be $\sim 1 \times 10^9\,M_\odot$(Taniguchi et al. 1997).

Iwasawa et al. (2001) also reported that the temperature of the ICM near the central region is $\sim 3.3\,\mathrm{keV}$, which was consistent with that measured by Piconcelli et al. (2007). The abundance of the ICM was determined to be 0.47 ± 0.10 solar by Piconcelli et al. (2007). O'Sullivan et al. (2012) investigated the radial profiles of temperature and abundance of the ICM. They obtained a maximum temperature of $7.7^{+0.7}_{-0.6}\,\mathrm{keV}$ at $\sim 200\,\mathrm{kpc}$, and a minimum temperature of $3.9 \pm 0.3\,\mathrm{keV}$ in the central region ($5'' \sim 28\,\mathrm{kpc}$). In the outer region ($\sim 250 - 900\,\mathrm{kpc}$) the temperature was measure to be about 7 keV. The abundance of the ICM is 0.6 solar, almost constant over the entire region. O'Sullivan et al. (2012)

evaluated the total mass of $(5.83 \pm 1.69) \times 10^{14}\,M_\odot$ and $(8.10 \pm 2.64) \times 10^{14}\,M_\odot$ within r_{500} and r_{200}, where r_{500} and r_{200} correspond to $\sim 1.09\,\mathrm{Mpc}$ and $\sim 1.65\,\mathrm{Mpc}$, respectively. O'Sullivan et al. (2012) estimated the cooling rate of $\sim 235\,M_\odot\,\mathrm{yr}^{-1}$ within 27 kpc with Equation 2.11.

A hard X-ray component from the type 2 QSO was detected with *BeppoSAX* (Boella et al. 1997) by Iwasawa et al. (2001). Nevertheless, Piconcelli et al. (2008) suggested that it might be a contamination from other AGNs around IRAS 09104+4109. Vignali et al. (2011) claimed that contamination from NGC 2785, a nearby ($z = 0.009$) type 2 AGN located only $17'$ apart from IRAS 09104+4109, could be significant based on the *Swift*/BAT 54-Month catalogue (Cusumano et al. 2010b). Chiang et al. (2013) investigated the hard X-ray component and its origin further with *Suzaku*. They carried out the *Suzaku* observations by shifting the pointing direction to $6'$ west from the center and taking a roll angle that minimizes the contamination from NGC 2785. As a result, Chiang et al. (2013) could not detected a significant flux from of the the type 2 QSO in IRAS 09104+4109with the *Suzaku*/HXD. The upper limit of the background-subtracted source flux provided by them was $\sim 4.25 \times 10^{-12}\,\mathrm{erg\,cm^{-2}\,s^{-1}}$ in $14 - 45\,\mathrm{keV}$.

6.1.2 ESP 39607

ESP 39607 is a galaxy at redshift $z = 0.201$ discovered in the European Southern Observatory (ESO) Slice Project (ESP; Vettolani et al. 1997, 1998). Although ESP 39607 was not detected in the *ROSAT* All-Sky Survey, the source was detected in hard X-ray all-sky surveys, including the *INTEGRAL*/IBIS 7-year All-Sky Hard X-Ray Survey (Krivonos et al. 2010) and the *Swift*/BAT 70-Month catalogue (Baumgartner et al. 2013). This fact implies that X-ray emission from the SMBH might be heavily absorbed, though detailed X-ray spectrum has not yet been obtained in pointing observations. Masetti et al. (2010) carried out an optical spectroscopy of ESP 39607 with the 1.5 m R-C Spectrograph at the Cerro Tololo Interamerican Observatory (CTIO) and classified the source as type 2 AGN.

6.1.3 3C 433

3C 433 is one of narrow-line radio galaxies (NLRG) at low-redshift $z = 0.102$ (Schmidt 1965). 3C 433 has an unusual extended radio emissions (van Breugel et al. 1983), with which (Wills et al. 2002) classified this source as Fanaroff-Riley Class I/II (FR I/II; Fanaroff & Riley 1974) .

As defined by Fanaroff & Riley (1974), FR I sources have prominent jets in central region tapering toward outer regions, whereas FR II sources show collimated jets terminating in luminous hotspots and complex lobes and have higher radio luminosity than FE I sources. Very small fraction (less than 1 %) radio sources have both FR I jet and FR II lobe on the opposite sides of the core (Gawroński et al. 2006). Gopal-Krishna & Wiita (2000) suggested that such structure, i,e,, hybrid morphology radio sources (HYMORS) they named, is most plausibly due to the propagation of twin jets into an asymmetric medium. 3C 433 has a luminous FR II lobe toward southern direction including a primary hot-spot and bright outer ridges (Miller & Brandt 2009). On the other hand, a knotty FR I jet is observed toward northern direction and it stretches perpendicularly to the east direction (Miller & Brandt 2009). Black et al. (1992) found that there are two core-like components (C1 and C2) separated by only 1 kpc into northern direction and suggested that the CI knot is most likely an inner jet knot.

The complex southern FR II lobe contains considerable cold gases, as indicated by H I measurements (e.g., Mirabel 1989; Morganti et al. 2003) (Ogle et al. 2006) found strong silicate absorption features in the mid-IR spectrum of this source obtained with *Spitzer*, where *Spitzer* is the infrared observatory of NASA's Great mission (Werner et al. 2004). Ogle et al. (2006) suggested that it is evidence for a kpc scale screen of cold dust in the host galaxy. The SFR in 3C 433 was measured to be also $1 \sim 2\,M_{\odot}\,\mathrm{yr}^{-1}$ based on the *Spitzer* observation of this source by Ogle et al. (2010).

3C 433 was not detected in the *ROSAT* All-Sky Survey, while the sources was detected with *Swift* in hard X-ray band (Baumgartner et al. 2013). With *Chandra* 37.2ks observations of this source, Miller & Brandt (2009) found a heavily absorbed component from the nuclear region, whose absorption column density was $N_{\mathrm{H}} = 8.3 \times 10^{22}\,\mathrm{cm}^{-2}$. This indicates that 3C 433 is classified as a type 2 AGN, though Fe I line was not significantly detected by Miller & Brandt (2009). The upper limit of the EW of the Fe I line was obtained as 85 eV at the rest frame.

A soft X-ray excess seen in the X-ray spectrum of the nuclear region could be reproduced either with a power-law model of $\Gamma = 2.2 \pm 0.8$ or a thermal bremsstrahlung of $kT = 1.2^{+14.2}_{-0.6}$ keV (they noted that the upper limit for the temperature was poorly constrained).

Moreover, Miller & Brandt (2009) revealed a soft diffuse emission, which surrounds the nuclear region and extends particularly toward the northeast direction by $\sim 9-11$ kpc. This diffuse emission, reproduced with a thermal bremsstrahlung of $kT = 1.37^{+1.66}_{-0.59}$ keV, could be associated with a hot gas often observed around FR II lobes (Miller & Brandt 2009). Miller & Brandt (2009) suggested that the hot gas may be experiencing a quasi-continuous heating by the northern jet. Miller & Brandt (2009) further found that the X-ray spectrum of the CI region is dominated by hard X-ray flux, indicating that heavily absorption ($N_{\mathrm{H}} > 1,7 \times 10^{22}\,\mathrm{cm}^{-2}$) is significant even at ~ 1 kpc from the core. This is much larger than typically assumed size of a torus (e.g., Maiolino & Risaliti 2007; Maiolino 2008). However, Miller & Brandt (2009) suggested that the location of the CI knot is well within the scale of the dust structures seen in the host galaxy of 3C 433. The CI knot may happen to lie along a line of sight that passes though a dense dust cloud or lane (Miller & Brandt 2009).

6.2 Observations and Data Reductions

We study X-ray properties of the type 2 QSOs in IRAS 09104+4109, ESP 39607, and 3C 433, by employing the archival data of *Suzaku* observations. We summarize the log of *Suzaku* observations of these sources in Table 6.1. The effective exposure time for the XIS and the HXD, column 6 of Table 6.1, are obtained after applying the standard data reduction described in Chapter 5.1.3. The PI of each observation is C. Chiang for IRAS 09104+4109 and W. Baumgartner for ESP 39607 and 3C 433.

For all the three targets, the XIS data were extracted from a circular region with a radius of $3'$ centered on the coordinate of each target. We employed the HXD ARFs supplied for observations at the XIS nominal position for ESP 39607 and 3C 433. On the other hand, as mentioned Section 6.1.1, since the aim point of the XRT during the observation of IRAS 09104+4109 is not at the XIS nominal position, we employed the HXD ARF for the HXD nominal position, following the procedure adopted by Chiang et al. (2013). For the CXB, we applied the ARF of the flat sky for all targets.

The redshifts of IRAS 09104+4109, ESP 39607, and 3C 433 are $z = 0.442, 0.201$, and 0.102, respectively. Thus, an $1''$ at each target corresponds to 5.7 kpc, 3.3 kpc, and 1.9 kpc, respectively.

Table 6.1: Summary of *Suzaku* Observations of the Type 2 QSOs in IRAS 09104+4109, ESP 39607, and 3C 433.

Target	ObsID	Obs. Date	R.A.^{1}	Dec.^{1}	Exposure^2	
IRAS 09104+4109	706038010	2011-Nov-18	09h13m45.5s	+40d56m28s	113 ks	71.3 ks
ESP 39607	705048010	2010-Dec-19	00h46m20.6s	−40d05m49s	60.7 ks	45.3 ks
3C 433	705050010	2010-Nov-06	21h23m44.5s	+25d04m12s	62.5 ks	41.3 ks

^{1}: Coordinate of the target not the aim point of the XRT.

^{2}: Effective exposure times of the XIS (left) and the HXD (right).

6.3 Spectral Analyses and Results

Similar procedures were applied to fit the X-ray spectra obtained with the *Suzaku*/XIS & HXD. The NXB spectra of the XIS and the HXD were subtracted. A column density ($N_{\rm H}$) of the Galactic absorption toward IRAS 09104+4109, ESP 39607, and 3C 433 was estimated to be $1.42 \times 10^{20}\,{\rm cm}^{-2}$, $3.2 \times 10^{20}\,{\rm cm}^{-2}$, and $7.8 \times 10^{20}\,{\rm cm}^{-2}$, respectively, by Kalberla et al. (2005). We fixed $N_{\rm H}$ to these values in our spectral fitting. We also fixed the redshift at $z = 0.442, 0.201$, and 0.102 for IRAS 09104+4109, ESP 39607, and 3C 433, respectively.

In the case of IRAS 09104+4109, we found that the HXD count rate after subtracting the NXB was $1.6 \times 10^{-2}\,{\rm cts\,s}^{-1}$ in $16 - 40\,{\rm keV}$, which corresponds to 6.9 % of the NXB. Since the CXB flux for the HXD is estimated to be 5.9 % of the NXB, the source flux from the type 2 QSO corresponds to only 1.0 % of the NXB, smaller than systematic uncertainty of the NXB model (Takahashi et al. 2010). We thus confirmed the result by Chiang et al. (2013), i.e., no significant hard X-ray flux was detected in this source.

In the cases of ESP 39607 and 3C 433, the count rate of the HXD in the $16 - 40\,{\rm keV}$ band after subtracting the NXB was $(2.1 \pm 0.2) \times 10^{-2}\,{\rm count\,s}^{-1}$ and $(2.2 \pm 0.3) \times 10^{-2}\,{\rm count\,s}^{-1}$, respectively. They correspond to 8.7 % of the NXB and 8.9 % of the NXB. Since the contribution of the CXB in this band is 5.9 %, the hard X-ray ($16-40\,{\rm keV}$) source flux is 2.8 % and 3.0 % of the NXB, which is slightly larger than the systematic errors of the NXB model (e.g., Takahashi et al. 2010). Although the two sources ESP 39607 and 3C 433were not detected with the HXD significantly, we include the HXD spectrum in the spectral fitting for these sources.

We generated the NXB of the XIS by using `xisnxbgen` for IRAS 09104+4109, and modeled the CXB, MWH, and LHB component in the spectral fit as mentioned in Section 5.1.4. On the other hand, Chiang et al. (2013) extracted background spectra from a circular region with a radius of $180''$ where there are no apparent sources and employed them as the spectra representing the NXB, CXB, MWH, and LHB. The extraction region of the source spectra are also different in our analysis and that in Chiang et al. (2013); we set the radius of the region to be $r < 3'$, while Chiang et al. (2013) set it to be $r < 110''$ region.

Figure 6.1 shows the X-ray images of IRAS 09104+4109, ESP 39607, and 3C 433 in the $0.4 - 10\,{\rm keV}$ band obtained with *Suzaku*/XIS3. Each image shows a point source and no apparent diffuse emission is found. As mentioned above, only in the case of IRAS 09104+4109, the aim point of the observation was not at the coordinate of the target.

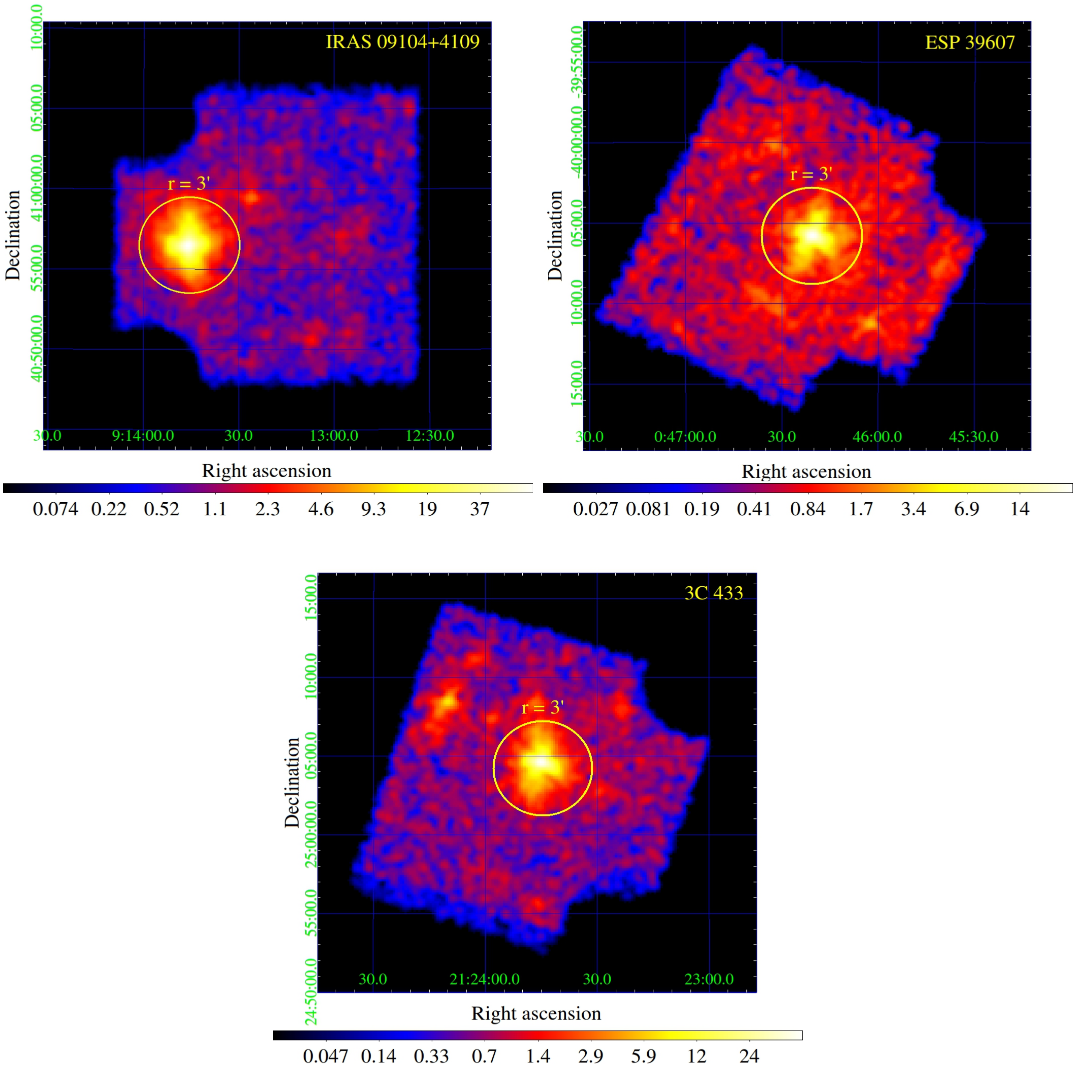

Figure 6.1: X-ray images of IRAS 09104+4109 (top left), ESP 39607 (top right), and 3C 433 (bottom) in the $0.4 - 10$ keV band obtained with *Suzaku*/XIS3. The yellow circle shows the region extracted X-ray spectra. In all the images, irradiation regions of the calibration sources of ^{55}Fe are excluded.

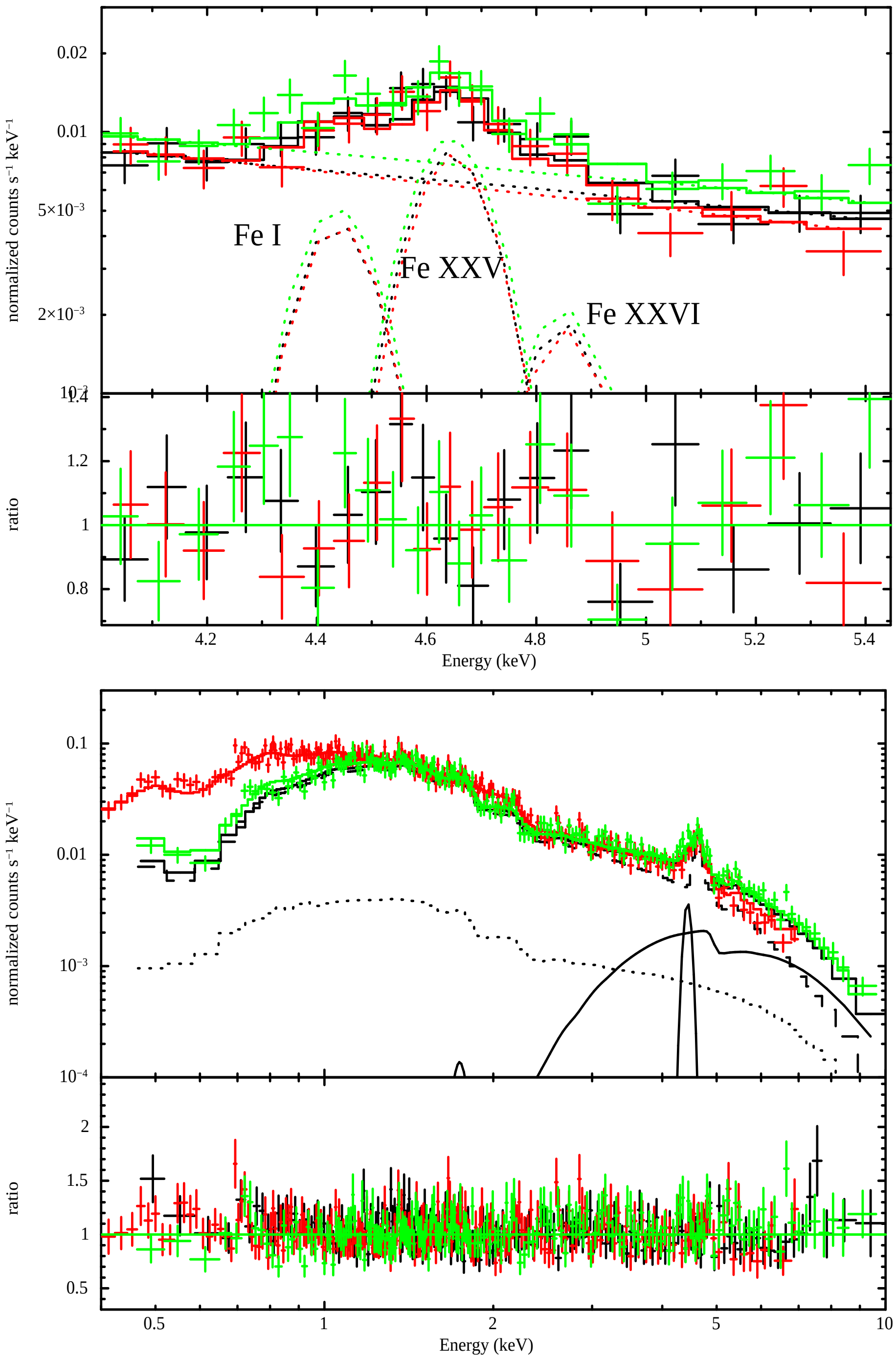

Figure 6.2: X-ray spectra of IRAS 09104+4109 obtained with the *Suzaku*/XIS. The ratios of the data to the model are plotted in the bottom panels. Top: X-ray spectra of IRAS 09104+4109 in iron K-band at the observer's frame. The Fe I, Fe XXV, and Fe XXVI lines are detected clearly. Bottom: X-ray spectra of IRAS 09104+4109 in 0.4 − 10 keV. The XIS0, 1, and 3 are shown in black, red, and green, respectively. The solid lines show the AGN emission, which consists of an absorbed power-law component and an Fe I line. The dashed line and dotted line represent the ICM thermal emission and the X-ray background models (Chapter 5.1.3), respectively.

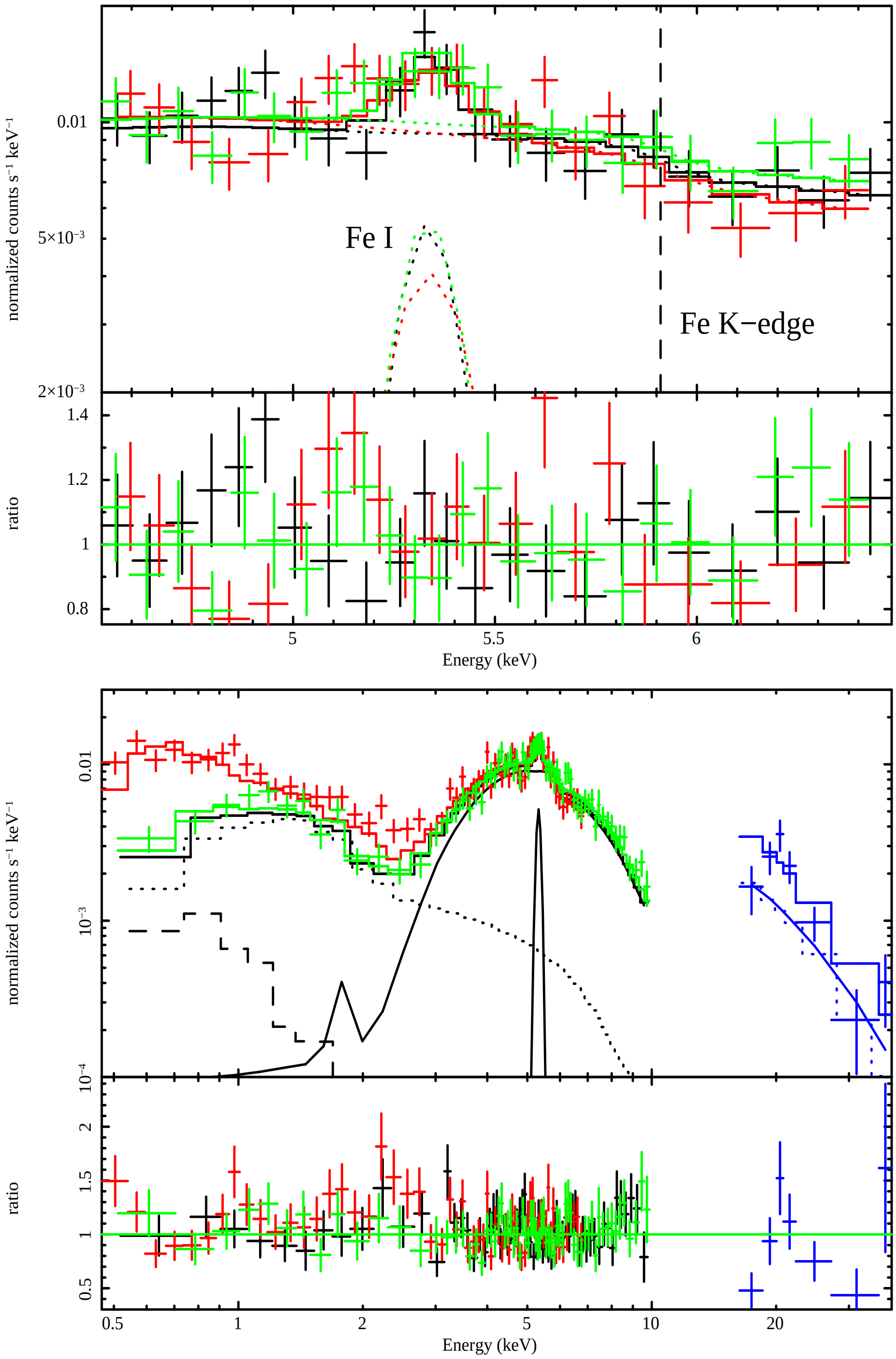

Figure 6.3: X-ray spectra of ESP 39607 with the *Suzaku*/XIS & HXD. The ratios of the data to the model are plotted in the bottom panels. Top panel: X-ray spectra in the iron K-band at the observer's frame. Bottom panel: X-ray spectra of ESP 39607 in 0.4−40 keV. The same colors and lines are used as those in Figure 6.2 for the *Suzaku*/XIS0, XIS1, and XIS3, respectively. The blue data points and lines show those for the HXD.

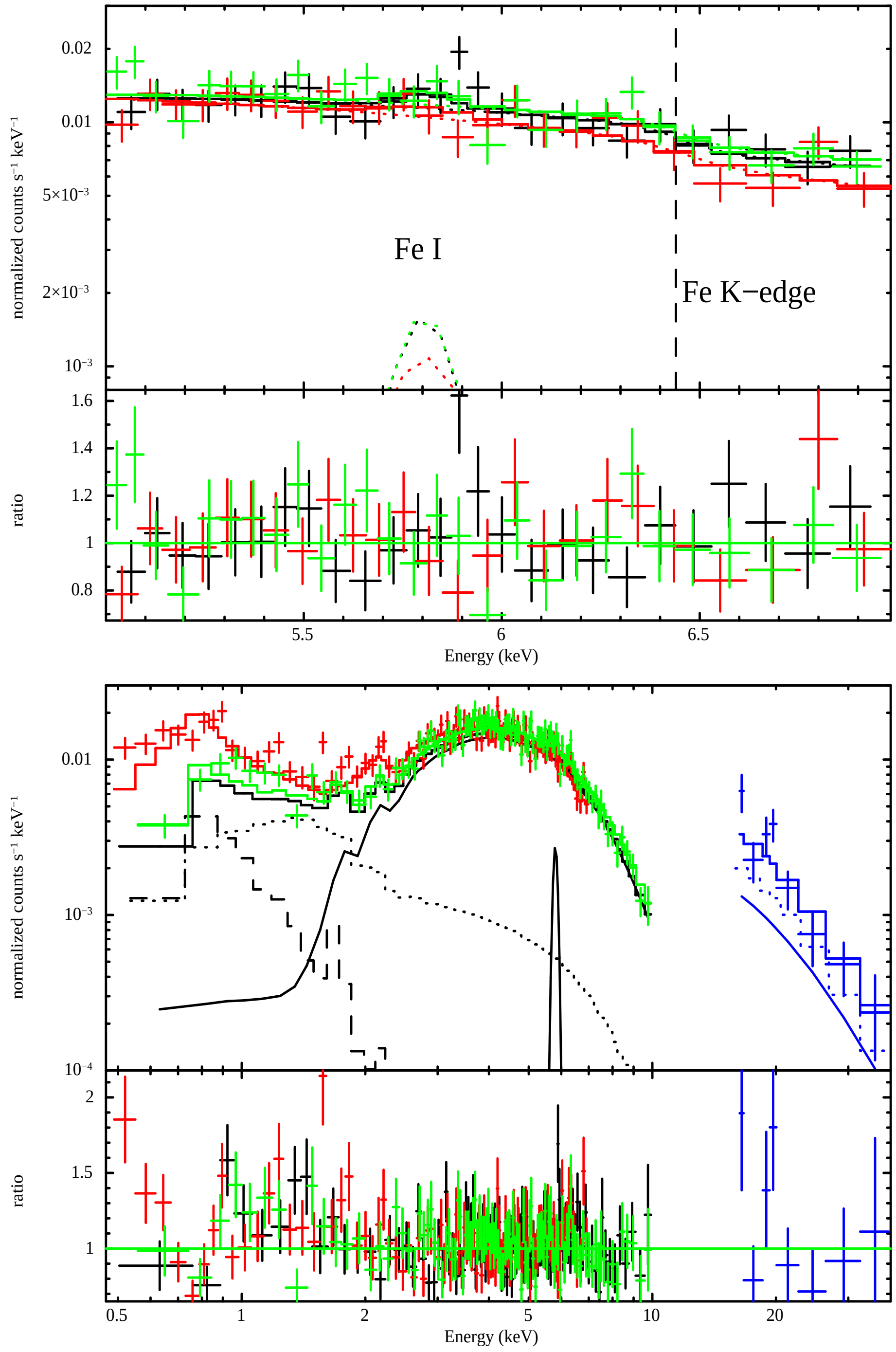

Figure 6.4: X-ray spectra of 3C 433 with the *Suzaku*/XIS & HXD. The ratios of the data to the model are plotted in the bottom panels. Top panel: X-ray spectra of 3C 433 in the iron K-band at the observer's frame. Bottom panel: X-ray spectra of 3C 433 in $0.4 - 40$ keV. The same colors and lines are used as those in Figure 6.3 for the *Suzaku*/XIS0, XIS1, XIS3, and the HXD, respectively.

We show the X-ray spectra of IRAS 09104+4109, ESP 39607, and 3C 433 obtained with the *Suzaku*/XIS & HXD. The top panels of Figure 6.2, Figure 6.3, and Figure 6.4 show the X-ray spectra in the iron K-band at the observer's frame. For IRAS 09104+4109, we detect a lump of emission lines consisting of Fe I, Fe XXV, and Fe XXVI. On the other hand, the Fe I line and a hint of the iron K-edge are observed in the X-ray spectra of ESP 39607 and 3C 433. No apparent indication of the emission lines of Fe XXV and Fe XXVI in the X-ray spectra of of ESP 39607 and 3C 433 suggests that the ICM thermal emission as found in rich clusters are not significant in these sources.

We next perform model fitting of wide band X-ray spectra of these sources. We show the X-ray spectra in the $0.4 - 40$ keV band ($0.4 - 10$ keV for IRAS 09104+4109) in the bottom panels of Figure 6.2, Figure 6.3, and Figure 6.4, respectively. To fit the X-ray spectrum of IRAS 09104+4109, we employ an emission model from a optically-thin single-temperature plasma (**APEC**) for the ICM thermal emission, and an absorbed power-law component and an Fe I line to reproduce the emission from the type 2 QSO in the BCG. Schematically the model is given as **wabs** × (**APEC** + **zwabs** × **power-law** + **zgauss**). We fixed a width of the Gaussian to 0 eV and its line energy is 6.40 keV at the rest frame. The same model is applied to the X-ray spectra of ESP 39607 and 3C 433, although the **APEC** model in these cases represents not necessarily the emission from the ICM but that from halo of the BCG. We hence fixed the abundance of the thermal emission to 1 solar.

We summarize the best-fit results of the wide band spectral analyses in Table 6.2 for IRAS 09104+4109, ESP 39607, and 3C 433, respectively. The temperature and abundance of the ICM in IRAS 09104+4109 is determined to be $kT = 4.65^{+0.39}_{-0.40}$ keV and $Z_\odot = 0.34 \pm 0.05$ solar, respectively. On the other hand, thermal emission in ESP 39607and in 3C 433, is reproduced with that with lower temperatures, i.e., $kT = 0.29^{+0.39}_{-0.07}$ keV for ESP 39607 and $kT = 0.96^{+0.06}_{-0.07}$ keV for 3C 433. The X-ray spectrum of the type 2 QSO in IRAS 09104+4109 is characterized with an absorbed power-law model with a photon index of $\Gamma = 1.13^{+1.24}_{-0.76}$ and a column density of $N_\mathrm{H} = 2.9^{+5.8}_{-1.7} \times 10^{23}\,\mathrm{cm}^{-2}$, plus an Fe I line with an EW of 540 ± 150 eV at the rest frame. The type 2 QSO in ESP 39607has an X-ray spectrum consisting of an absorbed power-law model with a photon index of $\Gamma = 1.42^{+0.15}_{-0.14}$, and a column density of $N_\mathrm{H} = 2.8 \pm 0.3 \times 10^{23}\,\mathrm{cm}^{-2}$, and an Fe I line with an EW of Fe I of 124^{+52}_{-31} eV at the rest frame. That in 3C 433 is characterized with a similar model but with different parameters, i.e., $\Gamma = 1.74 \pm 0.10$, $N_\mathrm{H} = (9.2 \pm 0.6) \times 10^{22}\,\mathrm{cm}^{-2}$, and the EW=$57^{+30}_{-27}$ eV.

Table 6.2: Best-fit Results of the Spectral Fitting for IRAS 09104+4109, ESP 39607, and 3C 433 with *Suzaku*.

Target	Thermal emission		AGN components		χ^2/d.o.f.
IRAS 09104+4109	kT (keV)	$4.65^{+0.39}_{-0.40}$	N_{H} ($\times10^{22}\,\mathrm{cm}^{-2}$)	29^{+58}_{-17}	597/578
	$Z_{\odot}$ (solar)	0.34 ± 0.05	Photon index	$1.13^{+1.24}_{-0.76}$	
	Redshift	0.442 (fix)	EW of Fe I (eV)	540 ± 150	
ESP 39607	kT (keV)	$0.29^{+0.39}_{-0.07}$	N_{H} ($\times10^{22}\,\mathrm{cm}^{-2}$)	28 ± 3	239/209
	$Z_{\odot}$ (solar)	1.0 (fix)	Photon index	$1.42^{+0.15}_{-0.14}$	
	Redshift	0.201 (fix)	EW of Fe I (eV)	124^{+52}_{-31}	
3C 433	kT (keV)	$0.96^{+0.06}_{-0.07}$	N_{H} ($\times10^{22}\,\mathrm{cm}^{-2}$)	9.2 ± 0.6	343/311
	$Z_{\odot}$ (solar)	1.0 (fix)	Photon index	1.74 ± 0.10	
	Redshift	0.102 (fix)	EW of Fe I (eV)	57^{+30}_{-27}	

6.4 Discussion on the X-ray Properties of the Three Type 2 QSOs

We find that X-ray spectra of IRAS 09104+4109, ESP 39607, and 3C 433 extracted from the $r < 3'$ region at the center are well-reproduced with a combination of a thermal component from the ICM or from the halo of the galaxies and an AGN component, which is described with an absorbed power-law component plus an Fe I line. We separately discuss these components here.

6.4.1 Thermal Emission from IRAS 09104+4109, ESP 39607, and 3C 433

We detected Fe XXV and Fe XXVI lines in the X-ray spectra of IRAS 09104+4109, (top panel of Figure 6.2), which should have ICM in their origin. In fact, we have shown the wide band X-ray spectrum in $0.4 - 10$ keV requires an thermal emission component of which temperature of $kT = 4.65^{+0.39}_{-0.40}$ keV, which is consistent with that reported by Vignali et al. (2011). We also derived the metal abundance of the ICM to be 0.34 ± 0.05 solar for the first time in this source; this value is typical for a rich cluster (e.g., Matsushita 2011).

On the other hand, since there found no apparent Fe XXV and Fe XXVI lines in the X-ray spectra of ESP 39607 and 3C 433 (top panels of Figure 6.3 and Figure 6.4), the thermal emission is not significant or with a lower temperature in these sources. Out wide band X-ray spectral analysis show the latter is more likely. As shown in Table 6.2, the temperatures of the thermal components in these sources are lower than 1 keV. We suggest that these thermal components do not have their origin in the ICM but in halo of the host galaxies. We note that the temperature of $kT = 0.96^{+0.06}_{-0.07}$ keV obtained by us for 3C 433 is consistent with that reported by Miller & Brandt (2009) for the extended emission around the FR II lobe in this source. The X-ray luminosities in $2-10$ keV of the thermal emission components in ESP 39607 and 3C 433 are $4 \sim 5$ orders of magnitudes lower than the intrinsic luminosity of the AGN components. We consider the results justify our selection of these sources as type 2 QSOs in field galaxies not in rich clusters.

6.4.2 AGN Component in the Three Type 2 QSOs

Our analysis of the wide-band X-ray spectra obtained with the *Suzaku*/XIS & HXD revealed that three sources commonly have an absorbed power law component with an Fe I line, which is typical for type 2 AGNs.

We obtained the unobscured X-ray luminosities in the $2-10$ keV band of $L_{\mathrm{X},2-10} = 5.1^{+0.4}_{-0.6} \times 10^{44}\,\mathrm{erg\,s^{-1}}$, $L_{\mathrm{X},2-10} = 4.7^{+0.1}_{-0.2} \times 10^{44}\,\mathrm{erg\,s^{-1}}$, and $L_{\mathrm{X},2-10} = (1.2 \pm 0.1) \times 10^{44}\,\mathrm{erg\,s^{-1}}$, for IRAS 09104+4109, ESP 39607, and 3C 433, respectively. The X-ray luminosity in $2-10$ keV of (the QSO in) IRAS 09104+4109 derived by us was not only consistent with that reported by Chiang et al. (2013), but also was within the range of previous observations, i.e., from ($\sim 3 \times 10^{44}\,\mathrm{erg\,s^{-1}}$; Vignali et al. 2011) to ($\sim 8 \times 10^{44}\,\mathrm{erg\,s^{-1}}$; Piconcelli et al. 2007). We note that the X-ray luminosity of 3C 433 was also consistent with that reported by Miller & Brandt (2009) with *Chandra* and *ASCA*. We also estimate the X-ray luminosity in the $10-50$ keV band for following discussions. Assuming that the AGN component has a simple power law spectrum with the photon index obtained by us in this energy range, the luminosities converted are $L_{\mathrm{X},10-50} = 1.5^{+0.4}_{-0.7} \times 10^{45}\,\mathrm{erg\,s^{-1}}$, $L_{\mathrm{X},10-50} = 1.2^{+0.1}_{-0.2} \times 10^{45}\,\mathrm{erg\,s^{-1}}$, and $L_{\mathrm{X},10-50} = (1.8 \pm 0.2) \times 10^{44}\,\mathrm{erg\,s^{-1}}$, for IRAS 09104+4109, ESP 39607, and 3C 433, respectively.

We can also estimate the accretion rate ($\dot{M}_{\mathrm{acc}}$) of each type 2 QSO by following Marconi et al. (2004) and assuming the accretion efficiency of 0.1. The accretion rate $\dot{M}_{\mathrm{acc}}$ derived in this way is $5\,M_{\odot}\,\mathrm{yr^{-1}}$, $4.8\,M_{\odot}\,\mathrm{yr^{-1}}$, and $0.7\,M_{\odot}\,\mathrm{yr^{-1}}$, for IRAS 09104+4109, ESP 39607, and 3C 433, respectively.

The EW of Fe I and N_{H} are also key parameters in following discussions. We first verify the consistency of the EW of Fe I derived by us and that reported by Chiang et al. (2013) for IRAS 09104+4109. The EW reported by Chiang et al. (2013) is that to the summed continuum of the thermal component and the AGN (power-law) component. The EW we obtain with the same definition is 107^{+50}_{-29} eV, which is consistent with that .reported by Chiang et al. (2013). The EW of Fe I line to the AGN component is more important for our discussion; that for IRAS 09104+4109 is 539 ± 150 eV. The EW of Fe I line to the AGN component for ESP 39607, and 3C 433 is 124^{+52}_{-31} eV, and 57^{+30}_{-27} eV, respectively. Note that the Fe I line was detected in ESP 39607 and 3C 433 for the first time and the EW of the line derived by us for 3C 433 is below its upper limit determined by Miller & Brandt (2009). The column densities of the AGN component are $2.9^{+5.8}_{-1.7} \times 10^{23}$ cm^{-2} for IRAS 09104+4109, $(2.8 \pm 0.3) \times 10^{23}$ cm^{-2} for ESP 39607, and $(9.2 \pm 0.6) \times 10^{22}$ cm^{-2} for 3C 433, respectively. The $N_{\rm H}$ values for IRAS 09104+4109 and 3C 433 are consistent with those reported by Vignali et al. (2011) and Miller & Brandt (2009), respectively.

6.5 Type 2 QSOs in BCGs versus Those in Field Galaxies

We have studied X-ray spectra of three type 2 QSOs in this chapter. One is that in IRAS 09104+4109, a type 2 QSO in a BCG of a rich cluster, which is supplementary sample of that in the Phoenix cluster. We also studied the other two type 2 QSOs not in rich clusters as control sample. Our goal is to find any systematic differences in the properties of QSOs in BCGs of rich clusters and those in field galaxies.

The unobscured X-ray luminosity Lx of AGNs is important to measure intrinsic activity of the SMBH in them. The column density $N_{\rm H}$ and the EW of Fe I line can provide the information on surrounding matter around the SMBH. As mentioned in Section 7.3, there is a anti-correlation between the EW of Fe I line and the X-ray luminosity ($L_{\rm X}$) known as the X-ray Baldwin effect, at least for the sources with lower luminosities. We should pay attention to the fact that the two type 2 QSOs in BCGs of rich clusters, IRAS 09104+4109 and the Phoenix cluster have extremely high luminosities among type 2 QSOs, but has relatively large EW of Fe I. We will examine significance of some of the possible differences between type 2 QSOs in BCGs and in field galaxies in the next Chapter. We will also discuss possible implications of each hypothesis.

Chapter 7

Discussion

In this chapter, we first summarize the observed properties of QSOs studied in this work. Second, we discuss the $N_{\rm H}$ − EW of Fe I relation of four type 2 QSOs, which reflects the torus geometry around the SMBH. Next, we discuss the relation between the EW and the X-ray luminosity, the X-ray Baldwin effect, for four type 2 QSOs and one type 1 QSO studied in this work. After that, we discuss the implication of our results on the association among cooling flow, star formation, and torus. Finally, we remark the future prospects based on our view point.

7.1 Observed Properties of Luminous AGNs in the BCGs and in the Field Galaxies

One of our aim is to search for luminous AGNs, i.e., QSOs, in BCGs of clusters of galaxies. By referring both the *Planck* SZ cluster catalogue and the *Swift*/BAT 70-Month catalogue, we find two clusters out of 861 clusters sample in which luminous AGNs with $\log L_{\rm X,14-195} > 45$ reside in their BCGs.

1. One is the Phoenix cluster, and the other is H 1821+643 (Table 4.1).
2. The fraction of such clusters is 2/861, i.e., 0.23 %.

Next, we analyze the X-ray spectra of the Phoenix cluster with the *Suzaku*/XIS & HXD, *Chandra*/ACIS-I, and *XMM-Newton*/EPIC and H 1821+643 with the *Suzaku*/XIS & HXD (Section 5.1 and Section 5.2). Either spectra consist of a thermal emission from the ICM and a non-thermal emission from the AGN. The AGN component is characterized as follows.

1. We detect the Fe I line in the AGN component of the X-ray spectra.

2. The power law continuum suffers heavy absorption for the AGN in the Phoenix cluster, but not for H 1821+643. This is consistent with the classification as type 2 QSO for the former and type 1 QSO for the latter.

3. The type 2 QSO in the Phoenix cluster has the EW of Fe I of 149^{+139}_{-58} eV and the X-ray luminosity of $L_{\mathrm{X},2-10} = (4.7 \pm 0.7) \times 10^{45}\,\mathrm{erg\,s^{-1}}$.

4. The type 1 QSO in H 1821+643 has the EW of Fe I of 82 ± 7 eV and the X-ray luminosity of $L_{\mathrm{X},2-10} = (2.16 \pm 0.02) \times 10^{45}\,\mathrm{erg\,s^{-1}}$.

5. When we included the reflection component in the fitting model, the reflection fractions ($|R| = \Omega/2\pi$) were determined to be $|R| = 0.77^{+0.48}_{-0.38}$ and $|R| = 0.80^{+0.06}_{-0.07}$, for the Phoenix cluster and H 1821+643, respectively.

In Chapter 6, we also analyze the X-ray spectra of three type 2 QSOs in IRAS 09104+4109, ESP 39607, and 3C 433. IRAS 09104+4109 is supplementary sample of the type 2 QSOs in the BCG of a rich cluster, as for the Phoenix cluster, while the type 2 QSOs of ESP 39607 and 3C 433 are in field galaxies and should be regarded as control sample.

We summarize observed properties of all the QSOs obtained in our study in Table 7.1. In the following sections, we attempt to find systematic differences between the properties of QSOs in the BCGs and those in field galaxies

Table 7.1: Summary of Observed Properties of Four Type 2 QSOs and One Type 1 QSO.

Source	Type[1]	location[2]	Redshift[3]	$N_{\rm H}$ ($10^{22}\,{\rm cm}^{-2}$)	EW (eV)	$L_{\rm X,2-10}$[4] ($10^{44}\,{\rm erg\,s}^{-1}$)	$L_{\rm X,10-50}$[5] ($10^{44}\,{\rm erg\,s}^{-1}$)	$\dot{M}_{\rm acc}$[6] ($M_\odot\,{\rm yr}^{-1}$)	$M_{\rm BH}$[7] ($M_\odot$)	$L_{\rm Edd}$[8] (%)	Ref.[9]
Phoenix cluster	2	BCG	0.596	32^{+9}_{-8}	149^{+139}_{-58}	47 ± 7	94^{+1}_{-2}	110	1.8×10^{10}	27	a
H 1821+643	1	BCG	0.297	< 0.01	82 ± 7	21.6 ± 0.2	32 ± 1	37	3.0×10^{9}	57	b, c
IRAS 09104+4109	2	BCG	0.442	29^{+58}_{-17}	539 ± 150	$5.1^{+0.4}_{-0.6}$	15^{+4}_{-7}	5	2.4×10^{9}	10	d
ESP 39607	2	field	0.201	28 ± 3	124^{+52}_{-31}	$4.7^{+0.1}_{-0.2}$	12^{+1}_{-2}	4.8	-	-	
3C 433	2	field	0.102	9.2 ± 0.6	57^{+30}_{-27}	1.2 ± 0.1	1.8 ± 0.2	0.7	-	-	

[1]: Classification of AGN.

[2]: Location of type 2 QSO.

[3]: Measured by McDonald et al. (2012), Pravdo & Marshall (1984), Kleinmann et al. (1988), Masetti et al. (2010), and Schmidt (1965) from top to bottom

[4]: X-ray luminosity in the $2-10\,$keV band.

[5]: X-ray luminosity in the $10-50\,$keV band.

[6]: Accretion rate.

[7]: Mass of SMBH.

[8]: Ratio of bolometric luminosity to Eddington luminosity.

[9]: References of mass of SMBHs (a: McDonald et al. (2012), b: Kolman et al. (1993), c: McGill et al. (2008), d: Piconcelli et al. (2007)).

7.2 EW $-$ $N_{\rm H}$ Relation of Type 2 QSOs

There found correlations between the EW of Fe I and the column density $N_{\rm H}$ for the power law component at least for nearby AGNs (e.g., Guainazzi et al. 2005; Fukazawa et al. 2011). The relation is characterized differently for $N_{\rm H} < 10^{23}\,{\rm cm}^{-}2$ and for $N_{\rm H} > 10^{23}\,{\rm cm}^{-}2$; the EW is almost constant for $N_{\rm H} < 10^{23}\,{\rm cm}^{-}2$, while the EW is roughly proportional to $N_{\rm H}$ for $N_{\rm H} > 10^{23}\,{\rm cm}^{-}2$. Proportionality between the EW and the $N_{\rm H}$ is expected if we assume a illuminating source surrounded by a sphere of a uniform density. On the other hand, the constant EW is expected for the reflection, i.e., an obscured source illuminating some optically thick matter. To realize both the relations in different regimes, a torus geometry is most plausible; we are observing X-rays through the torus and those reflected off the inner wall of the torus, as suggested by Ghisellini et al. (1994) and Krolik et al. (1994). Note that fluorescence iron K lines should be generated at the surface of accretion disk, though those should be broad and have unique profile called disk-line. We assume the Fe I line we observed are narrow and contribution from the disk-line is not significant, though it might not be valid for type 1 AGN, such as H 1821+643.

The EW of Fe I of four type 2 QSOs was determined to be 149^{+139}_{-60} eV, 539 ± 150 eV, 124^{+52}_{-31} eV, and 57^{+30}_{-27} eV, respectively. We plot these result overlaid with the data points derived by Fukazawa et al. (2011) for Seyfert galaxies, i.e., nearby radio-quiet AGNs observed with *Suzaku* in Figure 7.1.

As summarized in Table 7.1, we obtain the value of $N_{\rm H}$ as $3.2^{+0.9}_{-0.8} \times 10^{23}\,{\rm cm}^{-2}$, $2.9^{+5.8}_{-1.7} \times 10^{23}\,{\rm cm}^{-2}$, $(2.8 \pm 0.3) \times 10^{23}\,{\rm cm}^{-2}$, and $(9.2 \pm 0.6) \times 10^{22}\,{\rm cm}^{-2}$ for the Phoenix cluster, IRAS 09104+4109, ESP 39607, and 3C 433, respectively. The EW of Fe I of four type 2 QSOs was determined to be 149^{+139}_{-60} eV, $539 {\pm} 150$ eV, 124^{+52}_{-31} eV, and 57^{+30}_{-27} eV, respectively. We plot these result overlaid with the data points derived by Fukazawa et al. (2011) for AGNs in field observed with *Suzaku* in Figure 7.1.

The EW $-$ $N_{\rm H}$ relation for AGNs in field is consistent with what we mention above, which support the Fe I line is originated in the torus. The four data points based on our analysis of the type 2 QSOs are also on a similar trend to that for AGNs in field. This implies that torus geometry is also valid for our sample of the type 2 QSOs. There found no significant difference between the type 2 QSOs in the BCGs and those in filed galaxies.

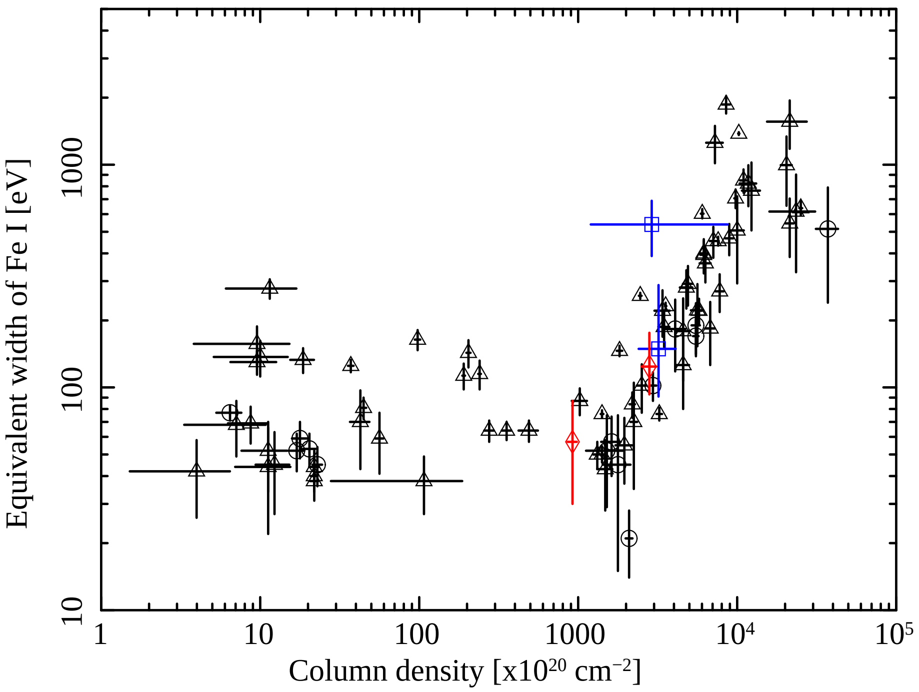

Figure 7.1: Relation of the EW of Fe I and the $N_{\rm H}$. The black triangles and circles are AGNs with X-ray luminosity in 10 − 50 keV ($L_{\rm X,10-50}$) of $L_{\rm X,10-50} < 10^{44}\,{\rm erg\,s^{-1}}$ and $L_{\rm X,10-50} > 10^{44}\,{\rm erg\,s^{-1}}$, respectively. The data are the same as Figure 5.6. The blue squares show the type 2 QSOs in the BCG of the Phoenix cluster and IRAS 09104+4109. The red diamonds show the type 2 QSOs in the field galaxy of ESP 39607 and 3C 433, respectively.

7.3 EW $-L_X$ relation and Type 2 Fraction for QSOs in BCGs

7.3.1 EW $-L_X$ Relation (the X-ray Baldwin Effect)

We next investigate the relation between the EW of Fe I and the X-ray luminosity. There found the X-ray Baldwin effect, anti-correlation between these two parameters. Figure 7.2 shows the relation between the EW of Fe I and the X-ray luminosity in the 10 − 50 keV band. We plot our results on four type 2 QSOs and one type 1 QSO overlaid with those of Seyfert galaxies derived by Fukazawa et al. (2011). The data points (red diamonds) of ESP 39607 and 3C 433 are also on the trend of the X-ray Baldwin effect of AGNs in field. On the contrary, the data points (blue squares) of the Phoenix cluster and IRAS 09104+4109 are offset in upward directions.

Figure 7.2 shows the relation between EW of Fe I and X-ray luminosity in the 10 − 50 keV band.

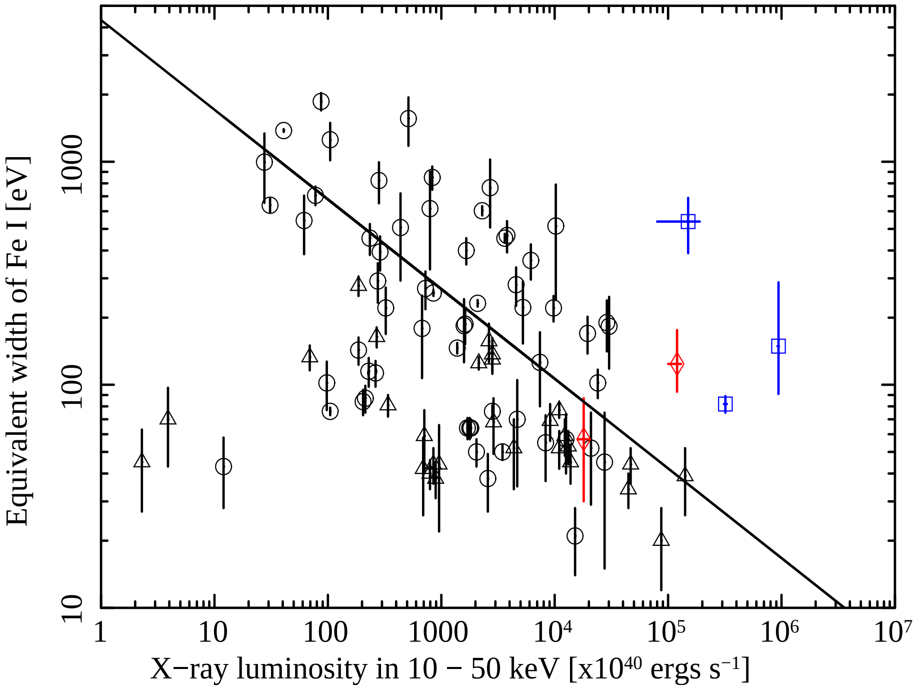

Figure 7.2: Relation between EW of Fe I and X-ray luminosity in the 10 − 50 keV band. The data are based on the bottom panel of Figure 7.1 but we put four bright field AGNs reported by Fukazawa et al. (2011) and the EW of H 1821+643 we obtained. Not only type 2 QSOs in the BCG but also type 1 QSO of H 1821+643 have the large EW of Fe I despite more luminous SMBH than field galaxies. The solid line describes the EW$-L_X$ relation from the fitting with the data of type 2 AGNs (black circles).

In order to perform statistical argument, we model the X-ray Baldwin effect. We adopt a simple power-law model for it. The parameters of the model are determined by fitting the data points of Type 2 AGNs (black circles in Figure 7.2) reported by Fukazawa et al. (2011). We obtain

$$\mathrm{EW} = 4300^{+2500}_{-2300} \times \left(\frac{L_{\rm X,10-50}}{10^{40}\,\mathrm{erg\,s^{-1}}}\right)^{-0.40^{+0.09}_{-0.10}} \quad \mathrm{eV}, \tag{7.1}$$

where $L_{\rm X,10-50}$ is the X-ray luminosity in $10-50\,\mathrm{keV}$. The goodness of fit is $\chi^2 = 7029$ for d.o.f. $= 57$, indicating that there are systematic errors larger than statistical errors by one order of magnitude.

These systematic errors are likely due to intrinsic variation of sources from the ideal relation assumed. Possible causes of the intrinsic variation in the EW for a given $L_{\rm X}$ includes the abundance of iron in the torus, the inclination, opening angle, and column density of the torus and so on. According to the simulation by Ikeda et al. (2009), the opening angle and inclination angle affects the EW by about factor of two.

We calculate the standard deviation of the data points of Type 2 AGNs in logarithmic space, that is $1\sigma_{\rm dex.} = 0.47\,\mathrm{dex}$. We use this value as the systematic error of our model, including a typical statistical error of the data. The uncertainties of parameters of the power-law model shown above are derived by taking this systematic errors into account.

We then examine the deviation of the EW (the most probable value) obtained by us from that expected with the model in the unit of $\sigma_{\rm dex.}$. The deviation is $+1.9\sigma_{\rm dex.}$, $+0.51\sigma_{\rm dex.}$, $+2.9\sigma_{\rm dex.}$ for the Phoenix cluster, H 1821+643, and IRAS 09104+4109, respectively. On the other hand, the deviation is $+0.53\sigma_{\rm dex.}$ and $-0.060\sigma_{\rm dex.}$ for ESP 39607and 3C 433, respectively. We summarize these values in Tab 7.3. The probability to obtain two sources out of three those that have deviations larger than $+1.9\sigma_{\rm dex.}$ and $+2.9\sigma_{\rm dex.}$ is 2×10^{-4}; we can reject the hypothesis that the the three QSOs in BCGs follow the same with a significance level of $\sim 0.02\,\%$. If we focus on the two QSOs in the Phoenix cluster and H 1821+643, we should refer the probability to obtain one source out of two those that has deviations larger than $+1.9\sigma_{\rm dex.}$, which is 6%.

We also perform a similar test with an alternative model of the X-ray Baldwin effect given by Ricci et al. (2013). They simulated the effect by assuming a torus geometry and a luminosity-dependent covering factor and succeeded in reproducing the observed EW$-L_{\rm X}$ relation obtained with *Chandra*/HETG by Shu et al. (2010), as we already showed in Figure 2.4. We calculate expected EW for each source in our sample by using the models provided by Ricci et al. (2013), one in which the column density $N_{\rm H}$ (along the equatorial plane of a torus) is assumed to be $10^{22.5}\,\mathrm{cm^{-2}}$ and the other in which that is assumed to be $10^{25}\,\mathrm{cm^{-2}}$. The results are listed in Table 7.2. We find the model with

$N_{\rm H} = 10^{22.5}\,{\rm cm}^{-2}$ underestimate the EW for all the five sources, and hence refer the model with $N_{\rm H} = 10^{25}\,{\rm cm}^{-2}$. We also assume the systematic error of the model is the same as that evaluated above. We then obtain the deviation of $+1.0\sigma_{\rm dex.}$, $+0.18\sigma_{\rm dex.}$, $+1.6\sigma_{\rm dex.}$ for the Phoenix cluster, H 1821+643, and IRAS 09104+4109, respectively. The deviation is $+0.099\sigma_{\rm dex.}$ and $-0.18\sigma_{\rm dex.}$ for ESP 39607and 3C 433, respectively. We summarize these values in Tab 7.3. The probability to obtain two sources out of three those that have deviations larger than $+1.0\sigma_{\rm dex.}$ and $+1.6\sigma_{\rm dex.}$ is $\sim 3\,\%$. The probability to obtain one source out of the two, the Phoenix cluster and H 1821+643, is 32 %.

Table 7.2: EW$-L_{\rm X}$ Relation from X-ray Observations and Expected EW from Simulations.

Name	Obs. EW (eV)	Exp. EW^1 (eV)	Exp. EW^2 (eV)	Exp. EW^3 (eV)
Phoenix cluster	149^{+139}_{-58}	17	1	31
H 1821+643	82 ± 7	26	2	42
IRAS 09104+4109	539 ± 150	36	5	73
ESP 39607	124^{+52}_{-31}	39	5	75
3C 433	57^{+30}_{-27}	84	10	111

^{1}: From Equation 7.1 based on the data of type 2 AGNs reported by Fukazawa et al. (2011).

^{2}: From simulations of quasar regime by Ricci et al. (2013) with the value of equatorial column density ($N_{\rm H}^{\rm T}$) as $N_{\rm H}^{\rm T} = 10^{22.5}\,{\rm cm}^{-2}$ but only that of Seyfert regime in the case of 3C 433.

^{3}: Same as Expected EW^2 but for the $N_{\rm H}^{\rm T} = 10^{25}\,{\rm cm}^{-2}$.

These statistical tests indicate that QSOs in the BCGs have significantly different EW$-L_{\rm X}$ relation than for nearby Type 2 AGNs plus type 2 QSOs in field galaxies, if we focus on the sample of three QSOs in the Phoenix cluster, H 1821+643, and IRAS 09104+4109. This difference is less significant if we limit the sample to the two QSOs selected from complete catalogues.

However, we have to consider various issues which may affect this results. Although we already have systematic error of the model taken into account, the models representing the X-ray Baldwin effect that we used above are based directly and indirectly on the observations of less luminous AGNs than ours. Therefore, the systematic error may be larger than for very luminous AGNs. Apparently we need larger sample especially that of very luminous AGNs in field galaxies before obtaining a firm conclusion.

Table 7.3: Significance of the Difference of the Observed EW from the Model Line.

Name	Obs. EW (eV)	Exp. EW[1] (eV)	Dev.[2] ($\sigma_{\mathrm{dex.}}$)	Exp. EW[3] (eV)	Dev.[4] ($\sigma_{\mathrm{dex.}}$)
Phoenix cluster	149^{+139}_{-58}	17	+1.9	31	+1.0
H 1821+643	82 ± 7	26	+0.51	42	+0.18
IRAS 09104+4109	539 ± 150	36	+2.9	73	+1.6
ESP 39607	124^{+52}_{-31}	39	+0.53	75	+0.099
3C 433	57^{+30}_{-27}	84	−0.060	111	−0.18

[1]: From Equation 7.1 based on the data of type 2 AGNs reported by Fukazawa et al. (2011).

[2]: Significance for the difference of observed EW from the model line (column 3).

[3]: From simulations of quasar regime by Ricci et al. (2013) with the value of equatorial column density ($N_{\mathrm{H}}^{\mathrm{T}}$) as $N_{\mathrm{H}}^{\mathrm{T}} = 10^{25}\,\mathrm{cm}^{-2}$ but only that of Seyfert regime in the case of 3C 433.

[4]: Same as column 4 but for $N_{\mathrm{H}}^{\mathrm{T}} = 10^{25}\,\mathrm{cm}^{-2}$ (column 5).

7.3.2 Type 2 Fraction and Opening Angle of a Torus

Type 2 fraction is defined as a fraction of the type 2 AGNs to type 1 plus 2 AGNs, as mentioned in Section 2.2.1. Hasinger (2008) showed that the type 2 fraction is smaller for higher luminosity and that for the X-ray luminosity $L_{\mathrm{X},2-10} \sim 2 \times 10^{45}\,\mathrm{erg\,s^{-1}}$, corresponding to our sample, is $\sim 10\,\%$. According to Burlon et al. (2011), the type 2 fraction with $L_{\mathrm{X}} > 10^{44}\,\mathrm{erg\,s^{-1}}$ in $15 - 55\,\mathrm{keV}$ is $\sim 20\,\%$. These values should be compared with the fact that one type 2 QSO, which in the Phoenix cluster, and one type 1 QSO, which in H 1821+643, are selected in our collation of the *Planck* SZ cluster catalogue with the *Swift*/BAT 70-Month catalogue in Chapter 5. The probability to obtain such pairs is 18 %, if the type 2 fraction is 10 %. We can little constrain the type 2 fraction of luminous AGNs in BCGs in clusters only with the two sources, as anticipated.

In the frame work of the AGN unification model (e.g., Antonucci 1993; Bianchi et al. 2012), the type 2 fraction should be determined by the opening angle of a torus. On this point, we note that the reflection fractions of the type 2 QSO in the Phoenix cluster and the type 1 QSO in H 1821+643 are $R = 0.77^{+0.48}_{-0.38}$ and $R = 0.80^{+0.06}_{-0.07}$, respectively. The reflection fraction is a fractional solid angle of the surrounding matter around a illuminating source, and thus should simply equal to the type 2 fraction. Therefore, the high reflection fractions we obtained is consistent with a larger type 2 fraction than expected for luminous AGNs in BCGs in clusters.

Overall, the EW$-L_{\mathrm{X}}$ relation, type 2 fraction, and reflection fraction of our sample of luminous AGNs in BCGs suggest that covering fraction is larger for those objects than expected. If we assume a tours, its opening angle can be smaller than expected in luminous AGNs in field galaxies. Although we apparently need larger sample, we discuss possible relations of this hypothesis with phenomenon in cluster scale, e.g., cooling flow, in the next section.

7.4 Cooling Flow, Star Formation, and Torus

We obtain the difference of the torus geometry (i.e., the opening angle) in the QSOs in the BCGs from those in the field galaxies. We assume that this difference is generated by mechanisms that function for only BCG. We discuss here the relation among cooling flow, star formation, and torus from the point of view of our assumption.

7.4.1 Time Scales of AGN feedback

As mentioned in Section 7.1, we find two clusters out of 861 samples, whose BCGs have luminous AGNs ($L_{\mathrm{X},14-195} > 10^{45}\,\mathrm{erg\,s^{-1}}$). Its fraction is 2/861 or 0.23 %.

Our results enable us to estimate a time scale of the AGN feedback of radiative mode. They indicate that the time scale is 23 Myr assuming that the age of clusters is 10 Gyr. In other words, the time scale of kinetic mode is estimated to be 9.977 Gyr, because the fraction of the others that their BCGs have no luminous AGNs is 859/861. We consider that their AGNs function the kinetic mode, i.e., they are in typical cool-core clusters.

7.4.2 Energy Transfer from SMBHs in BCGs

We discuss here the energy transfer from SMBHs in BCGs to the ICM, i.e., the AGN feedback, in the Phoenix cluster, H 1821+643, and IRAS 09104+4109. To evaluate the relation of the cooling flow and the AGN feedback of radiative mode and kinetic mode, we investigate the observational properties of clusters, BCGs, and tori by using the data of the Phoenix cluster, H 1821+643, and IRAS 09104+4109.

We summarize the observed properties of the QSOs in the Phoenix cluster, H 1821+643, and IRAS 09104+4109 involved the cooling flow and the AGN feedback in Table 7.4.

Table 7.4: Cooling Rate, Star Formation Rate, Accretion Rate, Radiative Heating Power, and Mechanical Power.

Component	Phoenix cluster	H 1821+643	IRAS 09104+4109
Cooling rate ($M_\odot\,\mathrm{yr}^{-1}$)	2300	300 (a)	235 (b)
Cooling radius (r_c) (kpc)	100	90	30
Mass within r_c ($10^{11} M_\odot$)	20	9.1	0.74
SFR ($M_\odot\,\mathrm{yr}^{-1}$)	798 (c)	13[1]	41 (d)
Accretion rate ($M_\odot\,\mathrm{yr}^{-1}$)	110	37	5
ϵ_cool[2] (%)	40	17	20
Mass of SMBH ($M_\odot$)	1.8×10^{10} (c)	3.0×10^{9} (e,f)	2.4×10^{9} (g)
Eddington ratio (%)	27	57	10
Radiative power[3] ($10^{43}\,\mathrm{erg\,s^{-1}}$)	67	8.6	0.9
Mechanical power[4] ($10^{43}\,\mathrm{erg\,s^{-1}}$)	-	$10 \sim 20$ (b)	528[5] (c)
Total radiative energy[6] (10^{61} erg) (w/ 23 Myr)	49E-3	6.2E-3	0.65E-3
Total mechanical energy[7] (10^{61} erg) (w/ 9.977 Gyr)	-	$24 \sim 47$	160
Total cooling energy (10^{61} erg)	200	73	7.4

[1]: Estimated by [O II] $\lambda3727$ reported by Kolman et al. (1991) using Kennicutt (1998) and Kewley et al. (2004).

[2]: Defined by (SFR + accretion rate) / cooling rate.

[3]: Estimated by Equation 7.2.

[4]: For example, cavities energy, jets energy.

[5]: Total of all cavities.

[6]: Assuming the time scale of 23 Myr.

[7]: Assuming the time scale of 9.977 Gyr.

(a): Russell et al. (2010), (b): O'Sullivan et al. (2012), (c): McDonald et al. (2012) and McDonald et al. (2013a), (d): Bildfell et al. (2008), (e): Kolman et al. (1993), (f): McGill et al. (2008), (g): Piconcelli et al. (2007)

First, the cooling rate of each cluster shown in Table 7.4 is estimated to be $\sim 2300\,M_\odot\,\mathrm{yr}^{-1}$ (Ueda et al. 2013a), $\sim 300\,M_\odot\,\mathrm{yr}^{-1}$ (Russell et al. 2010), and $\sim 235\,M_\odot\,\mathrm{yr}^{-1}$ (O'Sullivan et al. 2012) for the Phoenix cluster, H 1821+643, and IRAS 09104+4109, respectively. The cooling radius (r_c) and mass of the ICM within r_c for each cluster are referred to the same papers.

Next, the SFR in the BCG of the Phoenix cluster is measured by McDonald et al. (2013a) and that of IRAS 09104+4109 is obtained by Bildfell et al. (2008). In the case of H 1821+643, we estimate the SFR in its BCG to be $9.1\,M_\odot\,\mathrm{yr}^{-1}$ by using [O II] $\lambda3727$ (Kolman et al. 1991) with Kennicutt (1998) and Kewley et al. (2004).

The accretion rate of each SMBH is estimated by the X-ray luminosity obtained in this work. The mass of each SMBH is referred to McDonald et al. (2012), Kolman et al. (1993), McGill et al. (2008), and Piconcelli et al. (2007). The ϵ_cool represents the ratio defined by (SFR + accretion rate) / cooling rate.

The radiative power of the AGN in each BCG shown in Table 7.4 is estimated by

$$P_\mathrm{rad} = 1.25 \times 10^{44}\left(\frac{\tau}{0.01}\right)\left(\frac{f}{0.1}\right)\left(\frac{L_\mathrm{Bol}}{L_\mathrm{Edd}}\right)\left(\frac{M_\mathrm{BH}}{10^9\,M_\odot}\right)\ \mathrm{erg\,s^{-1}}, \tag{7.2}$$

where P_rad is the radiative power, τ is the opacity estimated by Equation 2.20, f is the fraction of the amount of available photons, L_Bol is the bolometric luminosity, and L_Edd is the Eddington luminosity. We assume that the f is 0.1 (10 %) mentioned in Siemiginowska et al. (2010). The total radiative energy represents the value that is integrated the radiative power during the time scale of AGN feedback of radiative mode, i.e., 23 Myr.

On the other hand, the mechanical power of each AGN is measured by Russell et al. (2010) for H 1821+643 and O'Sullivan et al. (2012) for IRAS 09104+4109. We summarize their results in Table 7.4. However, no measurement of the mechanical power is found for the AGN in the BCG of the Phoenix cluster. The total mechanical energy describes the value that is integrated the mechanical power during the time scale of AGN feedback of kinetic mode, i.e., 9.977 Gyr.

We estimate the total cooling energy by using the bolometric luminosity of the ICM in each cluster. They represent the energy that is integrated the luminosity of the ICM during the cooling time; the cooling time of the Phoenix cluster is 1.0 Gyr, that of H 1821+643 is 7.7 Gyr, and that of IRAS 09104+4109 is 1.0 Gyr.

The ϵ_cool, (SFR + accretion rate) / cooling rate, of three clusters is larger then 10 % (see Table 7.4), that is a typical value in nearby cool-core clusters (e.g., McDonald et al. 2011). The type 1 QSO of H 1821+643 and type 2 QSO of IRAS 09104+4109 have radio structures (i.e., jets) surrounding their BCGs (Russell et al. 2010; O'Sullivan et al. 2012). The mechanical powers in them are larger than the radiative heating power and required heating powers in their clusters, while we have no data of mechanical power in the Phoenix cluster.

In all cases of three clusters, the total radiative energy is many orders of magnitude smaller than the total cooling energy. For the Phoenix cluster, although it has the largest total radiative energy, the total radiative energy contributes only 0.01 % to balance the total cooling energy.

The total mechanical energy of IRAS 09104+4109 is two orders of magnitude larger than the total cooling energy. This result indicates that the heating overcomes the cooling. In the case of H 1821+643, the total mechanical energy is a factor of 2 smaller than the cooling energy. This results is suggested by Russell et al. (2010). They consider that some hidden cavities exist in this cluster to balance the cooling. We have no data of the mechanical energy in the Phoenix cluster. To discuss the balance of the heating to the cooling, we have to measure the mechanical power with radio observatory in the future.

In this work, we show that the radiative power of each QSO in the BCG does not contribute the heating. Moreover, the torus may block the radiation from the SMBH, i.e., the radiative power passed through the torus that is effective power to heat the ICM by radiation is smaller than that of the original power.

However, to generate the most powerful AGN feedback, McNamara et al. (2011) reported that the fueling of cold gas is required. However, the high accretion rate of three QSOs in the BCGs indicates an existence of a large amount of cooled gas near the SMBHs. Perhaps, it must be the torus. We will discuss this content in Section 7.4.3.

7.4.3 Mass Transfer from ICM

Changing the point of view, we discuss here the mass transfer from ICM to BCG, i.e., works of the cooling flow. Whereas, we do not have direct evidence of a presence of the cooling flow in three clusters.

We have already summarized the observed properties involved the mass transfer in Table 7.4. The SFRs of three BCGs are estimated to be 798 $M_\odot\,\mathrm{yr}^{-1}$, 9.1 $M_\odot\,\mathrm{yr}^{-1}$, and 41 $M_\odot\,\mathrm{yr}^{-1}$ for the Phoenix cluster, H 1821+643, and IRAS 09104+4109, respectively. We also estimate the accretion rates of three SMBHs to be 110 $M_\odot\,\mathrm{yr}^{-1}$, 37 $M_\odot\,\mathrm{yr}^{-1}$, and 5 $M_\odot\,\mathrm{yr}^{-1}$, respectively. Therefore, the ϵ_{cool} becomes 40 %, 17 %, and 20 %, respectively.

The ϵ_{cool} of each cluster is larger than that of typical cool-core cluster, i.e., 10 % (e.g., McDonald et al. 2011). The Phoenix cluster has the largest accretion rate in three clusters in this work, and it also has the largest ϵ_{cool} in three clusters. Although we have no idea to explain these reason, we consider that these results are a hint for understanding the fate of cooled gas from the ICM, i.e., the cooling flow.

Next, we estimate the mass of the torus. As described in Section 5.1.6, we obtain the mass of the torus of the type 2 QSO in the Phoenix cluster assuming a spherical ring with the inner radius of 0.9 pc and the column density of $3.2 \times 10^{23}\,\mathrm{cm}^{-2}$ (Ueda et al. 2013a). Although the estimated torus mass is largely dependent on the assumed outer radius, it is estimated to be $3.0 \times 10^4\,M_\odot$ $1.2 \times 10^6\,M_\odot$, and $1.1 \times 10^8\,M_\odot$ for the outer radius of 1 pc, 10 pc, and 100 pc, respectively (Ueda et al. 2013a). Burtscher et al. (2013) measure the outer radius of the torus of 23 AGNs including 3C 273. Although the radius with 300 K of several AGNs including 3C 273 is larger than 100 pc, all the mid-IR half-light radii are smaller than 10 pc (Burtscher et al. 2013). Therefore, we consider that the mass of the torus with the outer radius of 100 pc is the maximum value.

We apply this method to estimate the mass of the torus of the type 2 QSO in IRAS 09104+4109. When the inner radius is 0.4 pc and the column density is $2.9 \times 10^{23}\,\mathrm{cm}^{-2}$, the mass is estimated to be $1.5 \times 10^4\,M_\odot$, $1.0 \times 10^6\,M_\odot$, and $9.8 \times 10^7\,M_\odot$ for the outer radius of 1 pc, 10 pc, and 100 pc, respectively.

As mentioned above, we obtain that the time scale of AGN feedback of radiative mode is 23 Myr. Assuming that the accretion rates of both the type 2 QSOs are maintained continuously during 23 Myr, the masses of accreted gas onto the SMBHs reach $2.5 \times 10^9\,M_\odot$ for the Phoenix cluster and $1.2 \times 10^8\,M_\odot$ for IRAS 09104+4109. Both the masses are larger than the estimated masses of the tori with the outer radii of 100 pc.

This result indicates that a large amount of cold/cooled gas is required to maintain the accretion rate during the time scale of AGN feedback of radiative mode, when the gas accrete onto the SMBH through the torus. The cold/cooled gas should be supplied from the outside region of the torus. Furthermore, the cold/cooled gas is needed to keep the massive starburst in the BCG during at least 10^8 yr (e.g., Kennicutt 1998). We discuss as follows that a merger with member galaxies is one of the possibilities of the origin of the amount of required gas.

Following McDonald et al. (2013a), we estimate a number of required mergers with gas-rich galaxies. Corbelli et al. (2012) measure the cold gas mass of the galaxies in the Virgo cluster. According to Corbelli et al. (2012), the most gas-rich galaxy they measured has the cold gas of $\sim 5 \times 10^9\,M_\odot$. The required gas, i.e., the total mass of accreted gas onto the SMBH during 23 Myr and fuel of the starburst during 10^8 yr in the Phoenix cluster and IRAS 09104+4109, reaches $8 \times 10^{10}\,M_\odot$ and $4 \times 10^9\,M_\odot$, respectively. The amount of required gas for IRAS 09104+4109 is consistent with the mass of the cold gas in the gas-rich galaxy in the Virgo cluster. However, in the case of the Phoenix cluster, the amount of required gas is significantly larger than its.

On the contrary, the cooling flow enables to supply the required gas within 3.5×10^7 yr for the Phoenix cluster and 1.7×10^7 yr for IRAS 09104+4109. This time scale is roughly consistent with that of AGN feedback of radiative mode.

In the case of IRAS 09104+4109, we can explain that the origin of the amount of required gas is the gas-rich mergers. However, for the Phoenix cluster, the amount of required gas may be mainly supplied from the cooling flow. This statement has been already claimed by McDonald et al. (2013a). From this point of view, we consider the torus plays a role in a reservoir of the cooled gas to accrete onto the SMBH finally.

The latest studies of the central galaxy of clusters of galaxies are unveiling the existence of the cold gas (i.e., the molecular gas) of a few kpc scale around the SMBHs. For example, Fujita et al. (2013) and Hamer et al. (2014) discover a dust lane rotating around the AGN in Hydra A, the BCG of the Hydra cluster ($z = 0.055$). In the case of the Phoenix cluster, McDonald et al. (2013b) detect a molecular gas of $\sim 2 \times 10^{10}\, M_\odot$ in the BCG. Perhaps, these results support our assumption.

Figure 7.3 shows the mass (or energy) transfer from the ICM to the SMBH through the torus (with the cooling flow in this work) in the case of the Phoenix cluster based on Ueda et al. (2013a). We consider that a part of the cooled gas from the cooling flow transfers to the torus so that it accretes onto the SMBH. Several indirect evidence show its concept. In fact, to maintain the starburst and the torus, a large amount of cooled gas is required. When this system is maintained in steady-state, the BCG need a total mass of cooled gas of $\sim 900\, M_\odot\, \mathrm{yr}^{-1}$ at least during 10^7 yr.

Figure 7.4 shows a sketch of a distance from an SMBH in the BCG and a scale of each region. Simultaneously, we denote the energy flow around SMBH in Figure 7.4. In previous studies, the cooling flow reaches the star-forming region (see Figure 7.4). In this work, we suggest that a part of the cooled gas to maintain the torus is supplied from the cooling flow.

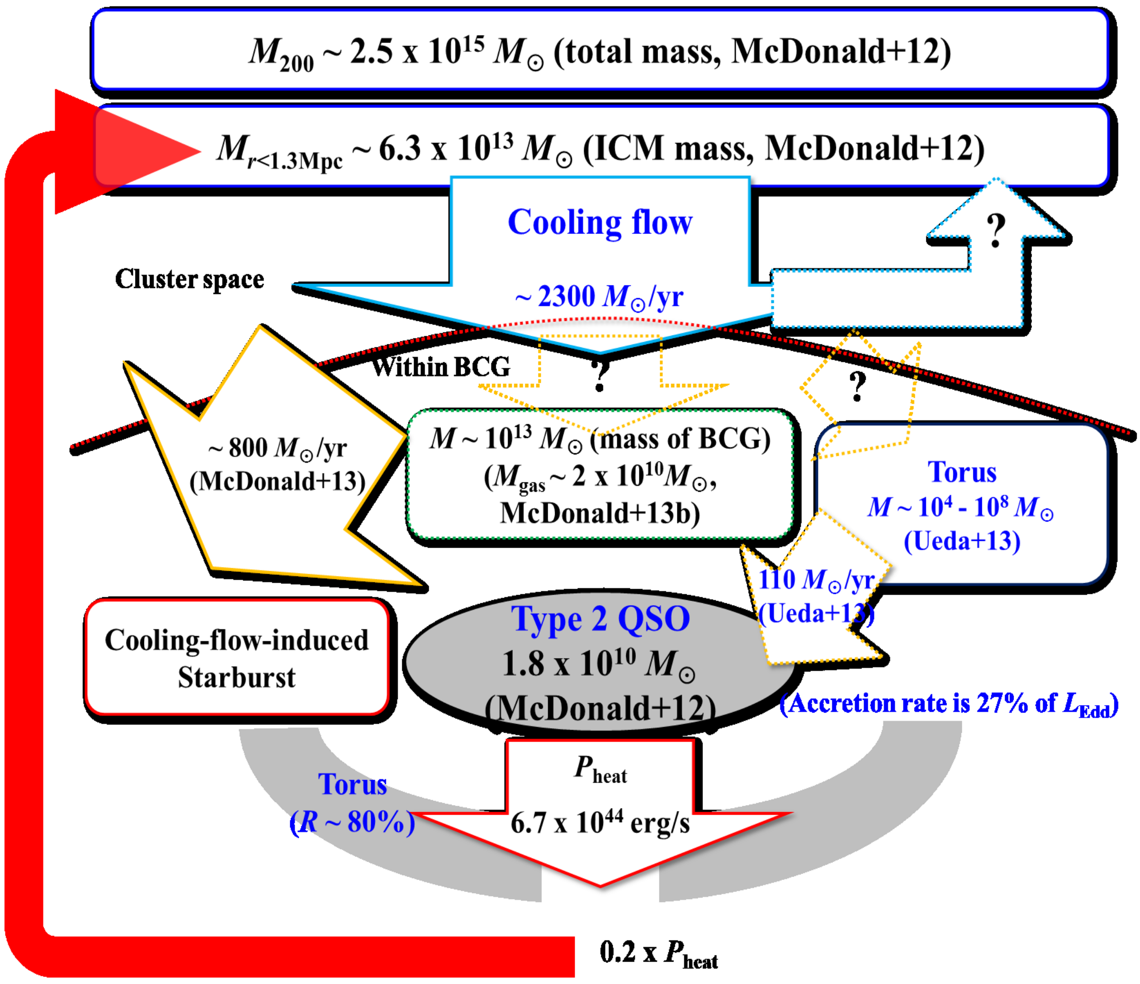

Figure 7.3: Mass (energy) transfer from the ICM to the SMBH and from the SMBH to the ICM in the Phoenix cluster.

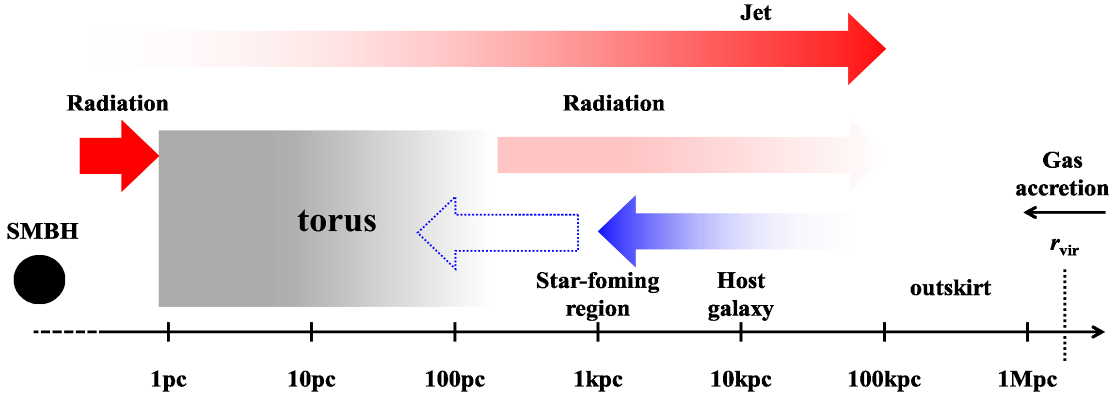

Figure 7.4: Distance from an SMBH in the BCG, a scale of each region, and an energy transportation.

7.5 Future Prospects

We list future prospects to develop our study.

1. Find more samples that clusters have luminous AGNs in their BCGs to study the EW $-L_{\mathrm{X}}$ relation and the type 2 fraction for AGNs in BCGs.
2. Radio observations of the Phoenix cluster to measure mechanical powers and to evaluate molecular gas in its BCG.
3. Search for the Fe I line from BCGs in nearby cool-core clusters and measurement of its EW.
4. Theoretical study to understand the mass transfer from ICM to SMBH.

First statement is the simplest idea to extend our study. By referring both the updated *Planck* SZ cluster catalogue and *Swift* hard X-ray source catalogue, we can search for the samples easily with our method.

Second one is to fully understand the energy transfer from the SMBH to the ICM. It is important to reveal the balance of the heating to the cooling.

Third one is new point of view to study the evolution of SMBHs (and tori) in nearby cool-core clusters. We have to investigate an existence of the torus in AGN with kinetic mode. Since ASTRO-H (Takahashi et al. 2012) has a performance to detect the Fe I line from SMBHs in nearby coo-core cluster, we can study it with ASTRO-H.

Final one is a point of view from the theoretical study. Some researchers start to this study with numerical simulations (e.g., Li & Bryan 2012; Gaspari et al. 2013; Li & Bryan 2013, 2014; Guo & Mathews 2014). However, the contribution of the torus is not considered in their works. Since we show in this work that the torus may play a role in a reservoir of cooled gas, we hope to include observational indication of our works.

7.5.1 Why Did IRAS 09104+4109 Go the Missing Cluster?

IRAS 09104+4109 is not included in the *Planck* SZ cluster catalogue and the *Swift*/BAT 70-Month catalogue. We discuss why IRAS 09104+4109 is not included in them.

A sensitivity of *Planck* for SZ clusters is roughly $(0.1-1.0)\times10^{15}\,M_{\odot}$ within r_{500} but with the redshift dependence. Figure 7.5 shows the sensitivity limit of *Planck* survey at each redshift. At the redshift of $z = 0.442$ corresponding to that of IRAS 09104+4109, the sensitivities of *Planck* are over $0.4\times10^{15}\,M_{\odot}$ for the deep survey area covering 2.7 % of the sky, over $0.5\times10^{15}\,M_{\odot}$ for the medium-deep survey area covering 41.3 % of the sky, and over $0.6 \times 10^{14}\,M_\odot$ for the shallow survey are covering 56 % of the sky, respectively (Planck Collaboration et al. 2014). The total mass of IRAS 09104+4109 within r_{500} is estimated to be $(5.83 \pm 1.69) \times 10^{14}\,M_\odot$ (O'Sullivan et al. 2012), which is equivalent to the sensitivities of *Planck* at the redshift of $z = 0.442$. Therefore, it is possible that *Planck* survey did not find the SZ effect of IRAS 09104+4109 significantly.

On the other hand, a flux sensitivity of *Swift* is $1.34 \times 10^{-11}\,\mathrm{erg\,s^{-1}\,cm^{-2}}$ in the $14 - 195$ keV band covering 90 % of the sky (Baumgartner et al. 2013). Figure 7.6 shows the 5σ sensitivity limit of *Swift* survey. We estimate a flux of the type 2 QSO in IRAS 09104+4109 with the parameters obtained in Section 6.3. Thus, we obtain the upper limit of the flux to be $1.37 \times 10^{-11}\,\mathrm{erg\,s^{-1}\,cm^{-2}}$ in the $14 - 195$ keV band, which is consistent with the flux sensitivity of *Swift*.

Therefore, IRAS 09104+4109 and the type 2 QSO in its BCG may fall below the sensitivities of each satellite. If the *Planck* team and the *Swift*/BAT team release new catalogue in the future, we will be able to add in the samples of luminous AGNs in BCGs.

7.5.2 Future X-ray Observatory Missions

To verify one of our assumption, i.e., type 2 fraction for QSOs in BCGs is larger than that for AGNs in field, we have to search for more samples of such clusters. However, perhaps, as mentioned by (Urry & Treister 2007; Treister & Urry 2012), the type 2 fraction in previous study (e.g., Hasinger 2008) is affected by the selection biases. The type 2 fraction for QSOs in BCGs we obtained is may be well-described for "true" type 2 fraction in the Universe.

A hard X-ray survey is one method hardly affected by the selection bias. Because we can detect heavily obscured AGNs (Compton thick AGNs) directly. In particular, the thermal emission from ICM pollutes the emission from AGNs in BCGs in soft X-ray band.

Since *Swift* is kept observing, it is likely possible that we obtain updated data of hard X-ray source in the all-sky, i.e., new candidates of luminous AGNs in the BCGs. On the other hand, new hard X-ray observatory (e.g., *NuSTAR*; Harrison et al. 2013) may play a powerful role in the hard X-ray survey. *NuSTAR* has a factor of 100 higher sensitivities than that of *Swift*. Moreover, the observable energy range of *NuSTAR* is $3 - 80$ keV (Harrison et al. 2013). However, the energy resolution of hard X-ray detectors onboard *NuSTAR* is about 2 times worse than that of X-ray CCD at 10 keV (Harrison et al. 2013). Then, it is difficult to resolve lines of Fe I, Fe XXV, and Fe XXVI.

ASTRO-H X-ray observatory (Takahashi et al. 2012) is likely the most powerful X-ray observatory to reveal X-ray natures of AGNs and clusters. The Hard X-ray Imager (HXI; Kokubun et al. 2012) onboard ASTRO-H shows similar performances of *NuSTAR*.

Furthermore, the Soft X-ray Spectrometer (SXS; Mitsuda et al. 2010) has a performance of X-ray high resolution spectroscopy of several eV at 6 keV. Combining the HXI with the SXS, we will be able to measure the EW of Fe I and X-ray luminosity in the hard X-ray band simultaneously and accurately even if the AGNs are embedded in the central galaxies of clusters.

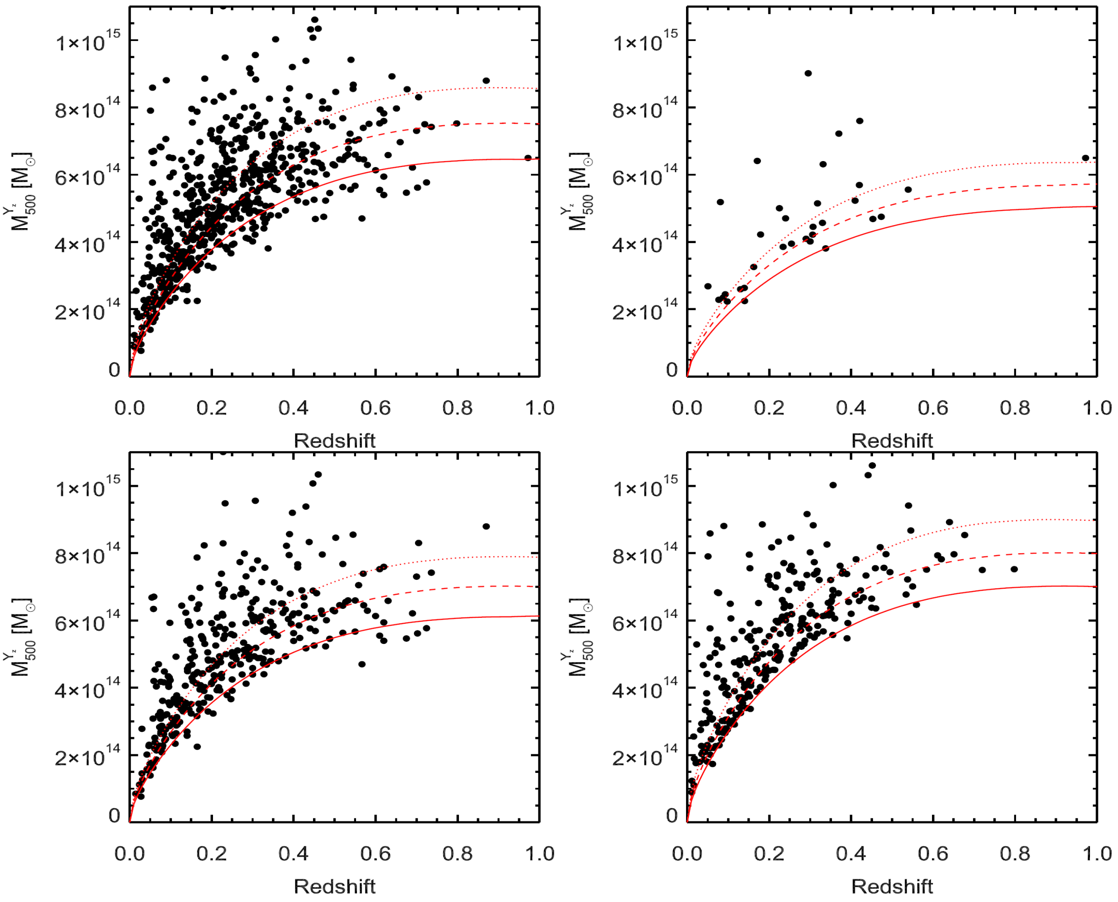

Figure 7.5: Sensitivity limits of the *Planck* SZ cluster catalogue (Figure 28 of Planck Collaboration et al. 2014). Upper left: average mass limit computed from the average noise over the sky. Upper right: same for the deep survey zone corresponding to 2.7 % sky coverage centred at the Ecliptic polar regions. Lower left: same for the medium-deep survey area covering 41.3 % of the sky. Lower right: same for the shallow-survey area covering 56 % of the sky. In each panel, only detections in the corresponding areas are plotted. The lines dotted, dashed and solid lines show the Planck mass limit at 80, 50 and 20 % completeness, respectively (Planck Collaboration et al. 2014). Reproduced with permission, Dr. Nabila Aghanim (Planck Collaboration et al. 2014), private communication.

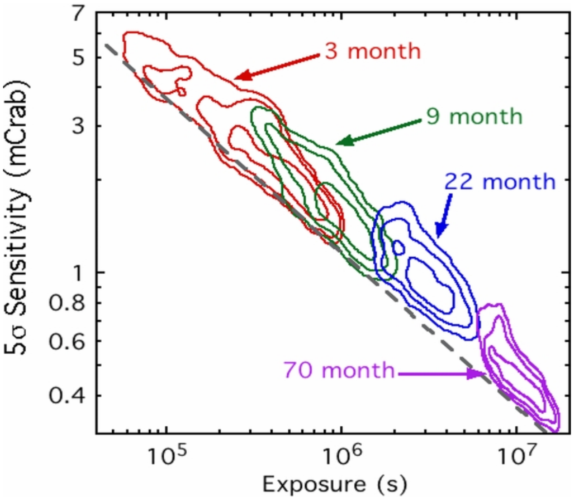

Figure 7.6: Measured 5σ *Swift*/BAT sensitivity limit for pixels in the all-sky map as a function of effective exposure time, T, for the 3 month (red; Markwardt et al. 2005)), 9 month (green; Tueller et al. 2008), 22 month (blue; Tueller et al. 2010), and 70 month (purple; Baumgartner et al. 2013) survey analyses. The contours are linearly spaced and indicate the number of pixels with a given sensitivity and effective exposure. The black dashed line represents a lower limit to the expected Poisson noise level (Baumgartner et al. 2013). The median achieved sensitivity is within 13 % of the predicted value. ©AAS. Reproduced with permission.

Chapter 8

Summary

We summarize the results obtained in this work.

Our aim is to investigate whether or not there are significant differences in the properties of the luminous SMBHs in the BCGs from those in field galaxies. By referring both the *Planck* SZ cluster catalogue and the *Swift*/BAT 70-Month catalogue, we search for clusters including such BCGs. Thus, we find two clusters out of 861 clusters sample, which have luminous AGNs in their BCGs with X-ray luminosities of $1 \times 10^{45}\,\mathrm{erg\,s^{-1}}$ in the $14 - 195\,\mathrm{keV}$ band. One is the Phoenix cluster ($z = 0.596$), and the other is H 1821+643 ($z = 0.297$).

We detect the Fe I line from both AGNs with the *Suzaku*/XIS. The EW of Fe I is 149^{+139}_{-58} eV and 82 ± 7 eV, respectively. The Fe I line indicates that a large amount of cold gas, i.e., the torus, surrounds the luminous SMBH. In particular, we measure that the column density (N_{H}) of the torus of the AGNs in the Phoenix cluster is $3.2^{+0.9}_{-0.8} \times 10^{23}\,\mathrm{cm^{-2}}$, meaning that it is heavily obscured. On the other hand, we obtain that the value of N_{H} of that in H 1821+643 is below $1 \times 10^{20}\,\mathrm{cm^{-2}}$. We classify the AGNs in the Phoenix cluster and H 1821+643 as the type 2 QSO and the type 1 QSO with X-ray observations of the *Suzaku*/XIS & HXD, respectively.

We also analyze other three type 2 QSOs to investigate the difference. One exists in the BCG of IRAS 09104+4109 ($z = 0.442$), which is not included in both catalogues but the mass of the cluster and the X-ray luminosity of its AGN are below the sensitivity limit of the surveys each other. The others are in the field galaxies of ESP 39607 ($z = 0.201$) and 3C 433 ($z = 0.102$). With the *Suzaku*/XIS & HXD, we identify that they are heavily obscured and luminous AGNs; the value of N_{H} as the type 2 QSO in IRAS 09104+4109 is $2.9^{+5.8}_{-1.7} \times 10^{23}\,\mathrm{cm^{-2}}$, that of ESP 39607 is $(2.8 \pm 0.3) \times 10^{23}\,\mathrm{cm^{-2}}$, and that of 3C 433 is $(9.2 \pm 0.6) \times 10^{22}\,\mathrm{cm^{-2}}$. The EW of Fe I of each type 2 QSO is 539 ± 150 eV, 124^{+52}_{-31} eV, and 57^{+30}_{-27} eV, respectively.

For our purpose, by using four type 2 QSOs and one type 1 QSO, we investigate the difference between QSOs in the BCGs and those in field galaxies. We also examine the AGN feedback of radiative mode and the cooling flow by using the observed properties of the Phoenix cluster, H 1821+643, and IRAS 09104+4109.

We first focus on the environment of the SMBHs with four type 2 QSOs. The relation of the N_{H} and EW indicates that the origin of the Fe I is the torus. We find that no significant difference of this relation for four type 2 QSOs from that obtained from field galaxies. Therefore, we suggest that the torus geometry of four type 2 QSOs is similar to that obtained from field galaxies even if the type 2 QSO are in the BCG.

We then investigate the EW $-L_{\mathrm{X}}$ relation. X-ray observations showed that the EW of Fe I is anti-correlated with the X-ray luminosity, which is called the X-ray Baldwin effect.

Since there are some causes to deviate the data points from the trend, we evaluate the fluctuations by using a total of 59 type 2 AGNs in field. We estimate that the standard deviation of the fluctuations is $1\sigma_{\mathrm{dex.}} = 0.47\,\mathrm{dex}$. Thus, the difference of the data from the model line for the Phoenix cluster is estimated to be $1.9\sigma_{\mathrm{dex.}}$ significance. Similarly, those of each QSO are estimated to be $0.51\sigma_{\mathrm{dex.}}$, $2.9\sigma_{\mathrm{dex.}}$, and $0.30\sigma_{\mathrm{dex.}}$ significance for H 1821+643 and IRAS 09104+4109, respectively. The probability to obtain two sources out of three those that have deviations larger than $+1.9\sigma_{\mathrm{dex.}}$ and $+2.9\sigma_{\mathrm{dex.}}$ is 2×10^{-4}; we can reject the hypothesis that the the three QSOs in BCGs follow the same with a significance level of $\sim 0.02\,\%$. If we focus on the two QSOs in the Phoenix cluster and H 1821+643, we should refer the probability to obtain one source out of two those that has deviations larger than $+1.9\sigma_{\mathrm{dex.}}$, which is 6%.

From the point of view of the type 2 fraction, we also investigate the difference between the QSOs in the BCGs and those in field galaxies. By referring both the *Planck* SZ cluster catalogue and the *Swift*/BAT 70-Month catalogue, we find one type 1 QSO and one type 2 QSO, meaning that the type 2 fraction is 50 %. On the contrary, we measure the reflection fraction of them (i.e., the covering factor). We obtain that the mean values of the covering factor is $0.79^{+0.48}_{-0.39}$, which indicates that the type 2 fraction for QSOs in BCGs is expected to be 80 % (at least over 40 %). Since it is estimated to be $10 - 20\,\%$ that is the type 2 fraction for AGNs in field on the same X-ray luminosity as the Phoenix cluster and H 1821+643, the type 2 fraction for QSOs in BCGs obtained by us is larger than that obtained by previous studies. Whereas, we have only two samples such QSOs. We need more samples to determine whether or not the type 2 fraction for QSOs in BCGs is larger than that for field galaxies.

Overall, the EW$-L_{\mathrm{X}}$ relation, type 2 fraction, and reflection fraction of our sample of luminous AGNs in the BCGs suggest that covering factor is larger for those objects than than expected. If we assume a tours, its opening angle can be smaller than that expected in luminous AGNs in field galaxies.

We discuss the AGN feedback of radiative mode in the cluster including luminous AGN in its BCG. We find two samples of such a cluster out of 861 clusters. Assuming that the cluster age is 10 Gyr, we can estimate the time scale of the AGN feedback of radiative mode to be 23 Myr. We quantitatively obtain the time scale, for the first time.

To evaluate the effect of radiation heating, we evaluate the heating and cooling energy of three clusters. The total radiative energies in the Phoenix cluster, H 1821+643, and IRAS 09104+4109 are many orders of magnitude smaller than the total cooling energy of each cluster estimated by the bolometric luminosity of the ICM. The total mechanical energy in IRAS 09104+4109 overcomes the total cooling energy of the ICM, while the total mechanical energy in H 1821+643 is about a factor of 2 smaller than the total cooling energy of the its ICM. Since we have no data of the total mechanical energy in the Phoenix cluster, we can not discuss the balance of the heating to the cooing in the Phoenix cluster.

We estimate the mass of the torus in the Phoenix cluster and IRAS 09104+4109 to be $1.1 \times 10^8\,M_\odot$ and $9.8 \times 10^7\,M_\odot$ for the outer radius of 100 pc, respectively. If both SMBHs keep constant accretion rate during 23 Myr, the total accretion masses are estimated to be $2.5 \times 10^9\,M_\odot$ and $1.2 \times 10^8\,M_\odot$, respectively, which are larger than those of the tori. To maintain the mass of the torus, some mechanisms need to supply the cold gas. The cooling flow may supply the cooled gas and then the torus may play a role in a reservoir of cooled gas.

Our work is the first step to verify the co-evolution among cluster, BCG, and SMBH. In order to reveal it, we have to search for such clusters and QSOs. The future work of *Swift* and several high quality hard X-ray surveys (e.g., *NuSTAR* and ASTRO-H but they do not perform the all-sky survey) may discover new candidates. In particular, ASTRO-H will perform the high resolution spectroscopy with the SXS, which may detect the Fe I line from QSOs in AGNs in BCGs in nearby cool-core cluster.

Acknowledgment

First of all, I appreciate to Prof. Hiroshi Tsunemi for his continuous and strong guidances, supports, and encouragements in my Ph.D. course. Thank you very much!!

Next, I am grateful to Dr. Hayashida and Dr. Koyama for strong guidances and supports. Especially, I have many thanks to Dr. Hayashida.

I appreciate to Dr. Anabuki, Dr. Nakajima, Dr. Nagino, and Dr. Takahashi for their supports. I also appreciate to the member of Kaiseki meeting. Especially I have many thanks for Dr. Mori, Dr. Katsuda, and Dr. Uchida. I thank to the member of Tsunemi Lab especially for the member of F 520. I also thank to Mrs. Hashimoto and Mrs. Sawamoto for advices of office works, who are the secretaries of Tsunemi Lab.

Finally, I am deeply grateful to support from all the people in Osaka University and my family. I also thank to encouragements from Mr. Kitayama, Mr. Kamitsukasa, and Mr. Deguchi. We are the member of Shojikkenshitsu. During a certain period of time in my master course, I was supported by Mr. Shuku.

Thanks God, it's 4 AM!

References

Abell, G. O. 1958, ApJS, 3, 211

Abell, G. O., Corwin, Jr., H. G., & Olowin, R. P. 1989, ApJS, 70, 1

Ajello, M., Rebusco, P., Cappelluti, N., et al. 2010, ApJ, 725, 1688

—. 2009, ApJ, 690, 367

Akylas, A., Georgantopoulos, I., Georgakakis, A., Kitsionas, S., & Hatziminaoglou, E. 2006, A&A, 459, 693

Allen, C. W. 1973, Astrophysical quantities (Athlone Press)

Anders, E., & Grevesse, N. 1989, Geochim. Cosmochim. Acta, 53, 197

Angulo, R. E., Springel, V., White, S. D. M., et al. 2012, MNRAS, 425, 2722

Antonucci, R. 1993, ARA&A, 31, 473

Antonucci, R. R. J., & Miller, J. S. 1985, ApJ, 297, 621

Arnaud, K. A. 1996, in Astronomical Society of the Pacific Conference Series, Vol. 101, Astronomical Data Analysis Software and Systems V, ed. G. H. Jacoby & J. Barnes, 17

Awaki, H., Koyama, K., Inoue, H., & Halpern, J. P. 1991a, PASJ, 43, 195

Awaki, H., Koyama, K., Kunieda, H., & Tawara, Y. 1990, Nature, 346, 544

Awaki, H., Kunieda, H., Tawara, Y., & Koyama, K. 1991b, PASJ, 43, L37

Bahcall, J. N., & Sarazin, C. L. 1978, ApJ, 219, 781

Baldi, A., Ettori, S., Mazzotta, P., Tozzi, P., & Borgani, S. 2007, ApJ, 666, 835

Baldwin, J. A. 1977, ApJ, 214, 679

Ball, R., Burns, J. O., & Loken, C. 1993, AJ, 105, 53

Bambynek, W., Crasemann, B., Fink, R. W., et al. 1972, Reviews of Modern Physics, 44, 716

Barbosa, D., Bartlett, J. G., Blanchard, A., & Oukbir, J. 1996, A&A, 314, 13

Barger, A. J., Cowie, L. L., Mushotzky, R. F., et al. 2005, AJ, 129, 578

Barrena, R., Girardi, M., & Boschin, W. 2013, MNRAS, 430, 3453

Barthelmy, S. D., Barbier, L. M., Cummings, J. R., et al. 2005, Space Sci. Rev., 120, 143

Baumgartner, W. H., Tueller, J., Markwardt, C. B., et al. 2013, ApJS, 207, 19

Beckmann, V., & Shrader, C. 2012a, in Proceedings of "An INTEGRAL view of the high-energy sky (the first 10 years)" - 9th INTEGRAL Workshop and celebration of the 10th anniversary of the launch (INTEGRAL 2012). 15-19 October 2012. Bibliotheque Nationale de France, Paris, France. Published online at http://pos.sissa.it/cgi-bin/reader/conf.cgi?confid=176, id.69

Beckmann, V., & Shrader, C. R. 2012b, Active Galactic Nuclei (Wiley-VCH Verlag GmbH & Co. KGaA)

Bianchi, S., Guainazzi, M., Matt, G., & Fonseca Bonilla, N. 2007, A&A, 467, L19

Bianchi, S., Maiolino, R., & Risaliti, G. 2012, Advances in Astronomy, 2012

Bildfell, C., Hoekstra, H., Babul, A., & Mahdavi, A. 2008, MNRAS, 389, 1637

Bîrzan, L., Rafferty, D. A., McNamara, B. R., Wise, M. W., & Nulsen, P. E. J. 2004, ApJ, 607, 800

Black, A. R. S., Baum, S. A., Leahy, J. P., et al. 1992, MNRAS, 256, 186

Blandford, R. D., & McKee, C. F. 1982, ApJ, 255, 419

Blanton, E. L., Sarazin, C. L., & McNamara, B. R. 2003, ApJ, 585, 227

Blundell, K. M., & Rawlings, S. 2001, ApJ, 562, L5

Boella, G., Butler, R. C., Perola, G. C., et al. 1997, A&AS, 122, 299

Böhringer, H., Matsushita, K., Churazov, E., Ikebe, Y., & Chen, Y. 2002, A&A, 382, 804

Boldt, E. 1987, Phys. Rep., 146, 215

Boldt, E., McDonald, F. B., Riegler, G., & Serlemitsos, P. 1966, Physical Review Letters, 17, 447

Brandt, W. N., & Hasinger, G. 2005, ARA&A, 43, 827

Branduardi-Raymont, G., Fabricant, D., Feigelson, E., et al. 1981, ApJ, 248, 55

Brinkman, A. C., Gunsing, C. J. T., Kaastra, J. S., et al. 2000, ApJ, 530, L111

Burbidge, G. 1967, Quasi-stellar objects (W.H.Freeman)

Burbidge, G. R., & Burbidge, M. 1966, Nature, 210, 774

Burke, B. E., Gregory, J. A., Bautz, M. W., et al. 1997, IEEE Transactions on Electron Devices, 44, 1633

Burlon, D., Ajello, M., Greiner, J., et al. 2011, ApJ, 728, 58

Burtscher, L., Meisenheimer, K., Tristram, K. R. W., et al. 2013, A&A, 558, A149

Canizares, C. R., Davis, J. E., Dewey, D., et al. 2005, PASP, 117, 1144

Carilli, C. L., Perley, R. A., & Harris, D. E. 1994, MNRAS, 270, 173

Chiang, C.-Y., Cackett, E. M., Gandhi, P., & Fabian, A. C. 2013, MNRAS, 430, 2943

Corbelli, E., Bianchi, S., Cortese, L., et al. 2012, A&A, 542, A32

Cowie, L. L., & Binney, J. 1977, ApJ, 215, 723

Crawford, C. S., & Vanderriest, C. 1996, MNRAS, 283, 1003

Cusumano, G., La Parola, V., Segreto, A., et al. 2010a, A&A, 510, A48

—. 2010b, A&A, 524, A64

Czerny, B., Nikołajuk, M., Piasecki, M., & Kuraszkiewicz, J. 2001, MNRAS, 325, 865

David, L. P., Jones, C., & Forman, W. 1995, ApJ, 445, 578

De Lucia, G., & Blaizot, J. 2007, MNRAS, 375, 2

den Herder, J. W., Brinkman, A. C., Kahn, S. M., et al. 2001, A&A, 365, L7

Dunn, R. J. H., & Fabian, A. C. 2004, MNRAS, 355, 862

Dunn, R. J. H., Fabian, A. C., & Taylor, G. B. 2005, MNRAS, 364, 1343

Edge, A. C. 2001, MNRAS, 328, 762

Einstein, A. 1936, Science, 84, 506

Elvis, M., Maccacaro, T., Wilson, A. S., et al. 1978, MNRAS, 183, 129

Ettori, S. 2000, MNRAS, 318, 1041

Fabian, A. C. 1994, ARA&A, 32, 277

Fabian, A. C. 2003, in Revista Mexicana de Astronomia y Astrofisica Conference Series, Vol. 17, Revista Mexicana de Astronomia y Astrofisica Conference Series, ed. V. Avila-Reese, C. Firmani, C. S. Frenk, & C. Allen, 303–313

—. 2012, ARA&A, 50, 455

Fabian, A. C., & Crawford, C. S. 1990, MNRAS, 247, 439

—. 1995, MNRAS, 274, L63

Fabian, A. C., Hu, E. M., Cowie, L. L., & Grindlay, J. 1981, ApJ, 248, 47

Fabian, A. C., & Nulsen, P. E. J. 1977, MNRAS, 180, 479

Fabian, A. C., Sanders, J. S., Ettori, S., et al. 2000, MNRAS, 318, L65

Fanaroff, B. L., & Riley, J. M. 1974, MNRAS, 167, 31P

Fang, T., Davis, D. S., Lee, J. C., et al. 2002, ApJ, 565, 86

Felten, J. E., Gould, R. J., Stein, W. A., & Woolf, N. J. 1966, ApJ, 146, 955

Ferrarese, L., & Merritt, D. 2000, ApJ, 539, L9

Forman, W., Kellogg, E., Gursky, H., Tananbaum, H., & Giacconi, R. 1972, ApJ, 178, 309

Foster, A. R., Ji, L., Smith, R. K., & Brickhouse, N. S. 2012, ApJ, 756, 128

Fujita, Y., Ohira, Y., & Yamazaki, R. 2013, ApJ, 767, L4

Fujita, Y., Tawa, N., Hayashida, K., et al. 2008, PASJ, 60, 343

Fukazawa, Y., Mizuno, T., Watanabe, S., et al. 2009, PASJ, 61, 17

Fukazawa, Y., Hiragi, K., Mizuno, M., et al. 2011, ApJ, 727, 19

Garmire, G. P., Bautz, M. W., Ford, P. G., Nousek, J. A., & Ricker, Jr., G. R. 2003, in Society of Photo-Optical Instrumentation Engineers (SPIE) Conference Series, Vol. 4851, Society of Photo-Optical Instrumentation Engineers (SPIE) Conference Series, ed. J. E. Truemper & H. D. Tananbaum, 28–44

Gaspari, M., Ruszkowski, M., & Oh, S. P. 2013, MNRAS, 432, 3401

Gawroński, M. P., Marecki, A., Kunert-Bajraszewska, M., & Kus, A. J. 2006, A&A, 447, 63

Gebhardt, K., Bender, R., Bower, G., et al. 2000, ApJ, 539, L13

Gehrels, N., & Williams, E. D. 1993, ApJ, 418, L25

Gehrels, N., Chincarini, G., Giommi, P., et al. 2004, ApJ, 611, 1005

Ghisellini, G., Haardt, F., & Matt, G. 1994, MNRAS, 267, 743

Giacconi, R., Gursky, H., Paolini, F. R., & Rossi, B. B. 1962, Physical Review Letters, 9, 439

Giacconi, R., Kellogg, E., Gorenstein, P., Gursky, H., & Tananbaum, H. 1971, ApJ, 165, L27

Giacconi, R., Branduardi, G., Briel, U., et al. 1979, ApJ, 230, 540

Gilli, R., Comastri, A., & Hasinger, G. 2007, A&A, 463, 79

Gopal-Krishna, & Wiita, P. J. 2000, A&A, 363, 507

Gorenstein, P., Fabricant, D., Topka, K., & Harnden, Jr., F. R. 1979, ApJ, 230, 26

Gorenstein, P., Fabricant, D., Topka, K., Harnden, Jr., F. R., & Tucker, W. H. 1978, ApJ, 224, 718

Gorenstein, P., Fabricant, D., Topka, K., Tucker, W., & Harnden, Jr., F. R. 1977, ApJ, 216, L95

Graham, A. W., & Scott, N. 2013, ApJ, 764, 151

Grossman, S. A., & Narayan, R. 1988, ApJ, 324, L37

—. 1989, ApJ, 344, 637

Gruber, D. E., Matteson, J. L., Peterson, L. E., & Jung, G. V. 1999, ApJ, 520, 124

Guainazzi, M., Matt, G., & Perola, G. C. 2005, A&A, 444, 119

Gültekin, K., Richstone, D. O., Gebhardt, K., et al. 2009, ApJ, 698, 198

Guo, F., & Mathews, W. G. 2014, ApJ, 780, 126

Guth, A. H. 1981, Phys. Rev. D, 23, 347

Hall, P. B., Ellingson, E., & Green, R. F. 1997, AJ, 113, 1179

Hamer, S. L., Edge, A. C., Swinbank, A. M., et al. 2014, MNRAS, 437, 862

Häring, N., & Rix, H.-W. 2004, ApJ, 604, L89

Harrison, F. A., Craig, W. W., Christensen, F. E., et al. 2013, ApJ, 770, 103

Hasinger, G. 2008, A&A, 490, 905

Hayashida, K., Miyamoto, S., Kitamoto, S., Negoro, H., & Inoue, H. 1998, ApJ, 500, 642

Henke, B. L., Gullikson, E. M., & Davis, J. C. 1993, Atomic Data and Nuclear Data Tables, 54, 181

Henke, B. L., Lee, P., Tanaka, T. J., Shimabukuro, R. L., & Fujikawa, B. K. 1982, Atomic Data and Nuclear Data Tables, 27, 1

Hlavacek-Larrondo, J., Fabian, A. C., Edge, A. C., et al. 2012, MNRAS, 421, 1360

Hopkins, P. F., Bundy, K., Hernquist, L., & Ellis, R. S. 2007, ApJ, 659, 976

Hopkins, P. F., Hernquist, L., Martini, P., et al. 2005, ApJ, 625, L71

Hoshino, A., Henry, J. P., Sato, K., et al. 2010, PASJ, 62, 371

Hoyle, F., & Fowler, W. A. 1963, Nature, 197, 533

Huchra, J. P., Macri, L. M., Masters, K. L., et al. 2012, ApJS, 199, 26

Husband, K., Bremer, M. N., Stanway, E. R., et al. 2013, MNRAS, 432, 2869

Hutchings, J. B., & Neff, S. G. 1991, AJ, 101, 2001

Ichikawa, K., Matsushita, K., Okabe, N., et al. 2013, ApJ, 766, 90

Ikeda, S., Awaki, H., & Terashima, Y. 2009, ApJ, 692, 608

Ishisaki, Y., Maeda, Y., Fujimoto, R., et al. 2007, PASJ, 59, 113

Iwasawa, K., Crawford, C. S., Fabian, A. C., & Wilman, R. J. 2005, MNRAS, 362, L20

Iwasawa, K., Fabian, A. C., & Ettori, S. 2001, MNRAS, 321, L15

Iwasawa, K., Koyama, K., Awaki, H., et al. 1993, ApJ, 409, 155

Iwasawa, K., & Taniguchi, Y. 1993, ApJ, 413, L15

Jansen, F., Lumb, D., Altieri, B., et al. 2001, A&A, 365, L1

Jiménez-Bailón, E., Santos-Lleó, M., Piconcelli, E., et al. 2007, A&A, 461, 917

Jones, C., & Forman, W. 1984, ApJ, 276, 38

Kaastra, J. S., & Mewe, R. 1993, A&AS, 97, 443

Kalberla, P. M. W., Burton, W. B., Hartmann, D., et al. 2005, A&A, 440, 775

Kallman, T. R., Palmeri, P., Bautista, M. A., Mendoza, C., & Krolik, J. H. 2004, ApJS, 155, 675

Kelley, R. L., Mitsuda, K., Allen, C. A., et al. 2007, PASJ, 59, 77

Kennicutt, Jr., R. C. 1998, ARA&A, 36, 189

Kewley, L. J., Geller, M. J., & Jansen, R. A. 2004, AJ, 127, 2002

Kii, T., Williams, O. R., Ohashi, T., et al. 1991, ApJ, 367, 455

King, A. 2009, ApJ, 695, L107

King, I. 1962, AJ, 67, 471

Klebesadel, R. W., Strong, I. B., & Olson, R. A. 1973, ApJ, 182, L85

Kleinmann, S. G., Hamilton, D., Keel, W. C., et al. 1988, ApJ, 328, 161

Kokubun, M., Makishima, K., Takahashi, T., et al. 2007, PASJ, 59, 53

Kokubun, M., Nakazawa, K., Enoto, T., et al. 2012, in Society of Photo-Optical Instrumentation Engineers (SPIE) Conference Series, Vol. 8443, Society of Photo-Optical Instrumentation Engineers (SPIE) Conference Series

Kolman, M., Halpern, J. P., Shrader, C. R., & Filippenko, A. V. 1991, ApJ, 373, 57

Kolman, M., Halpern, J. P., Shrader, C. R., et al. 1993, ApJ, 402, 514

Komatsu, E., Smith, K. M., Dunkley, J., et al. 2011, ApJS, 192, 18

Kormendy, J., & Ho, L. C. 2013, ARA&A, 51, 511

Koyama, K., Awaki, H., Iwasawa, K., & Ward, M. J. 1992, ApJ, 399, L129

Koyama, K., Hyodo, Y., Inui, T., et al. 2007a, PASJ, 59, 245

Koyama, K., Tsunemi, H., Dotani, T., et al. 2007b, PASJ, 59, 23

Krivonos, R., Tsygankov, S., Revnivtsev, M., et al. 2010, A&A, 523, A61

Krolik, J. H., Madau, P., & Zycki, P. T. 1994, ApJ, 420, L57

Lacy, M., Rawlings, S., & Hill, G. J. 1992, MNRAS, 258, 828

Lawrence, A. 1991, MNRAS, 252, 586

Lawrence, A., & Elvis, M. 1982, ApJ, 256, 410

Lebrun, F., Leray, J. P., Lavocat, P., et al. 2003, A&A, 411, L141

Li, Y., & Bryan, G. L. 2012, ApJ, 747, 26

—. 2013, ArXiv e-prints

—. 2014, ArXiv e-prints

Li, Y., Hernquist, L., Robertson, B., et al. 2007, ApJ, 665, 187

Liedahl, D. A., Osterheld, A. L., & Goldstein, W. H. 1995, ApJ, 438, L115

Lusso, E., Hennawi, J. F., Comastri, A., et al. 2013, ApJ, 777, 86

Lynden-Bell, D. 1969, Nature, 223, 690

Lynden-Bell, D., & Rees, M. J. 1971, MNRAS, 152, 461

Magorrian, J., Tremaine, S., Richstone, D., et al. 1998, AJ, 115, 2285

Mahdavi, A., Hoekstra, H., Babul, A., & Henry, J. P. 2008, MNRAS, 384, 1567

Maiolino, R. 2008, New Astron. Rev., 52, 339

Maiolino, R., & Risaliti, G. 2007, in Astronomical Society of the Pacific Conference Series, Vol. 373, The Central Engine of Active Galactic Nuclei, ed. L. C. Ho & J.-W. Wang, 447

Makino, F. 1987, Astrophys. Lett., 25, 223

Makishima, K., Ezawa, H., Fukuzawa, Y., et al. 2001, PASJ, 53, 401

Marconi, A., & Hunt, L. K. 2003, ApJ, 589, L21

Marconi, A., Risaliti, G., Gilli, R., et al. 2004, MNRAS, 351, 169

Markwardt, C. B., Tueller, J., Skinner, G. K., et al. 2005, ApJ, 633, L77

Masetti, N., Parisi, P., Palazzi, E., et al. 2010, A&A, 519, A96

Mason, K. O., Breeveld, A., Much, R., et al. 2001, A&A, 365, L36

Mathews, W. G., & Bregman, J. N. 1978, ApJ, 224, 308

Matsushita, K. 2011, A&A, 527, A134

Matsushita, K., Sakuma, E., Sasaki, T., Sato, K., & Simionescu, A. 2013, ApJ, 764, 147

Maughan, B. J., Jones, C., Forman, W., & Van Speybroeck, L. 2008, ApJS, 174, 117

McConnell, N. J., & Ma, C.-P. 2013, ApJ, 764, 184

McConnell, N. J., Ma, C.-P., Gebhardt, K., et al. 2011, Nature, 480, 215

McConnell, N. J., Ma, C.-P., Murphy, J. D., et al. 2012, ApJ, 756, 179

McDonald, M., Benson, B., Veilleux, S., Bautz, M. W., & Reichardt, C. L. 2013a, ApJ, 765, L37

McDonald, M., Veilleux, S., Rupke, D. S. N., Mushotzky, R., & Reynolds, C. 2011, ApJ, 734, 95

McDonald, M., Bayliss, M., Benson, B. A., et al. 2012, Nature, 488, 349

McDonald, M., Swinbank, A. M., Edge, A. C., et al. 2013b, ArXiv e-prints

McGill, K. L., Woo, J.-H., Treu, T., & Malkan, M. A. 2008, ApJ, 673, 703

McLure, R. J., & Dunlop, J. S. 2002, MNRAS, 331, 795

McNamara, B. R., & Nulsen, P. E. J. 2007, ARA&A, 45, 117

McNamara, B. R., Rohanizadegan, M., & Nulsen, P. E. J. 2011, ApJ, 727, 39

McNamara, B. R., Wise, M., Nulsen, P. E. J., et al. 2000, ApJ, 534, L135

Miller, B. P., & Brandt, W. N. 2009, ApJ, 695, 755

Miller, J. M. 2007, ARA&A, 45, 441

Miller, J. S., & Goodrich, R. W. 1990, ApJ, 355, 456

Miller, J. S., Goodrich, R. W., & Mathews, W. G. 1991, ApJ, 378, 47

Mirabel, I. F. 1989, ApJ, 340, L13

Miralda-Escude, J., & Babul, A. 1995, ApJ, 449, 18

Mitchell, R. J., Culhane, J. L., Davison, P. J. N., & Ives, J. C. 1976, MNRAS, 175, 29P

Mitsuda, K., Bautz, M., Inoue, H., et al. 2007, PASJ, 59, 1

Mitsuda, K., Kelley, R. L., Boyce, K. R., et al. 2010, in Society of Photo-Optical Instrumentation Engineers (SPIE) Conference Series, Vol. 7732, Society of Photo-Optical Instrumentation Engineers (SPIE) Conference Series

Morganti, R., Oosterloo, T., Tadhunter, C., & Emonts, B. 2003, New Astron. Rev., 47, 273

Morris, R. G., & Fabian, A. C. 2005, MNRAS, 358, 585

Morrison, R., & McCammon, D. 1983, ApJ, 270, 119

Murray, S. S., Chappell, J. H., Kenter, A. T., et al. 1998, in Society of Photo-Optical Instrumentation Engineers (SPIE) Conference Series, Vol. 3356, Society of Photo-Optical Instrumentation Engineers (SPIE) Conference Series, ed. P. Y. Bely & J. B. Breckinridge, 974–984

Mushotzky, R. F., Cowie, L. L., Barger, A. J., & Arnaud, K. A. 2000, Nature, 404, 459

Mushotzky, R. F., Done, C., & Pounds, K. A. 1993, ARA&A, 31, 717

Nagai, D., Vikhlinin, A., & Kravtsov, A. V. 2007, ApJ, 655, 98

Nandra, K., O'Neill, P. M., George, I. M., & Reeves, J. N. 2007, MNRAS, 382, 194

Narayan, R., Blandford, R., & Nityananda, R. 1984, Nature, 310, 112

Netzer, H. 1990, in Active Galactic Nuclei, ed. R. D. Blandford, H. Netzer, L. Woltjer, T. J.-L. Courvoisier, & M. Mayor, 57–160

Neugebauer, G., Miley, G. K., Soifer, B. T., & Clegg, P. E. 1986, ApJ, 308, 815

Nulsen, P. E. J., Jones, C., Forman, W. R., et al. 2007, in Heating versus Cooling in Galaxies and Clusters of Galaxies, ed. H. Böhringer, G. W. Pratt, A. Finoguenov, & P. Schuecker, 210

O'Dea, C. P., Baum, S. A., Privon, G., et al. 2008, ApJ, 681, 1035

Ogle, P., Boulanger, F., Guillard, P., et al. 2010, ApJ, 724, 1193

Ogle, P., Whysong, D., & Antonucci, R. 2006, ApJ, 647, 161

O'Sullivan, E., Giacintucci, S., Babul, A., et al. 2012, MNRAS, 424, 2971

Ota, N. 2012, Research in Astronomy and Astrophysics, 12, 973

Ota, N., Fukazawa, Y., Fabian, A. C., et al. 2007, PASJ, 59, 351

Ozawa, M., Uchiyama, H., Matsumoto, H., et al. 2009, PASJ, 61, 1

Padin, S., Staniszewski, Z., Keisler, R., et al. 2008, Appl. Opt., 47, 4418

Page, K. L., O'Brien, P. T., Reeves, J. N., & Turner, M. J. L. 2004, MNRAS, 347, 316

Pedlar, A., Ghataure, H. S., Davies, R. D., et al. 1990, MNRAS, 246, 477

Penzias, A. A., & Wilson, R. W. 1965, ApJ, 142, 419

Perlmutter, S., Aldering, G., Goldhaber, G., et al. 1999, ApJ, 517, 565

Perucho, M., Quilis, V., & Martí, J.-M. 2011, ApJ, 743, 42

Peterson, B. M. 1993, PASP, 105, 247

—. 1997, An Introduction to Active Galactic Nuclei (Cambridge, New York Cambridge University Press)

Peterson, B. M., Ferrarese, L., Gilbert, K. M., et al. 2004, ApJ, 613, 682

Peterson, J. R., & Fabian, A. C. 2006, Phys. Rep., 427, 1

Peterson, J. R., Kahn, S. M., Paerels, F. B. S., et al. 2003, ApJ, 590, 207

Peterson, J. R., Paerels, F. B. S., Kaastra, J. S., et al. 2001, A&A, 365, L104

Piconcelli, E., Bianchi, S., Miniutti, G., et al. 2008, A&A, 480, 671

Piconcelli, E., Fiore, F., Nicastro, F., et al. 2007, A&A, 473, 85

Pier, E. A., & Voit, G. M. 1995, ApJ, 450, 628

Piffaretti, R., Arnaud, M., Pratt, G. W., Pointecouteau, E., & Melin, J.-B. 2011, A&A, 534, A109

Plagge, T., Benson, B. A., Ade, P. A. R., et al. 2010, ApJ, 716, 1118

Planck Collaboration, Ade, P. A. R., Aghanim, N., et al. 2011, A&A, 536, A1

—. 2013a, ArXiv e-prints

—. 2013b, ArXiv e-prints

—. 2013c, ArXiv e-prints

—. 2014, Accepted by A&A

Pravdo, S. H., & Marshall, F. E. 1984, ApJ, 281, 570

Rafferty, D. A., McNamara, B. R., Nulsen, P. E. J., & Wise, M. W. 2006, ApJ, 652, 216

Raymond, J. C., & Smith, B. W. 1977, ApJS, 35, 419

Ricci, C., Paltani, S., Awaki, H., et al. 2013, A&A, 553, A29

Ricci, C., Walter, R., Courvoisier, T. J.-L., & Paltani, S. 2011, A&A, 532, A102

Richards, G. T., Strauss, M. A., Fan, X., et al. 2006, AJ, 131, 2766

Riess, A. G., Filippenko, A. V., Challis, P., et al. 1998, AJ, 116, 1009

Rizza, E., Loken, C., Bliton, M., et al. 2000, AJ, 119, 21

Rosati, P., Borgani, S., & Norman, C. 2002, ARA&A, 40, 539

Rozo, E., Wechsler, R. H., Rykoff, E. S., et al. 2010, ApJ, 708, 645

Ruhl, J., Ade, P. A. R., Carlstrom, J. E., et al. 2004, in Society of Photo-Optical Instrumentation Engineers (SPIE) Conference Series, Vol. 5498, Z-Spec: a broadband millimeter-wave grating spectrometer: design, construction, and first cryogenic measurements, ed. C. M. Bradford, P. A. R. Ade, J. E. Aguirre, J. J. Bock, M. Dragovan, L. Duband, L. Earle, J. Glenn, H. Matsuhara, B. J. Naylor, H. T. Nguyen, M. Yun, & J. Zmuidzinas, 11–29

Russell, H. R., Fabian, A. C., Sanders, J. S., et al. 2010, MNRAS, 402, 1561

Russell, H. R., Fabian, A. C., Taylor, G. B., et al. 2012, MNRAS, 422, 590

Rybicki, G. B., & Lightman, A. P. 1985, Radiative processes in astrophysics. (Wiley-VCH)

Sadoun, R., & Colin, J. 2012, MNRAS, 426, L51

Sakuma, E., Ota, N., Sato, K., Sato, T., & Matsushita, K. 2011, PASJ, 63, 979

Salpeter, E. E. 1964, ApJ, 140, 796

Salviander, S., & Shields, G. A. 2013, ApJ, 764, 80

Sarazin, C. L. 1988, X-ray emission from clusters of galaxies (Cambridge: Cambridge University Press)

Sato, K. 1981, Physics Letters B, 99, 66

Sato, T., Sasaki, T., Matsushita, K., et al. 2012, PASJ, 64, 95

Sazonov, S. Y., Ostriker, J. P., Ciotti, L., & Sunyaev, R. A. 2005, MNRAS, 358, 168

Schmidt, M. 1963, Nature, 197, 1040

—. 1965, ApJ, 141, 1

Schneider, D. P., Bahcall, J. N., Gunn, J. E., & Dressler, A. 1992, AJ, 103, 1047

Serlemitsos, P. J., Soong, Y., Chan, K.-W., et al. 2007, PASJ, 59, 9

Seyfert, C. K. 1943, ApJ, 97, 28

Shu, X. W., Yaqoob, T., & Wang, J. X. 2010, ApJS, 187, 581

Siemiginowska, A., Burke, D. J., Aldcroft, T. L., et al. 2010, ApJ, 722, 102

Simionescu, A., Werner, N., Urban, O., et al. 2012, ApJ, 757, 182

Simpson, C. 2005, MNRAS, 360, 565

Skrutskie, M. F., Cutri, R. M., Stiening, R., et al. 2006, AJ, 131, 1163

Smith, R. K., Brickhouse, N. S., Liedahl, D. A., & Raymond, J. C. 2001, ApJ, 556, L91

Springel, V., Frenk, C. S., & White, S. D. M. 2006, Nature, 440, 1137

Springel, V., White, S. D. M., Jenkins, A., et al. 2005, Nature, 435, 629

Staniszewski, Z., Ade, P. A. R., Aird, K. A., et al. 2009, ApJ, 701, 32

Steffen, A. T., Barger, A. J., Cowie, L. L., Mushotzky, R. F., & Yang, Y. 2003, ApJ, 596, L23

Strüder, L., Briel, U., Dennerl, K., et al. 2001, A&A, 365, L18

Suganuma, M., Yoshii, Y., Kobayashi, Y., et al. 2006, ApJ, 639, 46

Sunyaev, R. A., & Zeldovich, I. B. 1980, ARA&A, 18, 537

Sunyaev, R. A., & Zeldovich, Y. B. 1972, Comments on Astrophysics and Space Physics, 4, 173

Takahashi, H., Hayashida, K., & Anabuki, N. 2010, PASJ, 62, 1483

Takahashi, T., Abe, K., Endo, M., et al. 2007, PASJ, 59, 35

Takahashi, T., Mitsuda, K., Kelley, R., et al. 2012, in Society of Photo-Optical Instrumentation Engineers (SPIE) Conference Series, Vol. 8443, Society of Photo-Optical Instrumentation Engineers (SPIE) Conference Series

Tamura, T., Hayashida, K., Ueda, S., & Nagai, M. 2011, PASJ, 63, 1009

Tamura, T., Kaastra, J. S., Peterson, J. R., et al. 2001, A&A, 365, L87

Tanaka, Y., Inoue, H., & Holt, S. S. 1994, PASJ, 46, L37

Taniguchi, Y., Sato, Y., Kawara, K., Murayama, T., & Mouri, H. 1997, A&A, 318, L1

Tarter, C. B., Tucker, W. H., & Salpeter, E. E. 1969, ApJ, 156, 943

Tawa, N., Hayashida, K., Nagai, M., et al. 2008, PASJ, 60, 11

Treister, E., Krolik, J. H., & Dullemond, C. 2008, ApJ, 679, 140

Treister, E., & Urry, C. M. 2006, ApJ, 652, L79

—. 2012, Advances in Astronomy, 2012

Tremaine, S., Gebhardt, K., Bender, R., et al. 2002, ApJ, 574, 740

Tueller, J., Mushotzky, R. F., Barthelmy, S., et al. 2008, ApJ, 681, 113

Tueller, J., Baumgartner, W. H., Markwardt, C. B., et al. 2010, ApJS, 186, 378

Turner, E. L., Ostriker, J. P., & Gott, III, J. R. 1984, ApJ, 284, 1

Turner, M. J. L., Thomas, H. D., Patchett, B. E., et al. 1989, PASJ, 41, 345

Turner, M. J. L., Abbey, A., Arnaud, M., et al. 2001, A&A, 365, L27

Ubertini, P., Lebrun, F., Di Cocco, G., et al. 2003, A&A, 411, L131

Ueda, S., Hayashida, K., Anabuki, N., et al. 2013a, ApJ, 778, 33

Ueda, S., Hayashida, K., Nakajima, H., & Tsunemi, H. 2013b, Astronomische Nachrichten, 334, 426

Ueda, Y., Akiyama, M., Ohta, K., & Miyaji, T. 2003, ApJ, 598, 886

Urry, C. M., & Padovani, P. 1995, PASP, 107, 803

Urry, C. M., & Treister, E. 2007, Proceedings of "2007 STScI spring symposium: Black Holes", eds. M. Livio & A. M. Koekemoer, Cambridge University Press

Valentijn, E. A., & Bijleveld, W. 1983, A&A, 125, 223

van Breugel, W., Balick, B., Heckman, T., Miley, G., & Helfand, D. 1983, AJ, 88, 40

van Speybroeck, L. P., Jerius, D., Edgar, R. J., et al. 1997, in Society of Photo-Optical Instrumentation Engineers (SPIE) Conference Series, Vol. 3113, Society of Photo-Optical Instrumentation Engineers (SPIE) Conference Series, ed. R. B. Hoover & A. B. Walker, 89–104

Vanderlinde, K., Crawford, T. M., de Haan, T., et al. 2010, ApJ, 722, 1180

Véron-Cetty, M.-P., & Véron, P. 2001, A&A, 374, 92

—. 2010, A&A, 518, A10

Vestergaard, M., Fan, X., Tremonti, C. A., Osmer, P. S., & Richards, G. T. 2008, ApJ, 674, L1

Vettolani, G., Zucca, E., Zamorani, G., et al. 1997, A&A, 325, 954

Vettolani, G., Zucca, E., Merighi, R., et al. 1998, A&AS, 130, 323

Vignali, C., Piconcelli, E., Lanzuisi, G., et al. 2011, MNRAS, 416, 2068

Vikhlinin, A., Kravtsov, A. V., Burenin, R. A., et al. 2009, ApJ, 692, 1060

Voges, W., Aschenbach, B., Boller, T., et al. 1999, A&A, 349, 389

Volonteri, M., & Ciotti, L. 2013, ApJ, 768, 29

Weisskopf, M. C., Brinkman, B., Canizares, C., et al. 2002, PASP, 114, 1

Weisskopf, M. C., & O'dell, S. L. 1997, in Society of Photo-Optical Instrumentation Engineers (SPIE) Conference Series, Vol. 3113, Society of Photo-Optical Instrumentation Engineers (SPIE) Conference Series, ed. R. B. Hoover & A. B. Walker, 2–17

Werner, M. W., Roellig, T. L., Low, F. J., et al. 2004, ApJS, 154, 1

White, D. A., Fabian, A. C., Allen, S. W., et al. 1994, MNRAS, 269, 589

White, D. A., Jones, C., & Forman, W. 1997, MNRAS, 292, 419

Williamson, R., Benson, B. A., High, F. W., et al. 2011, ApJ, 738, 139

Wills, K. A., Tadhunter, C. N., Robinson, T. G., & Morganti, R. 2002, MNRAS, 333, 211

Winkler, C., Courvoisier, T. J.-L., Di Cocco, G., et al. 2003, A&A, 411, L1

Wu, J., Vanden Berk, D. E., Brandt, W. N., et al. 2009, ApJ, 702, 767

Yamashita, A., Matsumoto, C., Ishida, M., et al. 1997, ApJ, 486, 763

Yaqoob, T., & Serlemitsos, P. 2005, ApJ, 623, 112

York, D. G., Adelman, J., Anderson, Jr., J. E., et al. 2000, AJ, 120, 1579

Zel'dovich, Y. B. 1964, Soviet Physics Doklady, 9, 195

Zhao, P., Cohen, L. M., & van Speybroeck, L. P. 1997, in Society of Photo-Optical Instrumentation Engineers (SPIE) Conference Series, Vol. 3113, Society of Photo-Optical Instrumentation Engineers (SPIE) Conference Series, ed. R. B. Hoover & A. B. Walker, 106–123

Zhou, X.-L., & Wang, J.-M. 2005, ApJ, 618, L83

Zubovas, K., & King, A. R. 2012, MNRAS, 426, 2751

Zwicky, F. 1933, Helvetica Physica Acta, 6, 110

—. 1937, Physical Review, 51, 290